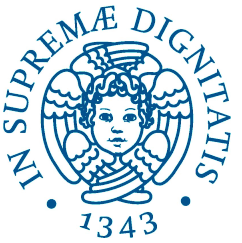

University of Pisa

Graduate Course in Physics

PhD Thesis - XVI Cycle

Search for Lepton Flavor Violation in the MEG Experiment and its Upgrade

Candidate
Francesco Tenchini

Supervisor
Dr. **Alessandro Baldini**

Contents

Introduction

The Standard Model is an incredibly successful theory that encompasses the electromagnetic, weak and strong interactions of elementary particles and describes how they shape our world at the most basic level. It is supported by a large breadth of experimental evidence and boasts many successful predictions, culminating with the recent observation of the Higgs boson (or, at the very least, a Higgs-like particle) at the LHC.

The search for rare processes beyond the scope of the Standard Model has become an increasingly important element of experimental particle physics. While the recent evidence of neutrino oscillations can be assimilated into the model with little trouble, all SM extensions predict Lepton Flavor Violating phenomena also occurring in the charged sector at high branching ratios. Observation of such extremely rare processes would be irrefutable proof of new physics.

One of these pursuits, the search for the rare lepton flavor violating $\mu \to e\gamma$ decay, is being undertaken by the MEG experiment at the Paul Scherrer Institut (PSI, Switzerland), in a collaboration of physicists from Italy, Japan, Switzerland, USA and Russia. The current published results, based on the analysis of the first half of the collected data, provide the best upper limit for the $\mu \to e\gamma$ branching ratio: $\mathcal{B} = 5.7 \times 10^{-13}$ at 90% CL.

A second phase of the experiment (MEG II) has been studied to provide a substantial increase of sensitivity, down to $\sim 5 \times 10^{-14}$. The construction of a new positron spectrometer, in which the Italian contribution features prominently, is underway, along with a new timing counter and a substantial redesign of the calorimeter.

This thesis focuses on the study of the properties of the new drift chamber and of the liquid xenon calorimeter.

In the first part, the theory behind the Standard Model and its extensions is summarized, with a focus on lepton flavor violation. The $\mu \to e\gamma$ decay kinematics are then

discussed.

In the second part the MEG I experiment is described and the analysis of the latest published results are presented.

The third part discusses the MEG II upgrade scheme and objectives and contains the core of the thesis. The drift chamber prototype studies taking place within the scope of the R&D activities in Pisa are presented, followed by an in-depth investigation of the photon detector behavior showing the limits of its achievable energy resolution.

In the drift chamber studies we concern ourselves with the realization of small prototypes for aging and single hit resolution measurements, as well as the wiring and testing of the first full scale single cell prototype, showing the feasibility of a 2 m long stereo drift chamber with variable cell size and the possibility of using a double readout to achieve single cell longitudinal resolutions on the scale of 10 cm. The gain change along the cell length is measured and compared to the simulations and a method for measuring wire tension based on acustic excitation is presented.

In the photon detector investigation we attempt to understand why the energy resolution of the MEG I calorimeter, while excellent, is still lower than the predicted value. A detailed study of calibration data is presented, leading to the development of a more accurate Monte Carlo simulation and an improved knowledge of the optical parameters of the detector. Evaluation of PMT quantum efficiency is discussed in this context, and the use of data acquired in gas phase xenon is proposed for MEG II as opposed to the liquid calibration scheme currently used. Development of a new reconstruction algorithm is attempted, with some promising results which still leave some questions open.

Part I

Theory and Phenomenology

1

Theory of Lepton Flavor Violation

Since its inception nearly half a century ago, the Standard Model has proven to be an incredibly successful theory for predicting particle physics phenomenology. Nevertheless, the many free parameters and accidental symmetries hint at a larger picture where the SM in only a low-energy approximation of a more fundamental theory.

1.1 The Standard Model

The Standard Model (SM) combines in its description three of the four fundamental interactions: electromagnetic, weak and strong interactions, leaving out only the gravitational one.

The two classes of elementary particles, leptons and quarks, are both fermions with spin = 1/2. Experimental evidence shows that quarks are subject to all the three interactions, while leptons are not subject to the strong one. Particles with integer spin, called gauge bosons, carry the interaction between fermions.

The SM is a gauge theory based on the group $\mathrm{SU(3)_C} \otimes \mathrm{SU(2)_L} \otimes \mathrm{U(1)_Y}$, which is spontaneously broken at the Fermi mass scale ($M_F \sim 100$ GeV) into $\mathrm{SU(3)_C} \otimes \mathrm{U(1)_{EM}}$. Free fermion and boson fields are introduced as elementary fields, along with the Higgs field. The coupling of fermions and gauge bosons with the Higgs field gives rise to particle mass.

We will denote quarks fields as $q_{\rm ij}$ and lepton fields as $l_{\rm ij}$, while $\psi_{\rm ij}$ will be used for a generic fermionic field. The index i $=$ 1, 2, 3 runs on the 3 flavor families and j $=$ L, R labels left or right chirality. Boson fields associated to the symmetry groups are G_μ for SU(3), W^μ for SU(2) and B^μ for U(1).

The SM Lagrangian $\mathcal{L}_{\rm SM}$ can be written as the sum of three components:

$$\mathcal{L}_{\rm SM} \;=\; \mathcal{L}_{\rm Gauge} \;+\; \mathcal{L}_{\rm Higgs} \;+\; \mathcal{L}_{\rm Yukawa} \tag{1.1}$$

which are respectively the gauge interaction between fermions and gauge bosons, the Higgs potential and the Yukawa interaction between elementary particles and the Higgs field ϕ (1). The Lagrangian for the gauge interaction is

$$\mathcal{L}_{Gauge} \;=\; \sum_{\rm SU(3),SU(2),U(1)} \mathcal{F}^{\rm a}_{\mu\nu}\mathcal{F}^{\rm a\mu\nu} \;+\; \sum_{q,l} i\overline{\psi_{ij}}\gamma^\mu \mathcal{D}_\mu \psi_{ij} \;+\; (\mathcal{D}_\mu\phi)^\dagger(\mathcal{D}^\mu\phi) \tag{1.2}$$

where

$$\mathcal{F}^{\rm a}_{\mu\nu} \;=\; \partial_\mu {\rm T}^{\rm a}_\nu \;-\; \partial_\nu {\rm T}^{\rm a}_\mu \;-\; {\rm c f_{abc} T}^{\rm b}_\mu {\rm T}^{\rm c}_\nu \tag{1.3}$$

is the gauge field tensor, $\rm T_\mu$ marks any gauge boson field (G_μ, W^μ, B^μ), $\rm f_{abc}$ are the group structure constants and c is the coupling constant ($g_{\rm s}$ for SU(3), g for SU(2) and $g\prime$ for U(1)). The covariant derivative defined as:

$$\mathcal{D}_\mu \;=\; \partial_\mu \;+\; ig_{\rm s}\frac{\lambda^{\rm a}}{2}G^{\rm a}_\mu \;+\; ig\frac{\tau^{\rm a}}{2}W^{\rm a}_\mu \;+\; ig\prime Q_{\rm Y} B_\mu \tag{1.4}$$

The most general renormalizable form for the Higgs potential part of lagrangian is

$$\mathcal{L}_{\rm Higgs} \;=\; \mu^2\phi^\dagger\phi \;-\; \lambda(\phi^\dagger\phi)^2 \tag{1.5}$$

where ϕ, the Higgs field, is a scalar complex $SU(2)_L$ doublet with $Y = 1$. By selecting the gauge in which

$$\langle\phi\rangle = \begin{pmatrix}0\\ v\end{pmatrix}, \quad v = \sqrt{\frac{\mu^2}{2\lambda}} \tag{1.6}$$

the symmetry is spontaneously broken: $\rm SU(2)_L \otimes U(1)_Y \rightarrow U(1)_{EM}$ and three of the four bosons acquire mass. The masses of the particles in terms of the parameters of the theory as shown in Tab. 1.1. The Weinberg angle $\theta_{\rm W}$, as the $\rm m_W$ and $\rm m_Z$ were each measured and found coherent with theory expectations(2):

$$\sin^2(\theta_{\rm W}) \;=\; 0.23126 \;\pm\; 0.0005 \tag{1.7}$$

$$\rm m_W \;=\; (80.385 \;\pm\; 0.015)\ GeV/c^2 \tag{1.8}$$

$$\rm m_Z \;=\; (91.1876 \;\pm\; 0.0021)\ GeV/c^2 s \tag{1.9}$$

$\mathrm{m}_W = gv/2$
$\mathrm{m}_Z = \sqrt{g^2 + g\prime^2}v/2$
$\mathrm{m}_W/\mathrm{m}_\mathrm{Z} = \mathrm{g}/\sqrt{\mathrm{g}^2 + \mathrm{g}'^2} = \sqrt{1-\sin^2(\theta_\mathrm{W})}$
$\mathrm{m}_H = \sqrt{2\lambda}v$
$\sin(\theta_\mathrm{W}) = g\prime/\sqrt{g^2 + g\prime^2}$
$\mathrm{e} = g\sin(\theta_\mathrm{W})$

Table 1.1: Electroweak boson masses, Higgs boson mass, $\sin(\theta_\mathrm{W})$ and electric charge e in function of theory parameters.

The Yukawa interaction part of the Lagrangian

$$\mathcal{L}_{\text{Yukawa}} = -[\overline{e}_{iR}(m_e)_{\mathrm{ij}}e_{\mathrm{jL}} + \overline{d}_{\mathrm{iR}}(m_d)_{\mathrm{ij}}d_{\mathrm{jL}} + \overline{u}_{\mathrm{iR}}(m_u)_{\mathrm{ij}}u_{\mathrm{jL}}] + \mathrm{HC} \tag{1.10}$$

is obtained substituting the vacuum expectation value for the Higgs field. The mass terms for quark and leptons are written in terms of the Yukawa coupling constants:

$$(m_{\mathrm{e,d,u}})_{\mathrm{ij}} = -(y_{\mathrm{e,d,u}})_{\mathrm{ij}}(v/\sqrt{2}). \tag{1.11}$$

with the neutrino being massless in this picture. Each mass matrix can, in general, be diagonalized in the flavor space by appropriate unitary transformations for left- and right-handed fermion fields. Since these rotations also affect the kinetic term of the lagrangian, flavor mixing is induced in the charged weak interaction for quarks:

$$\mathcal{L} = -\frac{g}{\sqrt{2}}[\overline{u}_{\mathrm{iL}}\gamma^\mu(V_{\mathrm{CKM}})_{\mathrm{ij}}d_{\mathrm{jL}}W^+_\mu + \overline{d}_{\mathrm{iL}}\gamma^\mu(V_{\mathrm{CKM}})^*_{\mathrm{ij}}u_{\mathrm{jL}}W^-_\mu] \tag{1.12}$$

where the $(V_{\mathrm{CKM})_{\mathrm{ij}}}$ is the flavor mixing matrix for the quark sector, *i.e.* the Cabibbo-Kobayashi-Maskawa (CKM) matrix. Meanwhile, due to the zero mass of neutrinos, the charged leptons mass matrix can be fully diagonalized by transformations on the lepton doublet fields $(e_{\mathrm{jL}}, \nu_{\mathrm{jL}})$ and the lepton singlet fields (e_{iR}), while maintaining the charged weak current interaction diagonal:

$$\mathcal{L} = -\frac{g}{\sqrt{2}}[\overline{\nu}_{\mathrm{iL}}\gamma^\mu e_{\mathrm{iL}}W^+_\mu + \overline{e}_{\mathrm{iL}}\gamma^\mu\nu_{\mathrm{iL}}W^-_\mu] \tag{1.13}$$

In this basis lepton flavors can be defined for each generation and no mixing occurs. It follows that any Lepton Flavor Violating decay, such as $\mu \to \mathrm{e}\gamma$, is forbidden.

1.2 Neutrino Oscillations

In the last decade, evidence arose of lepton flavor oscillations in the neutral sector, a mixing phenomenon only possible with thevi existence of massive neutrinos. The mixing can be described by the Pontecorvo-Maki-Nakagawa-Sakata maxtrix, written as

$$\nu_\ell \;=\; \sum_k (V_{\rm PMNS})_{\ell k}\nu_k \tag{1.14}$$

where $\ell \;=\; \mathrm{e},\ \mu,\ \tau$ (flavor eigenstate), $\mathrm{k} = 1, 2, 3$ (mass eigenstate).

Thus the Lagrangian for lepton charged weak interactions then becomes

$$\mathcal{L} \;=\; -\frac{g}{\sqrt{2}}\left[\overline{\nu}_{\rm iL}\gamma^\mu (V_{\rm PMNS})_{\rm ij} e_{\rm iL} W_\mu^+ \;+\; \overline{e}_{\rm iL}\gamma^\mu (V_{\rm PMNS})^*_{\rm ij}\nu_{\rm jL} W_\mu^-\right] \tag{1.15}$$

Given a neutrino ν_ℓ emitted from with energy E, the probability of observing a flavor transition at distance L is

$$\mathrm{P}(\nu_\ell \to \nu_{\ell\prime}) \;=\; \sin^2(2\theta)\sin^2\left(1.27\frac{\Delta \mathrm{m}^2(\mathrm{eV}^2)\mathrm{L(m)}}{\mathrm{E(MeV)}}\right) \tag{1.16}$$

with θ being the $\nu_\ell - \nu_{\ell\prime}$ mixing angle and $\Delta m^2 = (m_{\nu_\ell} - m_{\nu_{\ell\prime}})^2$ being the squared neutrino mass difference. In case of oscillations, a decrease in the flux of ν_ℓ is expected and indeed observed in reactor, atmospheric and solar neutrinos (3, 4, 5, 6, 7, 8). In this framework, charged Lepton Flavor Violation (cLFV) is allowed through neutrino loops. The diagrams for the $\mu \to \mathrm{e}\gamma$ process are shown in Fig. 1.1 as an example. In this picture the $\mu \to \mathrm{e}\gamma$ normalized decay probability can be written as

$$\mathrm{B}(\mu^+ \to \mathrm{e}^+\gamma) \;=\; 5 \times 10^{-48}[\Delta \mathrm{m}^2(\mathrm{eV})^2]^2 \sin^2(\theta)\cos^2(\theta) \tag{1.17}$$

and substituting the experimental values (2) $\Delta \mathrm{m}^2_{12} \;=\; 7.5 \times 10^{-5}\ \mathrm{eV}^2$ and $\sin(2\theta_{12}) \;=\; 0.85$ gives us a branching ratio of a $\mathrm{B} \approx\ 10^{-55}$, which is impossible to reasonably measure.

1.3 Beyond the Standard Model

Even though the Standard Model is highly successful at predicting physical observables, it still leaves some questions open. In particular, there is no unification of the coupling constants for the three forces involved, numerous free parameters are present (such as the amount of lepton/quark families, every mass and every mixing term) and the value of the Higgs mass poses a hierarchy problem, being several orders of magnitude below the Planck scale.

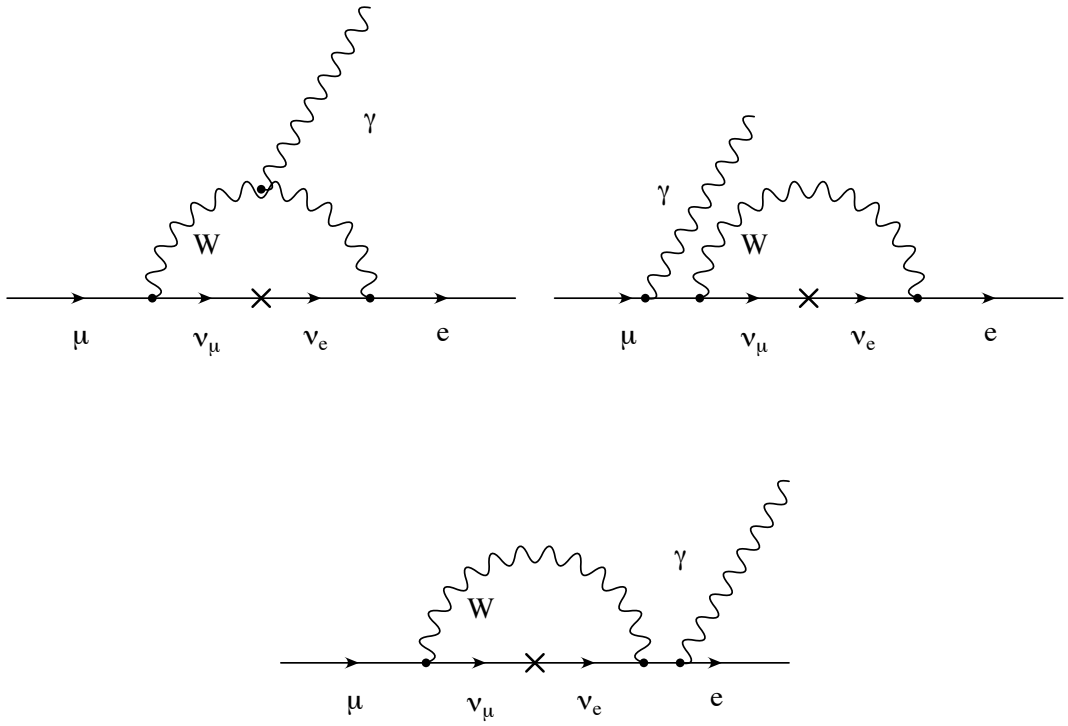

Figure 1.1: Feynman diagrams for the $\mu \to e\gamma$ decay in the Standard Model with the inclusion of massive neutrinos.

1.3.1 Grand Unification Theories (GUT)

The symmetry group SU(3) $\times$ SU(2) $\times$ U(1) possesses four indipendent diagonal generators: Y, T_3, λ_3 and λ_8. The simplest solution to achieve an unified theory is to describe it in terms of a symmetry group of rank four or higher. The simplest viable candidate is SU(5) (9).

In this description the SM fermions are arranged in terms of the $5 \oplus 10$ representations of the SU(5). There are 24 gauge bosons, 12 of which belong to the Standard Model and 12 more describing lepton-quark interactions. This model successfully predicts charge quantization, as well as the value of $\sin\theta_W$. Unfortunately, it also predicts a value for the proton decay rate which is inconsistent with experimental results.

Alternatively, a possible unification is provided by SO(10) group (10, 11). This is equivalent to SU(5) $\otimes$ U(1), corresponding the addition of a singlet field for the right handed neutrino. This a very appealing picture, in which all fermions belong to a single

16-dimensional representation.

GUT theories predict the unification of all coupling constants at a mass scale of $M_{GUT} \sim 10^{15}$ GeV, as well as the observed discrepancies at lower energies.

1.3.2 Supersymmetry (SUSY)

It is appealing to try and construct a theory in which complete unification of all forces (electroweak, strong and gravitational) becomes possible, resulting in the introduction of a new energy scale $M_{Planck} \approx 10^{19}$ at which the forces become comparable.

However, even though the Higgs potential parameters are in principle arbitrary, loop corrections to the Higgs mass give divergent contributions

$$\delta m_H^2 \sim \Lambda^2 \tag{1.18}$$

with Λ being the cutoff point of the theory, up to the Planck scale M_{Planck}. This poses the problem of explaining why the Higgs mass lies at the Fermi scale instead, without resorting to significant fine tuning. This is achieved through a supersymmetrical theory.

SUSY is a symmetry which commutes with every internal symmetry and predicts, for each SM particle, a supersymmetric partner with the same internal quantum numbers and a spin 1/2 lower. A few of those particles are shown as an example in Tab. 1.2. Supersymmetry particles give rise to new terms into the δm_H evaluation:

SM particles	**spin**	**SUSY partners**	**spin**
quark (q)	1/2	squark ($\tilde{q}$)	0
lepton (l)	1/2	slepton ($\tilde{l}$)	0
gluon(G)	1	gluino	1/2
$W^{\pm}, Z^0, \gamma$	1	chargino $\tilde{\chi}_i^{\pm}$ (i = 1-2)	1/2
Higgs boson H	0	neutralino $\tilde{\chi}_i^0$ (i = 1-4)	1/2

Table 1.2: Standard Model particles with their SUSY counterparts.

$$\delta m_H^2 \approx g_i^2 (m_{F_i}^2 - m_{\tilde{F}_i}^2) \tag{1.19}$$

where the opposite sign is caused by the difference between Fermi and Bose statistics. Supersymmetry is obviously broken as no supersymmetric partner is yet observed, and Eq. 1.19 predicts the scale at which they can be found to be the same as the Higgs mass: the Fermi scale.

1.4 $\mu \to e\gamma$ as a Probe for New Physics

Standard Model extensions are generally characterized by heavy partners whose interactions are not flavor-diagonal. Thus LFV in the SM particles is possible through flavor transitions in their heavy counterparts, suppressed by a power of the energy scale of the theory.

1.4.1 SUSY-GUT

In SUSY models, off-diagonal slepton mass matrix elements generate tree-level transitions between different leptonic generations. If we indicate the mixing angles between the first two generations of sleptons by $\theta_{\tilde{e}\tilde{\mu}}$ we obtain (12)

$$B(\mu \to e\gamma) \propto \frac{\alpha^3 \pi \theta^2_{\tilde{e}\tilde{\mu}}}{{G_F}^2 \tilde{m}^4} \tan^2(\beta) \tag{1.20}$$

where $\tilde{m}$ is a typical supersymmetric mass and $\tan(\beta)$ is the mass ratio of supersymmetric Higgs bosons. The mixing matrix for supersymmetric sleptons is unknown, but it is generally modeled to be analogous to the CKM or PMNS matrices. Supersymmetric particles have not yet been observed in energy frontiers experiments such as LHC; cLFV experiments provide a complementary probe which is especially sensitive to SUSY-GUT models. The exact expectations are in general dependent on the parameters above, but assuming SUSY particles at the Fermi scale, most models find large branching ratios close to the current experimental limits. For example, in the SUSY-GUT SO(10) model, the predicted value for $\mathcal{B}(\mu \to e\gamma)$ is found to be larger than 10^{-14} (see Fig. 1.3).

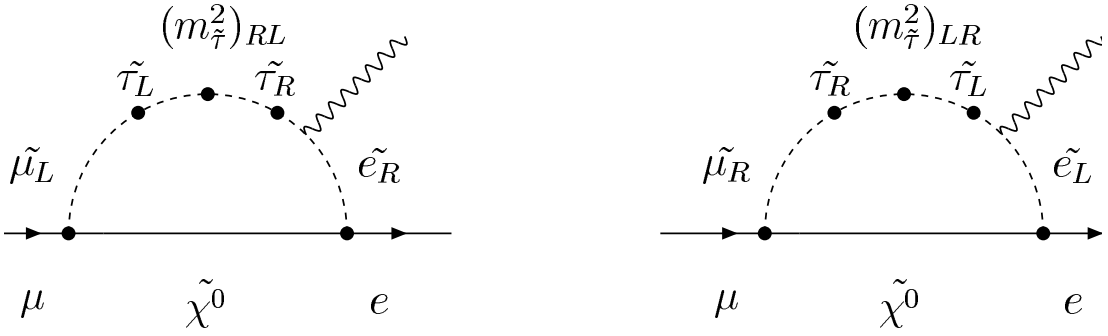

Figure 1.2: Feynman diagram for the dominant contributions to $\mu \to e\gamma$ in SUSY SO(10).

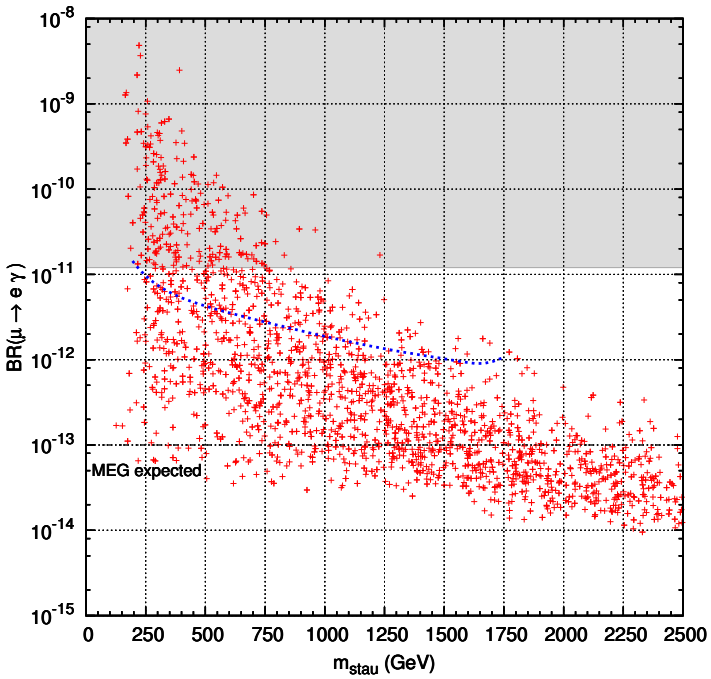

Figure 1.3: Branching ratio probability for the $\mu \rightarrow e\gamma$ decay in the SUSY-GUT SO(10) model as a function of stau mass. The grey area refers to the experimental limits before the advent of MEG. (13, 14)

1.4.2 Non-GUT Models

In non-GUT SUSY models, the predictions for cLFV decays are more reliant on the choice of parameters. One large contribution to flavor violation comes from the evidence of neutrino mass and mixing. The addition of massive right-handed neutrinos (*i.e.* seesaw mechanism) gives once again rise to off-diagonal terms in SUSY.

Recent observation (15, 16, 17, 18) of large values for the ν mixing angle, $\theta_{13} \approx 9°$ noticeably restrict the parameter space, once again predicting large values for the $\mu \to e\gamma$ decay. Two examples are given in Fig. 1.4 and 1.5 (19, 20).

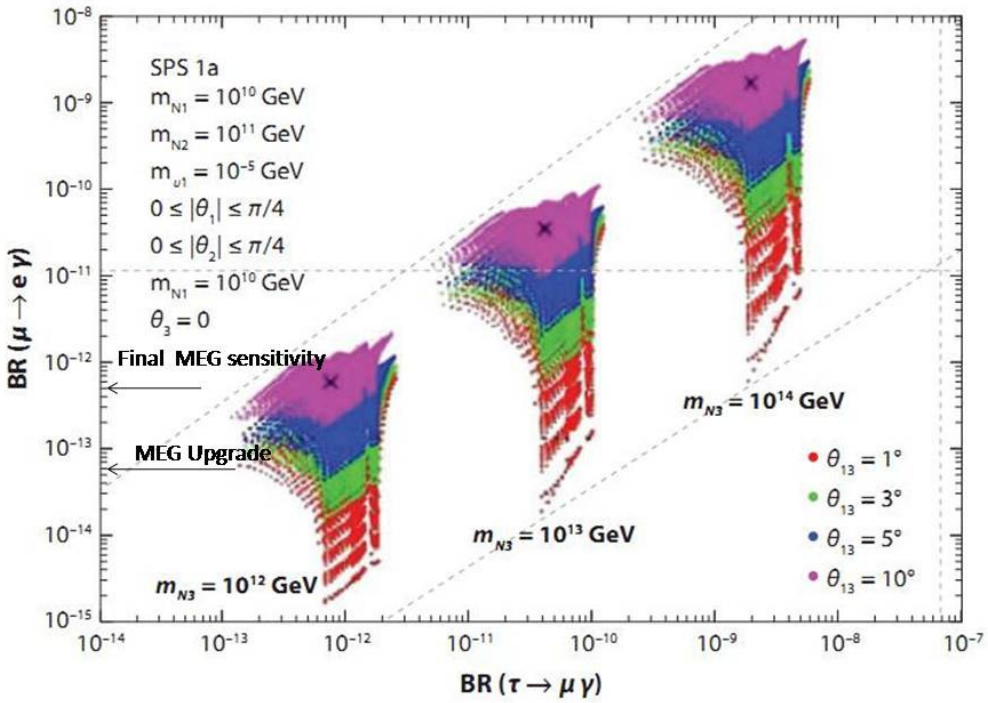

Figure 1.4: Predicted values for $\mu \to e\gamma$ and $\tau \to \mu\gamma$ decays as a function of neutrino mixing angles and slepton masses. Experimental evidence favors high values for θ_{13} (magenta)

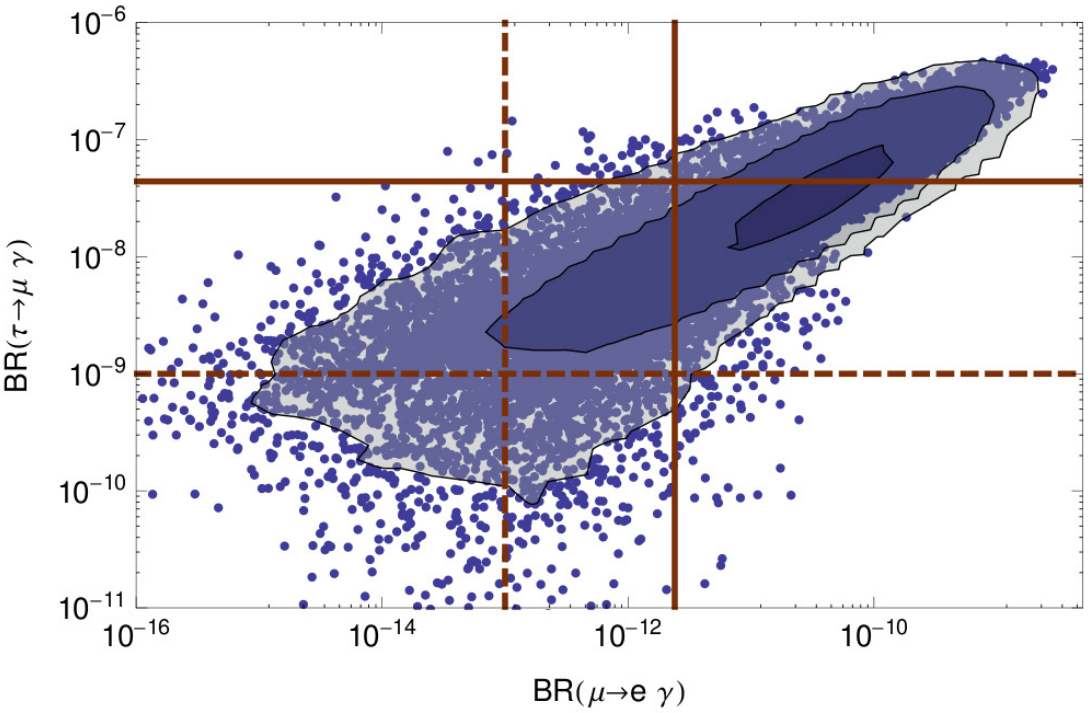

Figure 1.5: Predictions for $\mu \to e\gamma$ and $\tau \to \mu\gamma$ violation if only one slepton lies at the Fermi scale.

1.4.3 Comparison to Other Decay Channels

The $\tau \to \mu\gamma$ decay is an alternate channel for cLFV search which in SUSY has a branching ratio ranging from roughly equivalent (as in Fig. 1.5) to 10^4 higher (SUSY-GUT SO(10) prediction). One might then wonder why the τ channel is not the preferred one. The matter of fact is that while μ production is easily done at low energies, producing μ-beams which can then be stopped to observe a decay at rest, τ are produced at high energies in B-factories. This, combined with their short life time ($\sim 10^{-13}$ s) makes the production of low energy τ-beams impossible; cLFV must then be observed in the in-flight reference frame. Moreover amount of τ typically produced per year in a B-factory is $\approx 10^8$. A muon beam line can instead deliver up to $10^{13} \div 10^{14}$ μ/year, easily making up for the BR difference in event rate alone.

Internal comparison between muon decay channels is usually done in a model-independent fashion using the effective lagrangian

$$\mathcal{L}_{cLFV} = \frac{m_\mu}{(\kappa+1)\,\Lambda^2}\bar{\mu}_R\sigma_{\mu\nu}e_L F^{\mu\nu} + \frac{\kappa}{(\kappa+1)\,\Lambda^2}\bar{\mu}_R\gamma_\mu e_L \bar{f}\gamma^\mu f \tag{1.21}$$

where f and $\bar{f}$ are the appropriate fermion fields for decay products. The lagrangian is composed of two flavor violating terms and $\mu \to e\gamma$ only contributes to the first, while other processes like $\tau \to eee$ and $\mu \to e$ can proceed through both. SUSY-GUT models privilege the $\kappa = 0$ modes, and therefore MEG is strongly competitive with respects to other channels, as shown on Fig. 1.6, even for future experiments.

1.4.4 Current Status of the $\mu \to e\gamma$ search

Prior to the MEG experiment, the best result for $\mathcal{B}(\mu \to e\gamma)$ was an upper limit of 1.2×10^{-11} at 90% confidence level, published by the MEGA collaboration (14). The current best result, 5.7×10^{-13} at 90% CL, was published by the MEG collaboration in 2011 and will be discussed in Chapter 4.

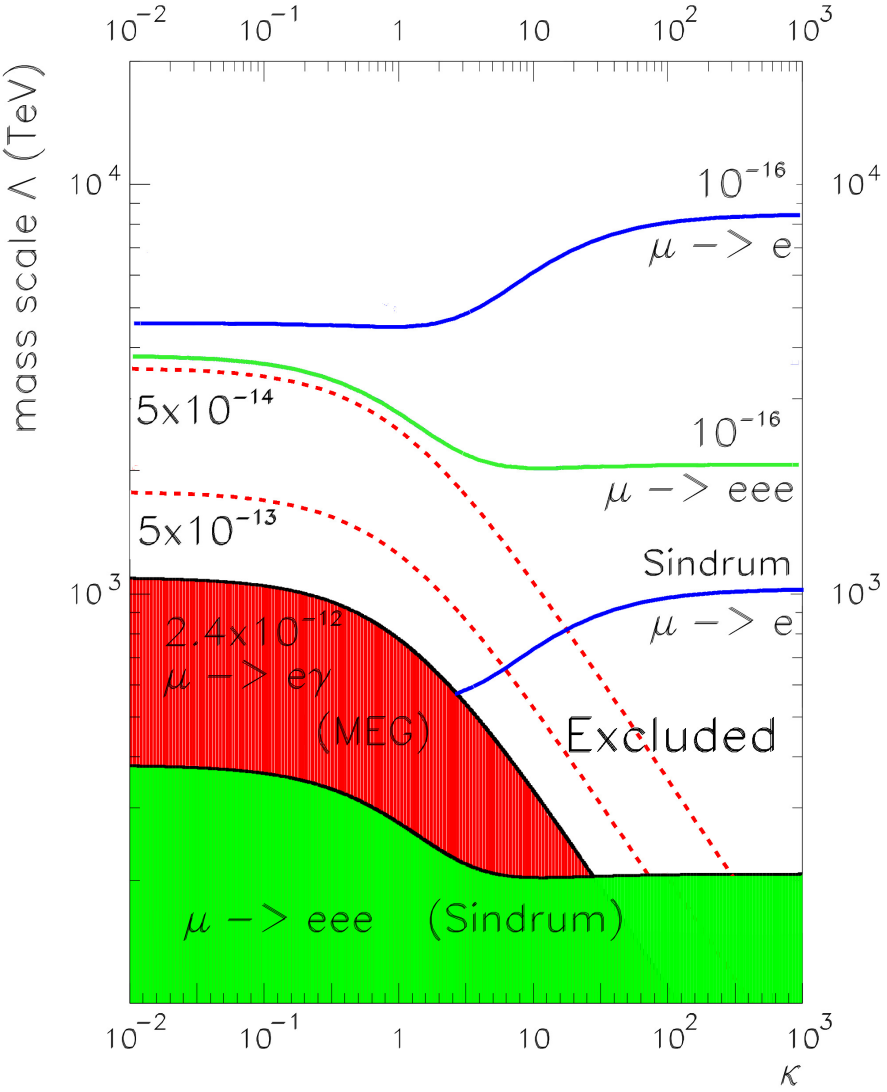

Figure 1.6: Regions in the (Λ , κ) parameter space excluded by various muon cLFV experiments. The red region refers to the first MEG I published result, while the dashed lines are the expected final sensitivities for MEG I and MEG II (adapted from (21)).

2

Kinematics and Background

2.1 Decay Kinematics and Branching Ratio

The kinematics of the $\mu \to e\gamma$ decay in the center of mass reference frame are especially simple:

- Two daughter particles emitted simultaneously;
- Back-to-back decay, *i.e.* with relative angle 180°;
- Particle energy $E_{\gamma,e} = \frac{m_\mu}{2} = 52.8 MeV$.

For this reason, all muon decay experiments so far have used a stopping target for the beam and studied the decay in a condition where the laboratory frame *is* the rest frame. The positive muon (μ^+) is used, owing to the fact that μ^- has a large atomic capture cross section.

2.2 Physics Background

The physics background is given by the tail distributions of the radiative muon decay $\mu^+ \to e^+ \nu_e \bar{\nu_\mu} \gamma$ in the configuration where the two neutrinos carry very small momentum. The radiative decay width is expressed in terms of $x = 2E_e/m_\mu$ and $y = 2E_\gamma/m_\mu$, with the $\mu \to e\gamma$ signal region lying at $x = y = 1$. We show in particular the photon spectrum in Fig. 2.1. In the decay region the radiative width vanishes; however by taking into account the experimental resolutions δx and δy and integrating over the ranges $[1 - \delta x, 1]$ and $[1 - \delta y, 1]$, the probability for a decay event to fall in the signal

region is nonzero and can be computed. From Fig. 2.2 it can be seen that with detector resolutions on the $\sim 1\%$ scale, sensitivities of $10^{-15} \div 10^{-14}$ can be reached.

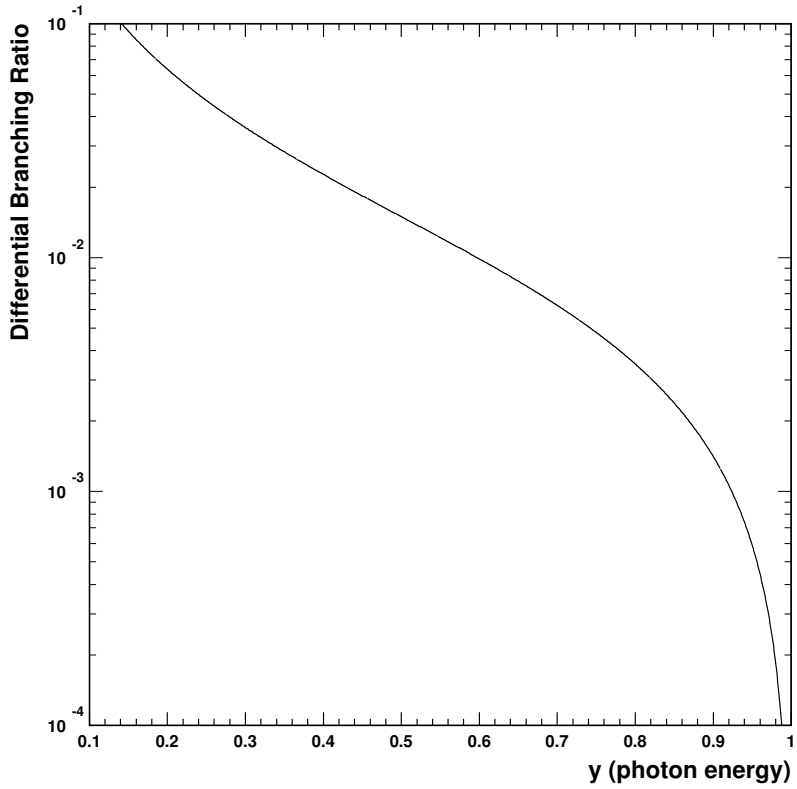

Figure 2.1: Energy spectrum of muons from radiative decay as a function of $y = 2E_\gamma/m_\mu$. (1)

2.3 Accidental Background

Accidental background originates from two distinct events producing a positron and a photon in temporal and spatial coincidence that closely match the event signature. With a very intense rate of incident muons, the accidental background becomes more important than the physics background. This is usually the case for the present and future experiments.

By using a muon beam we can guarantee that the only source of positrons is the muon decay. Photons can instead originate from multiple sources, such as radiative

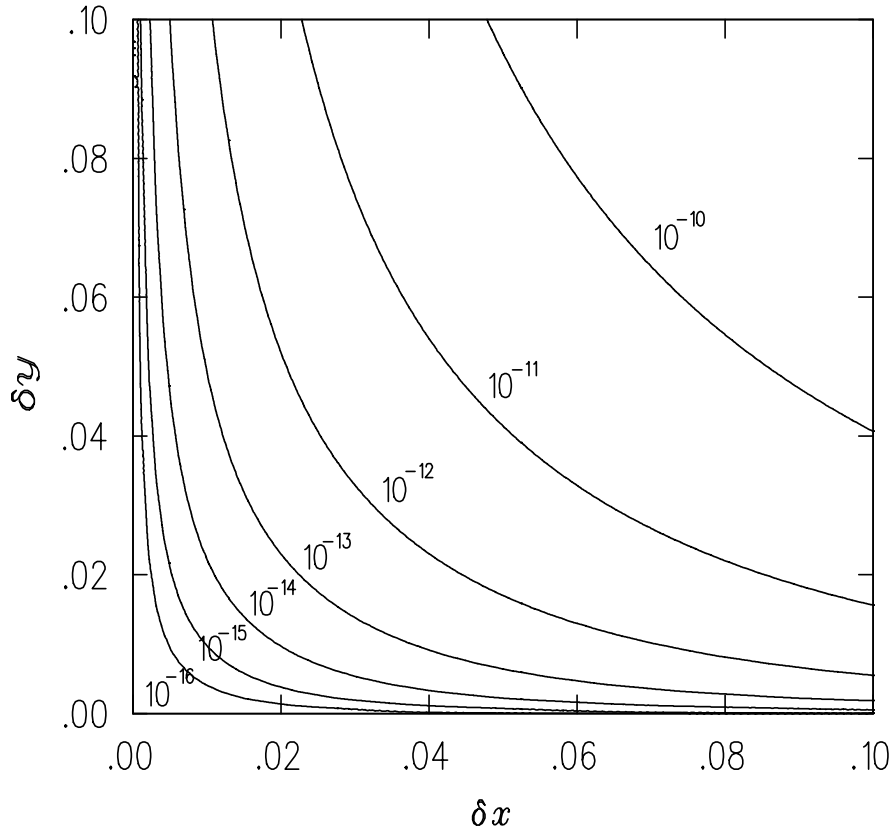

Figure 2.2: Fraction of radiative muon decay mistaken as $\mu \to e\gamma$ signal events as a function of of positron and γ energy resolutions. (1)

decays and positron annihilation in flight. Both those sources are dependent on muon rate; annihilation in flight is also dependent on the amount of material traversed. In Fig. 2.3 the integrated photon yield for photons near the signal region from both sources is shown (for annihilation in flight, a target thickness of 150 μm Mylar is assumed).

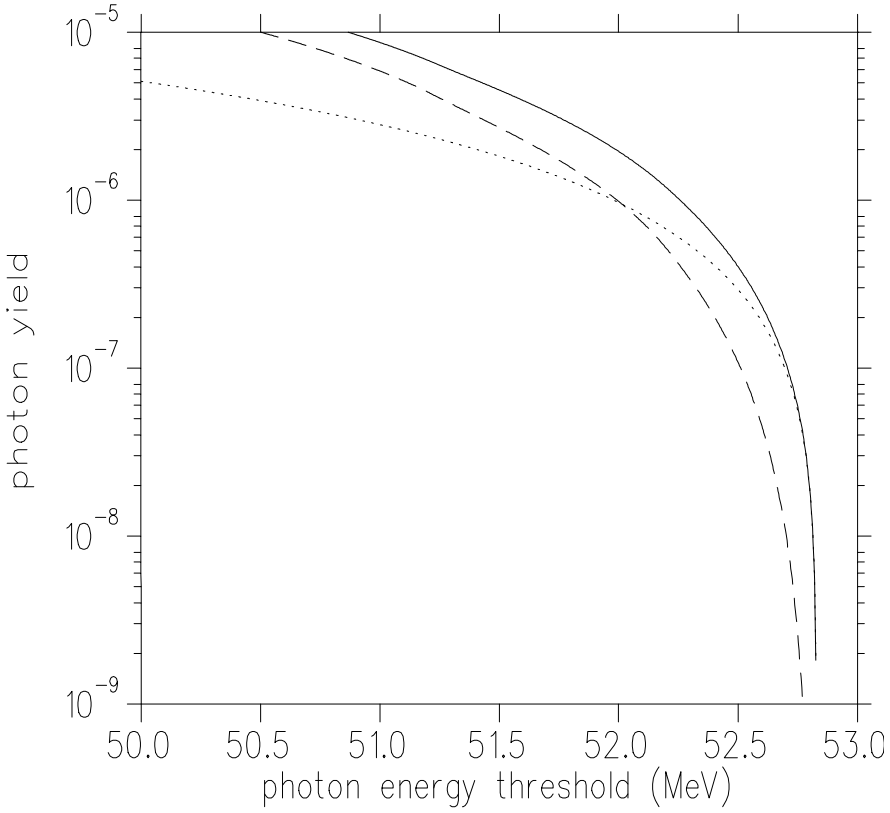

Figure 2.3: Integrated rates of backgrounds from annihilation in flight (dotted line) and radiative muon decay (dashed line). The solid line is the sum of the two. (1)

Integration over the positron energy spectrum (using the dominant Michel decay, $\mu^+ \to e^+\nu_e\bar{\nu_\mu}$), the γ spectra discussed above, and angular/temporal resolutions gives the rate of accidental coincidences

$$\mathrm{R_{acc}} \;=\; \frac{\alpha}{2(2\pi)^3}\mathrm{R_\mu^2}\delta\mathrm{x}(\delta\mathrm{y})^2\delta\mathrm{t_{e\gamma}}(\delta\theta_{\mathrm{e}\gamma})^2(\ln(\delta\mathrm{y}) + 7.33) \tag{2.1}$$

with R_μ being the muon beam rate.

We first notice that the rate scales quadratically with the photon energy resolution δy and the opening angle resolution $\delta\theta_{\mathrm{e}\gamma}$. Achieving a good resolution in these fields is thus extremely important.

Moreover, the accidental background scales quadratically with the muon rate. This imposes stringent constraints on the maximum beam intensity one can use in a $\mu \to e\gamma$ search.

Part II

The MEG I Experiment

3

MEG I Experimental Apparatus

3.1 Concept Overview

The aim of the MEG experiment is to measure the branching ratio of the rare muon decay $\mu \to e\gamma$ with a sensitivity of $\mathcal{O}\left(10^{-13}\right)$. In a rare decay search, as long as the background is maintained below the signal, the sensitivity is inversely proportional to the number of observed muons. Assuming an experiment running over the time scale of a few years (10^8 sec) and accounting for a 10% detection efficiency, an average stopping rate of $\approx 10^7$ μ/sec is required reach the desired sensitivity.

Current muon beam lines can be subdivided between *pulsed* and *continuous* beams. Pulsed beams feature muons grouped together in bunches separated by time delays. Continuous beams are designed to provide a constant flux of muons with no time separation.

As we have seen the accidental background is dominant and scales *quadratically* with the instantaneous muon rate because each daughter particle comes from a different muon, while $\mu \to e\gamma$ signal and the physics background instead scale linearly. A continuous muon beam is thus preferrable to a pulsed beam.

The requirements of a continuous beam along with a high rate of operation are satisfied by the currently most intense continuous muon source in the world, the one at the Paul Scherrer Institut (PSI) in Villigen, Switzerland.

The experiment comprises a thin polyethilene stopping target where the muon decay at rest occurs and two separate detectors to measure the kinematics of the decay products with the extreme precision required. The photon is revealed by a Liquid

Xenon (LXe) calorimeter while the positron momentum and direction are measured by a drift chamber (DC) placed in a inhomogeneous magnetic field and its timing is detected by a scintillating bar timing counter (TC).

A schematic of the detector is shown in Fig. 3.1

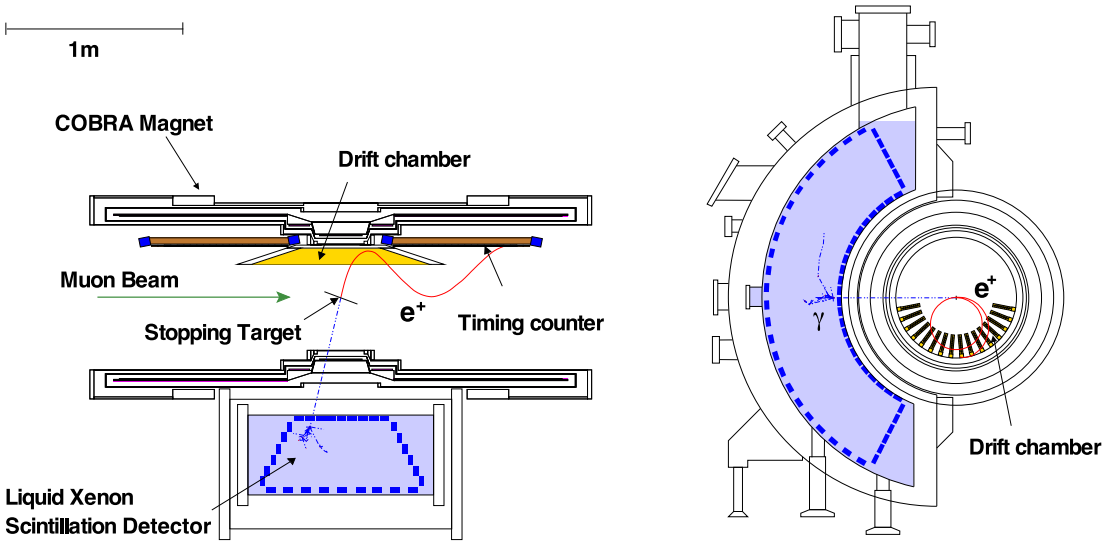

Figure 3.1: Schematic view of the MEG I detector with a simulated signal event.

To begin with, let us define a frame of reference to use in the upcoming sections. The choice of frame will be such that the z axis lies along the incoming beam direction, with the plane perpendicular to this direction being called the $r-\phi$ plane. To describe the apparatuse we will use rectangular (x, y, z), cylindrical (r, z, ϕ) or spherical (ρ, θ, ϕ) coordinates depending on convenience. The origin of the reference system $(x = y = z = 0)$ coincides with the center of the target, which is itself in the center of the experiment.

3.2 Beam and Target

A proton beam with an intensity of 1.8 mA is accelerated by a cyclotron to an energy of 590 MeV and transported to two production targets in sequence. The targets are rotating truncated cones of semi-aperture angle α composed of isotropic graphite and slanted with the same angle α with respect to the beam axis. The first target, called the M-target, is 7 mm thick, while the second one, called the E-target, can be either 40

or 60 mm thick in the proton beam direction. The proton interaction produces mainly pions, which decay both in flight and inside the graphite target, generating muons and electrons. Seven separate and simultaneously active beam lines branch out from the production targets.

The πE5 beam line used by the MEG experiment extracts low energy pions and muons from the E-target at an angle of 175° to the proton beam and is specifically tuned to collect so called *surface muons*, or muons produced by pion decay at rest. Pions at rest produce low energy (4 MeV) and low momentum (29 MeV/c) muons, which are trapped in the target unless originating from the target surface. The measured fluxes for the πE5 beam line are shown in Fig. 3.2 and clearly display the enhancement at 29 MeV/c caused by the surface muons.

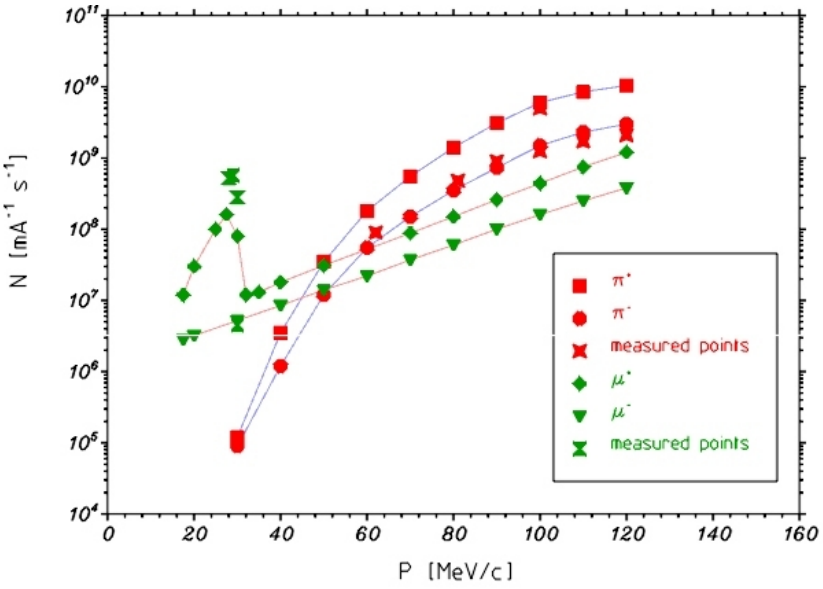

Figure 3.2: Muon and pion flux in the πE5 beam line as a function of momentum

The main characteristics of the πE5 beam line are listed in Tab. 3.1.

The choice of low energy muons is motivated by the need of a thin stopping target to minimize multiple scattering of decay positrons, which is one of the principal sources of uncertainty in a $\mu \to e\gamma$ search. In order to increase the stopping rate the beam must be further degraded.

The πE5 beam also contains a high component of positrons originating from muon

Parameter	Value
Length	10.4 m
Momentum range	$20 \div 120$ Mev/c
Momentum acceptance (FWHM)	10%
Momentum resolution (FWHM)	2%
Beam spot size (FWHM)	15×20 mm^2
Horizontal divergence (FWHM)	450 mrad
Vertical divergence (FWHM)	120 mrad

Table 3.1: πE5 beam line properties. (22)

decays and photon pair production in the target. This component must be eliminated, as it would otherwise produce a high rate background in the detector, either from the positrons themselves crossing the spectrometer or from the photons produced by their annihilation.

3.2.1 The MEG Beamline

The beam line leading up to the experiment manipulates the beam in order to:

1. Reduce the spurious positron component of the beam;
2. Reduce the muon momentum to allow for a thin stopping target;
3. Couple the beam line to the MEG superconducting magnet.

The beam line structure can be seen in Fig. 3.3.

It is composed of:

- A quadrupole triplet, used to re-focus the beam after the bending magnet;
- An electrostatic separator (Wien filter) to reduce the positron component of the beam. Acting as a velocity selector, the filter creates a spatial separation between muons and positrons equal to 11 cm at a distance of about 2 m from the target, as shown in Fig. 3.4. This is equivalent to 7σ, where σ is the combined RMS of the two beam envelopes. After the separator, the positron component of the muon beam amounts to less than 1%.

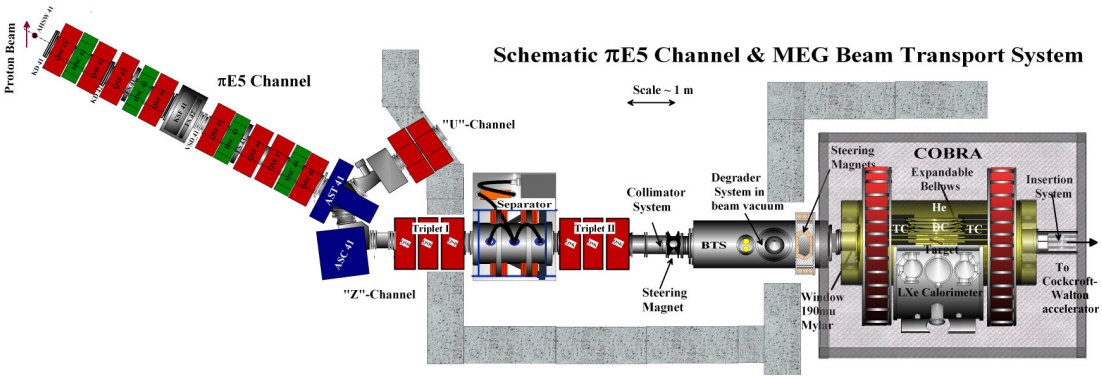

Figure 3.3: Schematic of the πE5 channel and MEG beam transport system.

- A second quadrupole triplet to re-focus after the filter.
- A beam transport solenoid (BTS) to couple the beam with the COBRA magnet field. A polyethylene foil is placed in the solenoid focus to act as a muon momentum degrader.

The resulting muon beam has an intensity of $3 \times 10^7 \mu^+$/sec and is focused in an ellipsoidal spot on the target with transverse dimensions $\sigma_x = 10$ mm and $\sigma_y = 11$ mm at the COBRA center.

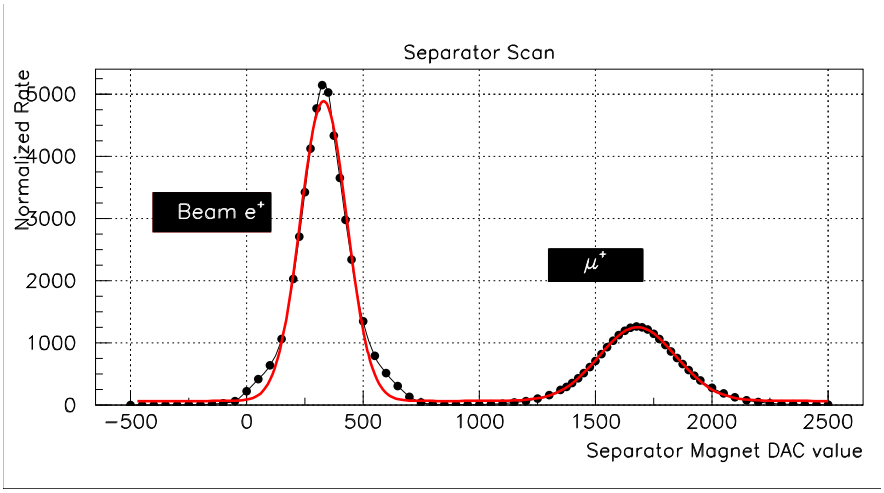

Figure 3.4: Scan plot showing separation of the positron and muon beam components.

3.2.2 The Target

The target is a 205 μm thick, elliptical sheet of polyethylene with semi-major and semi-minor axes of 10 cm and 4 cm, set at 20.5° with respect to the beam axis to increase the target thickness crossed by the muons and to minimize the thickness traversed by the decay positron.

The target system is immersed in a He atmosphere to minimize multiple scattering and mounted on an actuated support that allows it to be moved from the measuring position to a parking position upstream along the beam line and 20 cm away from the COBRA center. Six holes of radius 0.5 cm are punched in the target allow for software verification of the target plane position and measure the tracking capabilities on decay vertex reconstruction.

3.3 Positron Detector

The positron tracker is immersed in an inhomogeneous magnetic field providing two significant advantages:

1. Positrons emitted close to 90° to the magnetic field axis are quickly expelled from the tracking region (Fig. 3.5.a) while in a uniform field they would loop multiple times inside the chamber, increasing occupancy and lowering detector performance;

2. In a constant field the radius of positron trajectory on the transverse plane is dependent on the transverse momentum p_t. The MEG solenoid is instead shaped so that the radius of positron tracks is dependent on total momentum, simplifying the search for high momentum tracks (Fig. 3.5.b). This gives the magnet its acronym: COBRA (COnstant Bending RAdius)

3.3.1 COBRA Magnet

COBRA is a Niobium-Titanium superconducting magnet composed of five coils of different radius: a central coil, two gradient coils and two end coils, which are in turn separated into inner and outer parts with different current densities. The variable field,

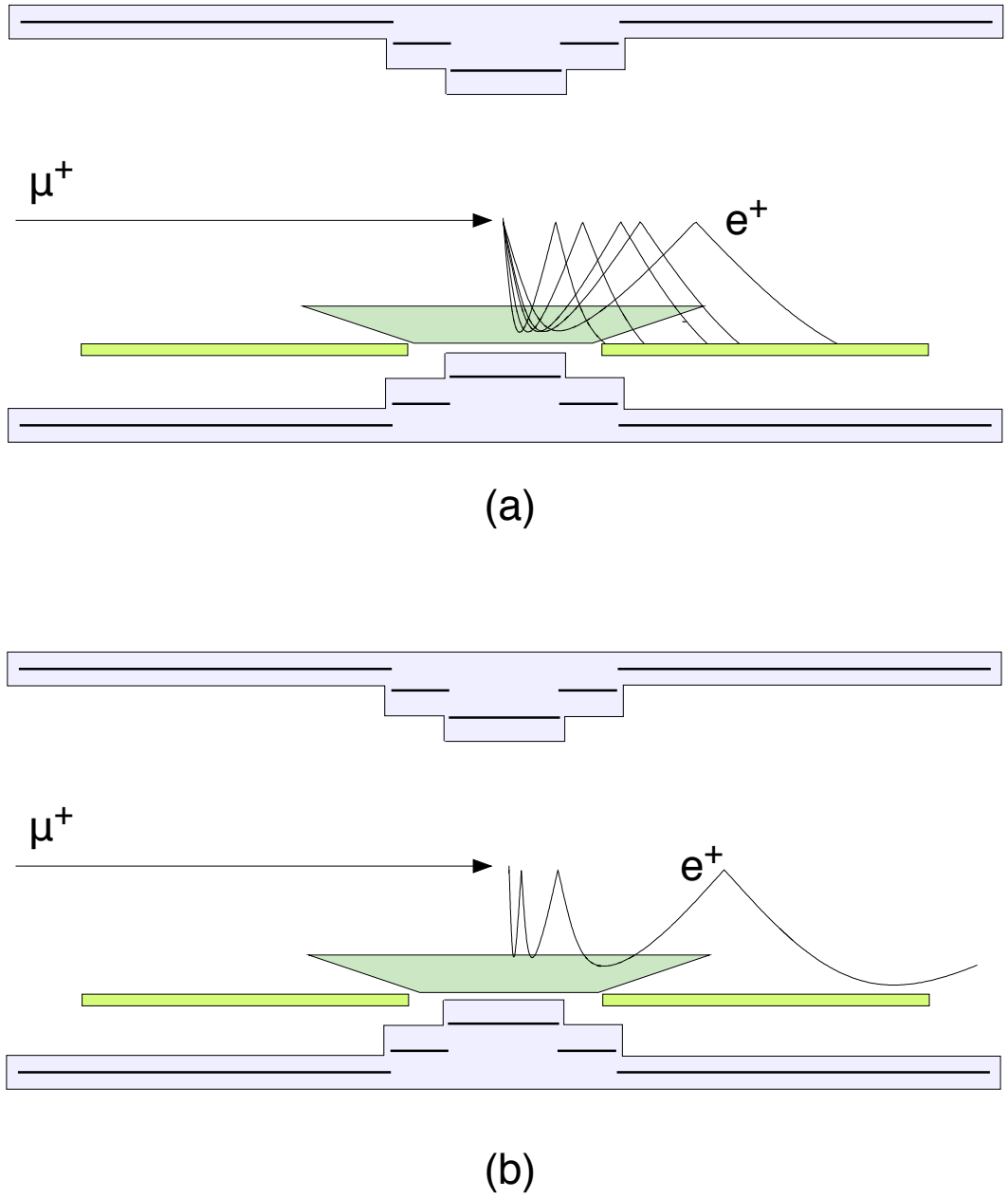

Figure 3.5: Behavior of charged tracks in a gradient magnetic field. Particle bending radius is independent from emission angle (a) and particles emitted at $\cos\theta \sim 0$ are quickly swept out of the tracker volume (b).

obtained by changing the winding density in each coil, achieves a maximum value of 1.27 Tesla at the magnet center and 0.49 at either end.

Photomultipliers tubes are sensitive to magnetic fields, suffering from reduced gain which in turn leads to degraded detector performance. A pair of non-superconducting compensation coils (Fig. 3.6) placed at the extremities are used to reduce the stray field in the photon detector zone to less than 50 Gauss, a level tolerable for photomultiplier operation.

The magnet thickness is reduced as low as 0.197 X_0 in the acceptance region of the photon detector ($|\cos(\theta)| \leq 0.35$), so that photons originating from the target can traverse it.

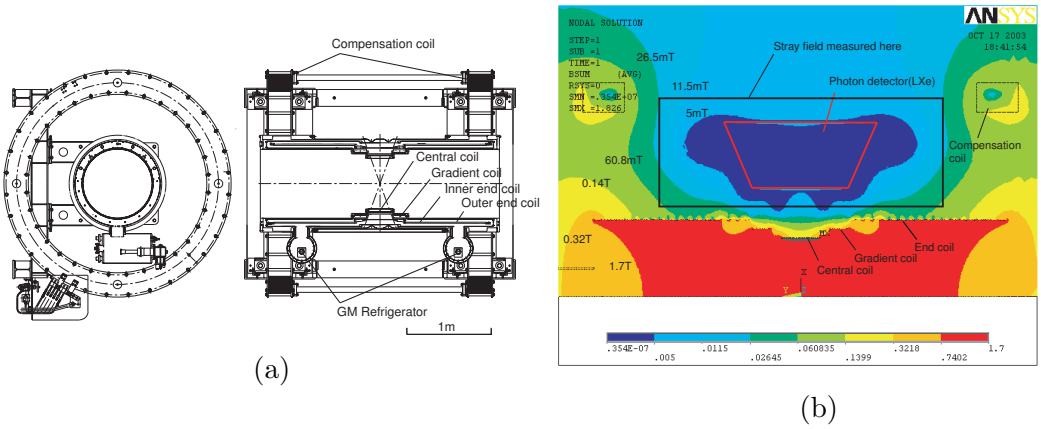

Figure 3.6: Cross section drawing of the COBRA magnet (a) and magnetic field map in the LXe detector region (b).

3.3.2 Drift Chamber

The MEG drift chamber system is composed of 16 trapezoidal modules spaced by 10.5° intervals of azimuthal angle (Fig. 3.7 and 3.8). Each sector consists of two staggered arrays of drift cells (Fig. 3.9) to solve the left-right ambiguity. The sensitive area of the chamber covers the radius of $r = 19.3$ cm to $r = 27.0$ cm and the longitudinal region of $|z| \leq 50$ cm.

The chamber walls are composed of thin (12.5 μm) plastic foils covered in a 250 nm thick aluminium deposit, etched in a 5 cm zig-zag pattern to make a *Vernier pad* (23). An initial estimate of the z position of the hit can be obtained from the ratio of collected

charge at each end of the hit wire, with an accuracy of 1 cm. A comparison between the charge deposits on the two parts of the vernier pad can then be used to improve the single hit resolutions to the level of $\sigma_z \approx 800$ μm, while the single hit resolution on the radial coordinate is $\sigma_r \approx 200$ μm.

The chamber structure is mounted on carbon fiber frames which are open towards the target, and immersed in a 50/50 He:C_2H_6 mixture, chosen to minimize multiple scattering on e^+ trajectories while allowing for sufficient ionization loss in the chamber. While the open frame structure makes wire and foil stretching challenging, it greatly reduceds the amount of material traversed by positrons: a typical 52.8 MeV/c positron only crosses 2×10^{-3} X_0 along its track.

The overall detector angular resolution is obtained from events where the positron makes two turns in the chamber. By treating each turn as an independent track, one can extract the resolution from the difference between measured angles. This gives a resolution of $\sigma_{\theta_e} = 9.4 \pm 0.5$ mrad and $\sigma_{\phi_e} = 8.4 \pm 1.4$ mrad.

The positron energy resolution is measured with a fit of the energy distribution to the Michel spectrum convolved with a double gaussian resolution function. The core component (79%) gives an average resolution of $\sigma_{E_e} = 330 \pm 16$ KeV

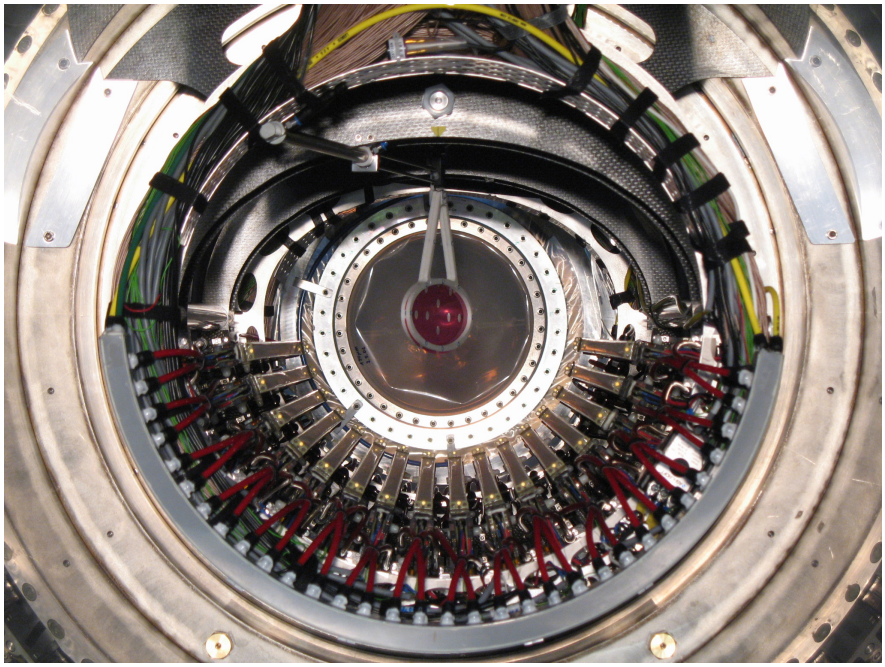

Figure 3.7: Downstream view of the MEG Target and DC system.

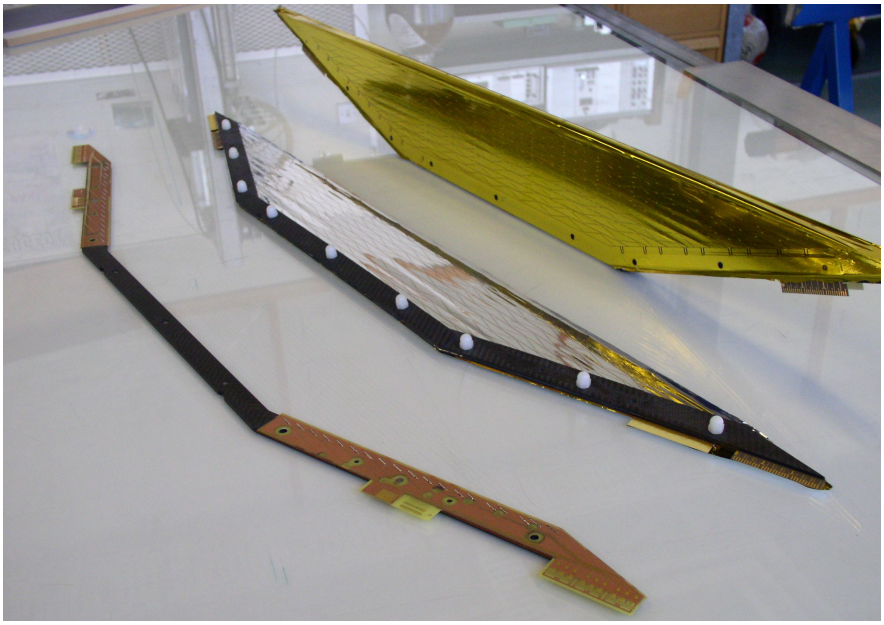

Figure 3.8: Components of a DC module: anode frame with wires (front), middle cathode and hood cathode (back).

3.3.3 Timing Counter

The timing counter purpose is to precisely measure positron time of flight and provide a fast determination of positron direction for trigger purposes. It is composed of two barrel-shaped sections (Fig. 3.10), placed with their axis of symmetry aligned with the z axis, starting at 31 cm upstream and downstream from the target respectively The sections occupy the region $31 \leq |z| \leq 111$ cm and cover 145° in the ϕ coordinate, allowing for full angular coverage for positrons from $\mu \to e\gamma$ decays when the photon points to the LXe detector.

Each section consists of 15 bars of BC404 plastic scintillator bars of square section and size $80 \times 4 \times 4$ cm^3, aligned along the z axis. Each bar is read out by a couple of fine mesh $2''$ PMTs glued at the ends. These detectors can measure the positron time of flight with an overall resolution of $\sigma_{t_e} \approx 100$ ps.

The bars are overlapped on the inner side with a series of 256 scintillating fibers oriented along the ϕ direction. The fibers have a 0.5×0.5 cm^2 square section and are read by avalanche photodiodes (APDs). Together, the two layers provide a measurement of the positron impact position on the TC for trigger and reconstruction purposes.

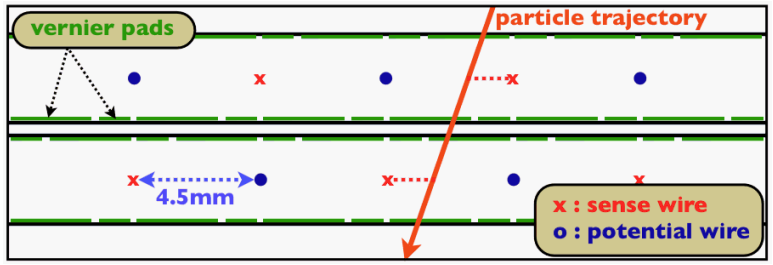

(a)

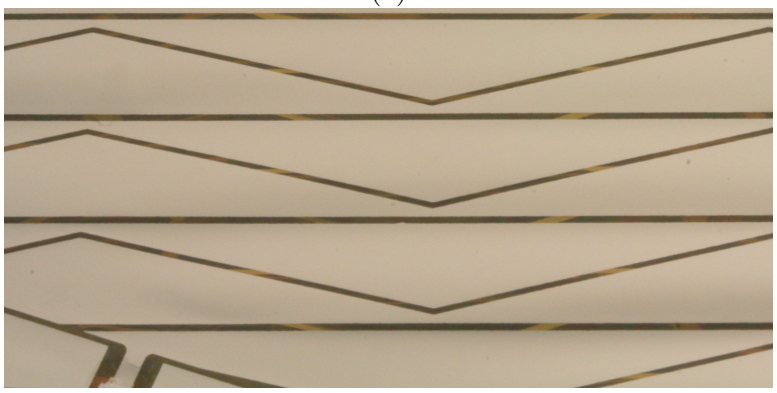

(b)

Figure 3.9: (a) Schematic view of the DC cell structure in the $x - y$ plane. (b) Close-up view of the Vernier pads etched on the cathode foil.

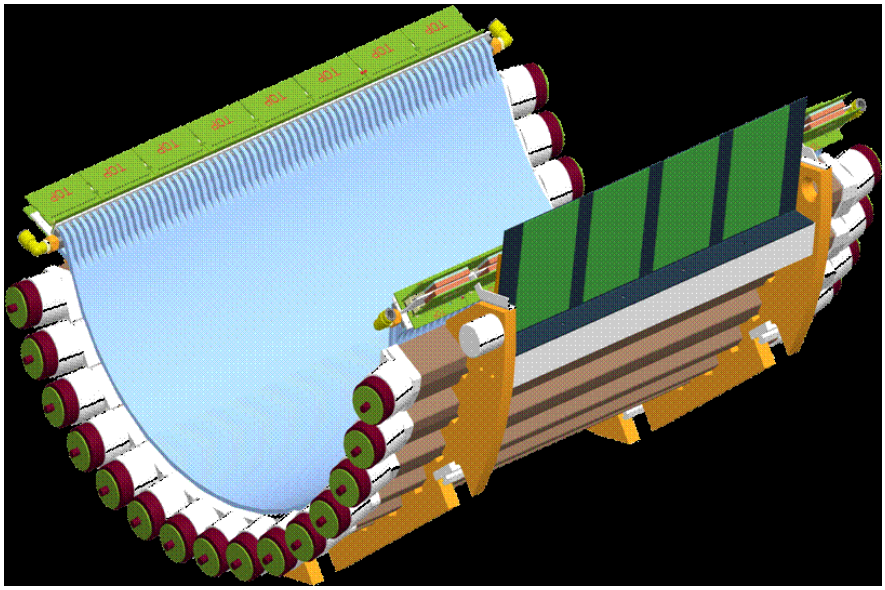

Figure 3.10: Three-dimensional view of a TC sector, with the scintillating fibers (light blue) overlapping the scintillator bars (brown).

PMTs have limited lifetimes when immersed in rich He atmospheres. For this reason, each of the two TC sections is wrapped in a plastic bag flushed with N_2 to isolate it from the tracker.

3.4 Gamma Detector

The MEG experiment requires an extremely precise determination of photon observables to minimize the number of accidental coincidences, which constitute the dominant background process. The adopted solution is a scintillating detector based on liquid Xenon scintillation.

3.4.1 Scintillation in Liquid Xenon

Xenon has, among noble gases, the advantage of having a high boiling point (165 K at 1 atm), a high atomic number (Z = 54) and high density in liquid phase ($\rho = 2.95$ g/cm^3) making for an excellent calorimeter with low radiation length ($X_0 = 2.77$ cm). The general properties of LXe are summarized in Tab. 3.2.

Properties	Value
Atomic/Mass number	54 / 131.293
Density at 161.4K	2.978 g/cm^3
Boiling/Melting point	165.1/161.4 K
Radiation length	2.77 cm
Moliere radius	4.20 cm
Scintillation wavelength	178 nm
W_{ph} for electron / α	21.6 eV / 17.9 eV
Decay time (recombination)	45 ns
Decay time (Fast/Slow component)	4.2 ns/22 ns
Absorption length	>100 cm

Table 3.2: Salient optical properties of liquid Xenon.

Scintillation processes in liquid Xenon produce a high amount of photons per unit of energy deposit, comparable to inorganic scintillators such as NaI(Tl), allowing for an excellent energy resolution. Moreover, the short scintillation times simultaneously

makes achieving the time resolutions and significantly reduce the probability of pile-up events.

LXe scintillation occurs in Vacuum Ultra Violet (VUV) at a wavelength of $\lambda = 178$ nm through the formation and subsequent decay of the excited atomic bound state Xe_2^*. LXe is consequently transparent to its own scintillation light, with an absorption length larger than the detector scale ($\lambda_{abs} > 300$ cm). Ionization charges are also produced by particle interactions, but are not collected in order to simplify the reconstruction and obtain a prompt detector response.

The presence of even small concentrations of impurities such as O_2, H_2O and N_2 can drastically reduce the detector transparency and thus require efficient and continuous elimination.

For this reason, double purification system has been designed for use in both gas and liquid phases. Gas phase impurities are removed by means of a metal-heated getter, while liquid phase Xenon is purified through a cryogenic centrifugal pump and molecular sieves.

3.4.2 Detector Geometry

The MEG photon detector is a C shaped, homogeneous liquid Xenon calorimeter covering the angular region defined by $|\cos(\theta)| \leq 0.53$ and $120^\circ < \phi < 240^\circ$, corresponding to 11% of the solid angle. It is positioned outside COBRA with an inner radius $R_{in} = 67.85$ cm and is 38.5 cm deep, equivalent to ≈ 14 X_0, fully containing a 52.8 MeV γ shower. The active volume of the detector is ~ 800 ℓ.

A schematic of the photon detector layout is shown in Fig. 3.11.

The cryostat surrounding the detector volume is designed to reduce the material traversed by incident γ-rays. The window of the outer vessel consists of a thin (0.4 cm) stainless steel plate, while the inner vessel is made of aluminum honeycomb panels covered with carbon-fiber plates for a total thickness as low as 0.075 X_0.

The scintillation light is collected by 846 internally mounted $2''$ PMTs (24) submerged in LXe and surrounding the active volume. They are mounted on an aluminum support structure with an inner face made of polyether ether ketone (PEEK) The PMTs are operated at LXe temperature ($\sim$ 165 K) and equipped with VUV-transparent quartz windows and bialkali photocathodes sensitive to VUV light.

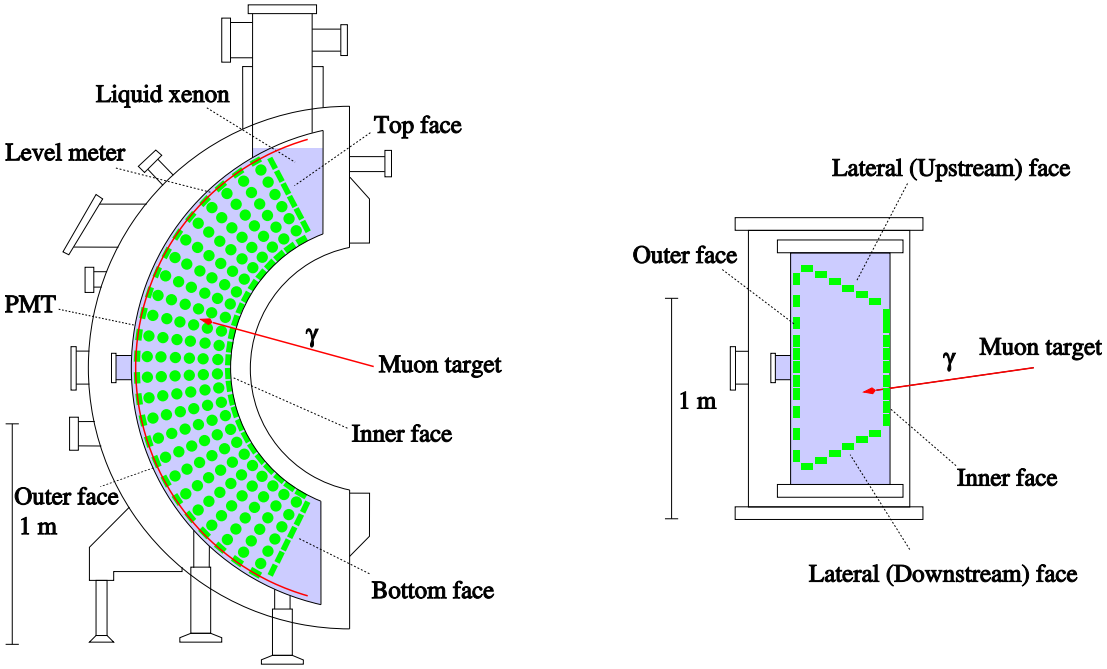

Figure 3.11: Schematic view of the LXe detector: from the side (left) and from the top (right).

When referring to the LXe calorimeter, a special internal coordinate system (u,v,w) will be used, where:

- u coincides with z in the MEG coordinate system;
- v is the direction along the inner face from bottom to top at $r = R_{in} = 67.85$;
- and $w = r - R_{in}$ measures the depth from the inner face.

3.4.3 Detector Calibration

Calorimeter stability and performance are continuously monitored during data taking using numerous calibration tools. The reason is twofold: first to promptly detect apparatus malfunctioning or misbehaviour, and second to properly account for systematic uncertainties in the measured physical variables, acceptances and thresholds.

3.4.3.1 LED Calibration

A system of 44 blue LEDs is installed inside the detector to determine the PMT gains and as a check for detector stability. LEDs are flashed on average every second day

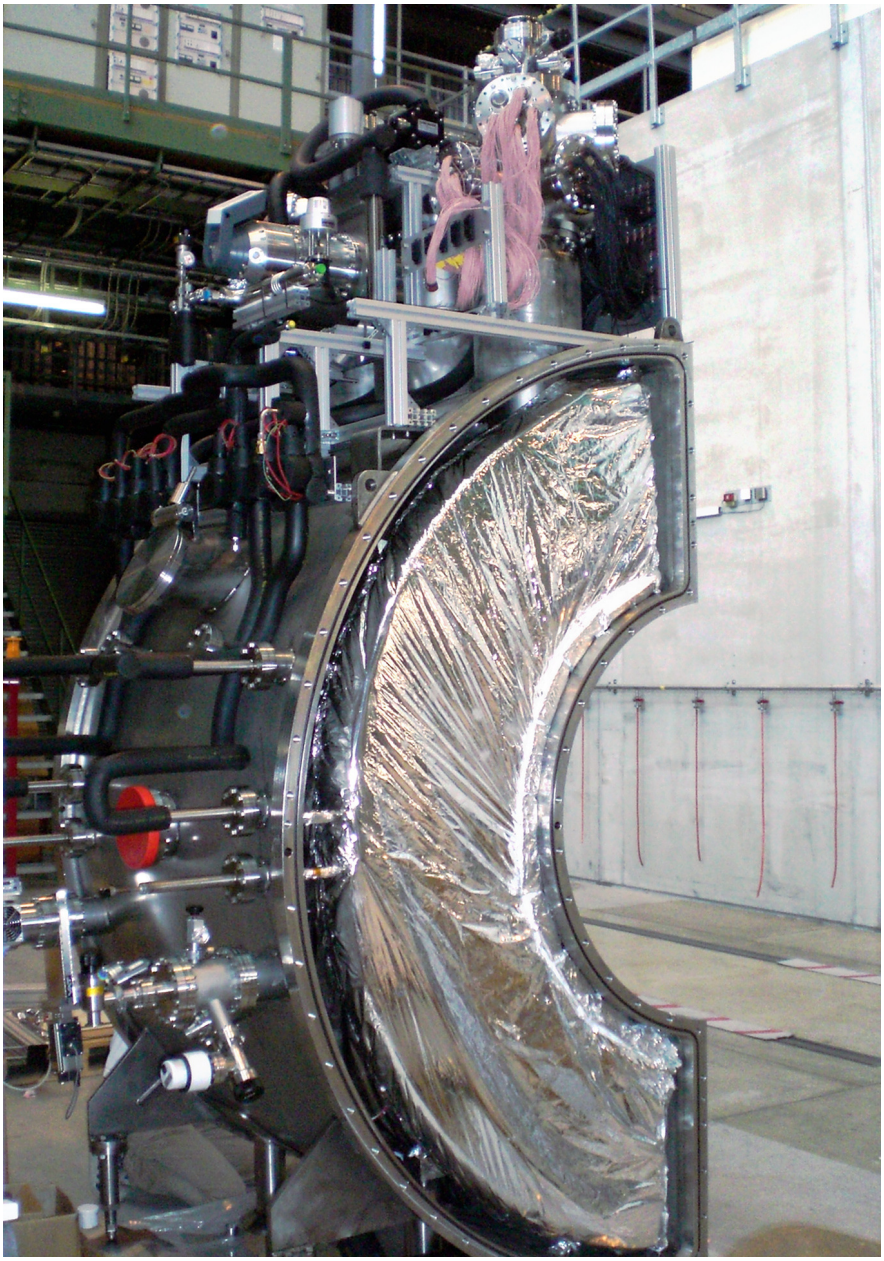

Figure 3.12: The LXe detector under construction, showing the open cryostat

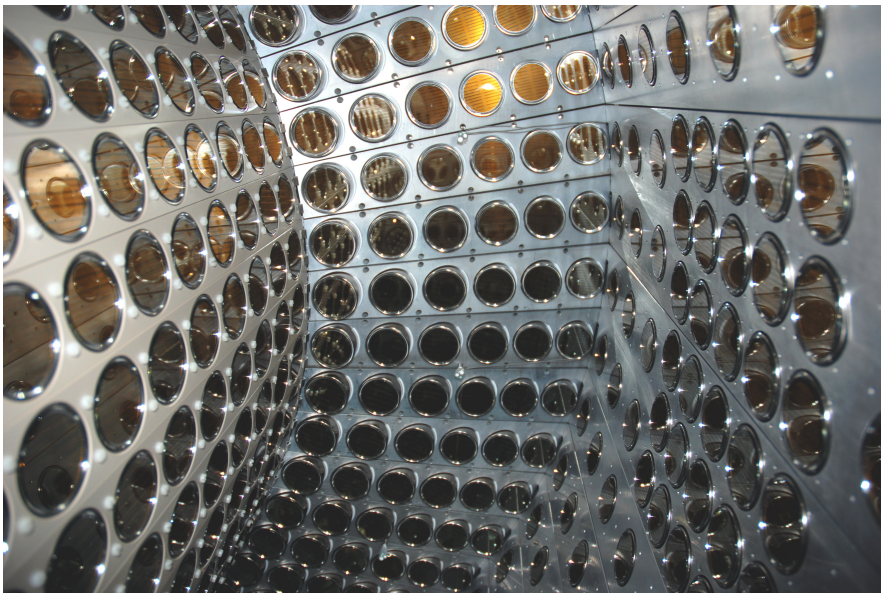

Figure 3.13: Internal view of the LXe detector, showing the 846 PMTs mounted on the inside.

at different light intensities during dedicated runs, and the gains are evaluated from photelectron statistics as follows:

Suppose that N photoelectrons are emitted by the photocathode as a result of exposure to scintillation light. The collected charge on the anode will then be:

$$q = gN + q_0 \tag{3.1}$$

where g is the PMT gain and q_0 is the offset arising from baseline fluctuations. The photoelectron distribution obeys poissonian statistics, so that

$$\sigma^2 = g^2 N + \sigma_0^2 \tag{3.2}$$

where σ_0 is the baseline standard deviation. Then combining Eq. 3.1 and 3.2

$$\sigma^2 = g(q - q_0) + \sigma_0^2 \tag{3.3}$$

and thus g can be extracted by fitting σ^2 as a function of pedestal-subtracted charge, as shown in Fig. 3.14.

Typical PMT gains are $g \approx 10^6$ and decrease on average by 0.1%/day during data taking, which is solved by periodically increasing the supply voltage.

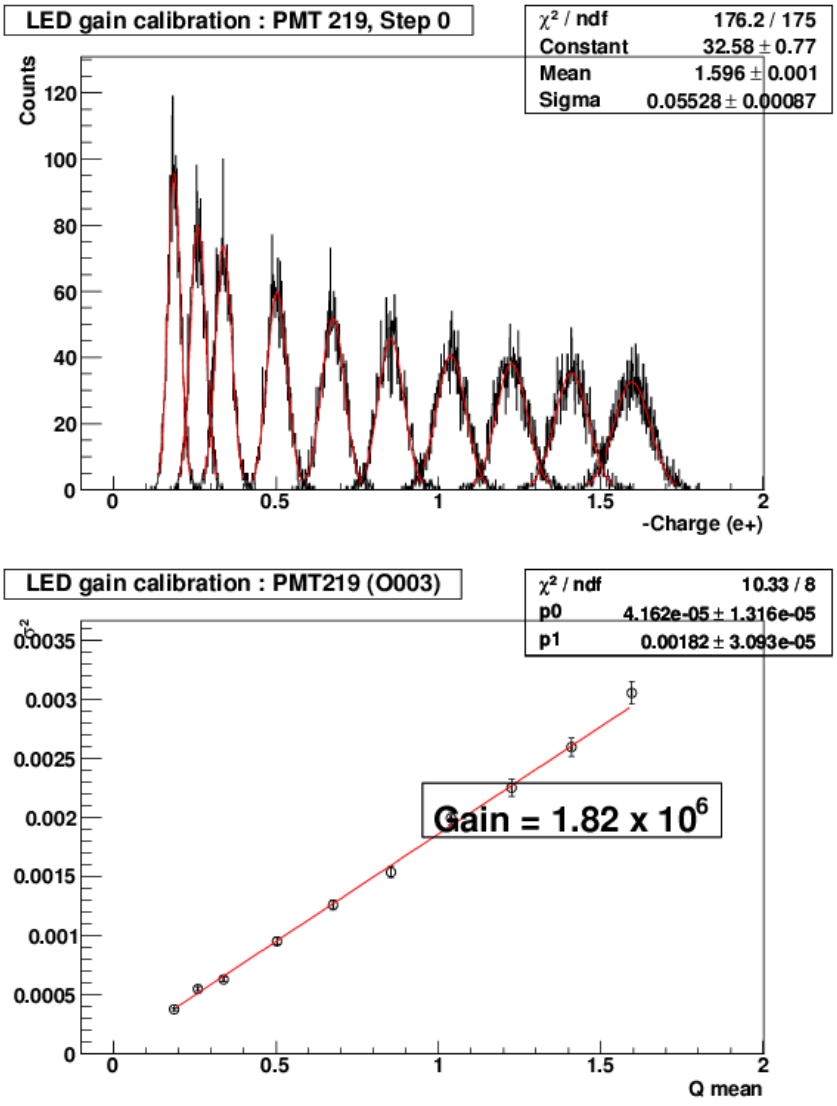

Figure 3.14: Example of gain measurement

LEDs are also flashed at a frequency of 0.2 Hz during physics runs; the peak position is used to monitor detector stability and to bridge the gain variations between two separate gain measurements.

3.4.3.2 Point-like α-sources

Quantum efficiency (QE) is an individual property of each PMT determined by differences between photocathodes arising during production. Precise knowledge of each QE is essential to reconstruct the γ observables from collected PMT charge.

Individual PMT QEs are measured using 25 ^{241}Am sources deposited on five 50 μm diameter wires, strung parallel to the beam direction and anchored to the calorimeter walls. The sources emit 5.44 MeV α particles with an activity of $|sim1|$ kBq each and are placed in a staggered fashion to optimise the range of angles and distances they are viewed from by PMTs.

The α particles are emitted from known positions and have very short range in LXe ($\sim$ 40 μm), making events easy to simulate. Each QE can be extracted by comparing the individual α-peak charges to those from a detailed Monte Carlo simulation.

The same comparison can be used to extract an estimate of LXe attenuation length (25). The combined α-peak from all sources provides a reference to control the LXe light yield and transparency.

Reconstruction of α-sources is different depending on the Xenon phase. As the range of α-sources in gaseous Xenon (GXe) is $\sim$ 8 mm, their position is reconstructed as a $\sim$ 1 cm diameter 3-dimensional spot. The range in LXe is much smaller ($\sim$ 40 μm), comparable to the wire diameter (100 μm). This causes roughly 50% of scintillation light to impinge on the source wire, creating a shadow effect. The source positions are thus reconstructed as rings surrounding the wire (Fig. 3.15).

In addition, simulation of LXe scintillation is in general more complex than in GXe and requires precise knowledge of the optical properties of the detector (attenuation lenght, refraction indexes, etc.), while the latter is a much simpler process, benefiting from an essentially infinite attenuation lenght and a refraction index $n_{GXe} \simeq 1$,

However, while simpler, α-source data can only be acquired in GXe twice a year, at the beginning and end of the run. Consequently, in order to monitor sudden changes in PMT behavior and precisely calibrate the detector during data taking, QEs are usually extracted from data acquired in LXe during the course of the year.

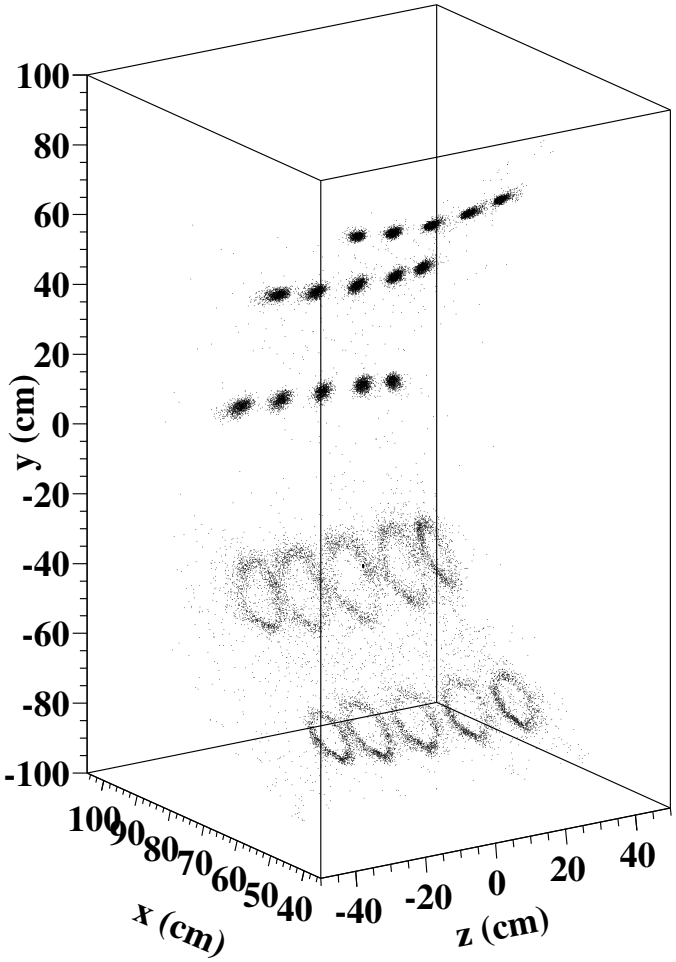

Figure 3.15: Reconstructed position of the 25 α-sources inside the detector during the Xenon liquefaction process. Part of the detector is filled with LXe, showing the different position recosntruction of sources in GXe and LXe.

3.4.3.3 Cockroft-Walton Accelerator

A dedicated Cockroft-Walton (CW) proton accelerator is used to calibrate the calorimeter energy scale and TC-LXe relative timing. It is placed downstream from the MEG detector (Fig. 3.16) and delivers a proton beam to induce nuclear reactions on a lithium tetraborate ($Li_2B_4O_7$) target, which is inserted in place of the muon target during calibrations by means of an extendable bellows system.

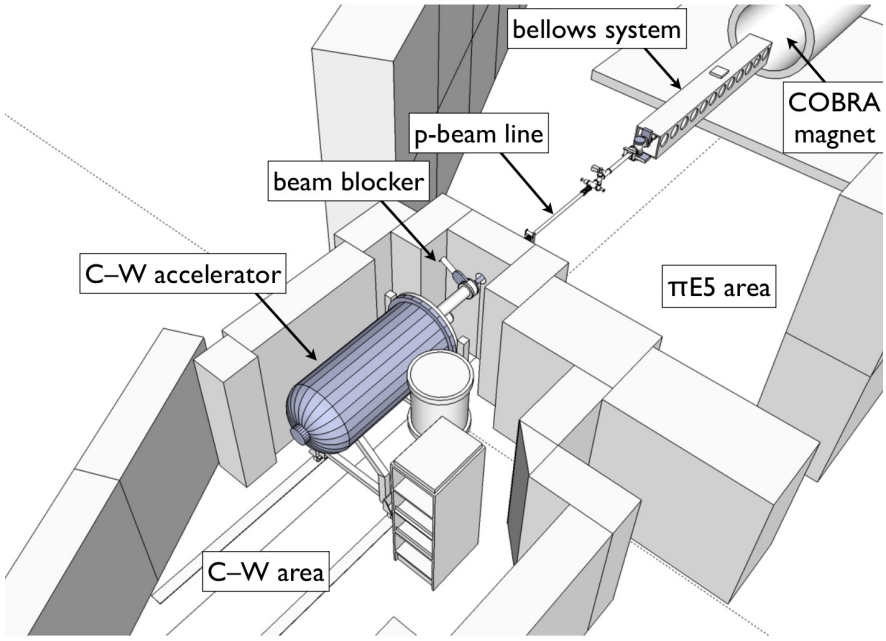

Figure 3.16: Placement of the CW accelerator beam line with respect to the MEG experimental area.

The lithium capture reaction $^7\mathrm{L}i(p,\gamma_{17.6})^8\mathrm{B}e$ has a threshold at a proton energy of 440 KeV and a peak cross section of $\sigma_{Li} \sim 6$ mbarn. It produces monochromatic 17.6 MeV γ-rays with the addition of a broad resonance centred at 14.8 MeV. This monochromatic signal provides a fast and reliable calibration point at $\sim$ 1/3 of the signal energy.

The boron capture reaction $^{11}\mathrm{B}(p,\gamma_{4.4}\gamma_{11.6})^{12}\mathrm{C}$ has a threshold at a proton energy of 163 KeV, with peak cross section of $\sigma_{Li} \sim 2$ mbarn. It produces a pair of simultaneous γ-rays of 4.4 MeV and 11.6 MeV. This reaction can be used to measure the relative timing of the LXe detector and TC scintillating bars and provides two additional energy

calibration points.

Together, these calibration processes provide a constant monitoring of the γ energy scale, which can be known at the few-per-mil level, and a LXe-TC time alignment better than 20 ps. CW data is acquired two to three times per week.

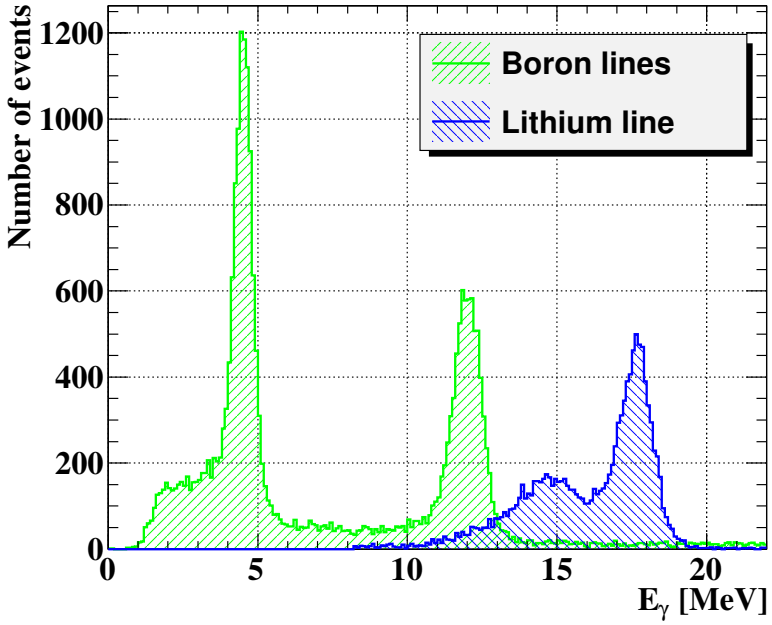

Figure 3.17: Cockroft-Walton calibration lines from γ-rays emitted by Lithium (17.6 MeV) and Boron (4.4 and 11.6 MeV) capture processes

3.4.3.4 Neutron Generator

Calorimeter calibration and monitoring during beam-on conditions is handled through the use of 9.0 MeV γ-rays produced by neutron capture in nickel.

Neutrons are produced with a pulsed D-D generator by means of the $d(d,^3\mathrm{He})n$ nuclear reaction at an energy of 2.5 MeV. The neutron generator is placed inside a polyethilene block (Fig. 3.18) positioned in front of the LXe detector, of which the calorimeter-facing side consists of alternating slabs of nickel and polyethylene. A large fraction of the neutrons are thermalized in polyethylene and then captured by nickel nuclei.

Nickel has a relatively large probability ($\sim$ 34%) of producing a single photon at 9.0 MeV through the $^{58}\mathrm{Ni}(n,\gamma_{9.0})^{59}\mathrm{Ni}$ process. The overall sandwitch structure surrounding the generator is designed to maximize the fraction of such γ-rays emitted in the LXe detector direction. Additionally, the structure minimizes the outgoing flux of both thermalized and unthermalized neutrons in order to avoid material activations and neutron interactions in the detector.

By exploiting the pulsed mode of the generator in conjunction with a dedicated trigger, it is possible to acquire calibration data during data taking and study the detector response when illuminated by the beam, as well as check the detector behavior during variations of beam intensity.

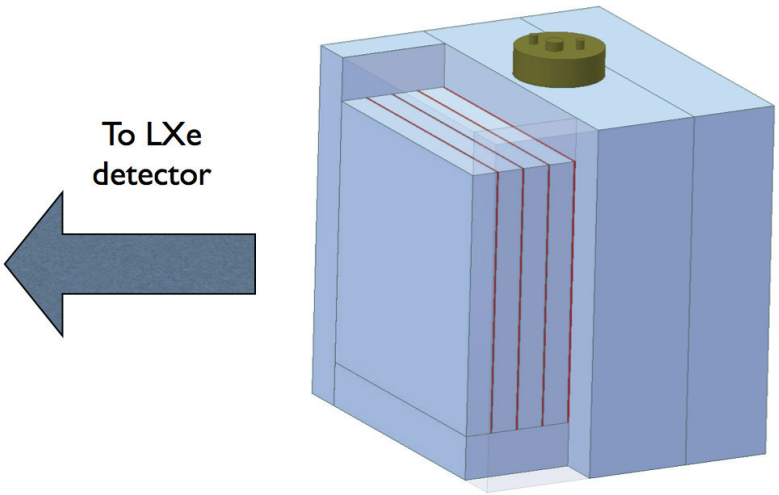

Figure 3.18: Schematic of the neutron generator setup, showing the moderator (blue) and nickel slabs (red)

3.4.3.5 Charge Exchange Reaction

A calibration technique based on γ-rays from neutral pion decay ($\pi^0 \to \gamma\gamma$) has been developed in order to provide the nearest possible calibration point to the MEG signal energy. Neutral pions are produced in the charge exchange (CEX) reaction at rest $\pi^- p \to \pi^0 n$ with a momentum of $\sim$ 2.9 MeV/c in the laboratory frame. In 98.8% of

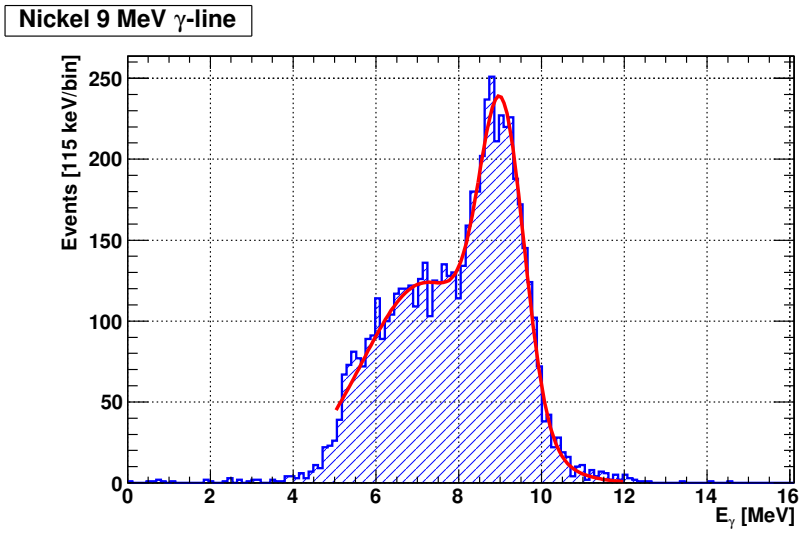

Figure 3.19: 9.0 MeV line from ^{5}8Ni capture seen in the LXe detector.

cases, the pion decays immediately in two photons, which in the mother particle rest frame are emitted back-to-back with an energy

$$E_{\gamma}^{*} = \frac{m_{\pi^0}}{2} \simeq 67.5 \text{ MeV} \tag{3.4}$$

In the lab frame, accounting for the Lorentz boost, the photon energies are

$$E_{\gamma_{1,2}} = \gamma \frac{m_{\pi^0}}{2} \left(1 \pm \beta \cos\theta^{*}\right) \tag{3.5}$$

where β is the π^0 velocity and θ^{*} the angle of photon emission in the rest frame. By differentiating Eq. 3.5 we obtain the energy spectrum of the two photons in the lab frame

$$\frac{\mathrm{d}N}{\mathrm{d}E_{\gamma}} = \frac{\mathrm{d}N}{\mathrm{d}\cos\theta^{*}} \times \frac{\mathrm{d}\cos\theta^{*}}{\mathrm{d}E_{\gamma}} \tag{3.6}$$

which is a flat spectrum between the values

$$E_{\gamma}^{min} = \frac{m_{\pi^0}}{2}\sqrt{\frac{1-\beta}{1+\beta}} \simeq 54.9\text{MeV} \qquad E_{\gamma}^{max} = \frac{m_{\pi^0}}{2}\sqrt{\frac{1+\beta}{1-\beta}} \simeq 82.9\text{MeV}. \tag{3.7}$$

The minimum and maximum photon energies are obtained when the photons are emitted in the π^0 flying direction, corresponding to a laboratory opening angle of 180°. It is thus possible to select photons of definite energy by tagging the brother particle flying in the opposite direction.

A π^- beam of 70.5 MeV/c is obtained by adjusting the πE5 beamline magnet current and polarity. The target used for the CEX reaction is a 50 mm diameter, 75 mm long cylinder filled with liquid hydrogen (LH_2) at 20 K and equipped with thin Mylar windows to minimize pion multiple scattering. It is cooled by a continuous flow of liquid helium and inserted in place of the muon target. A schematic of the target is shown in Fig. 3.20

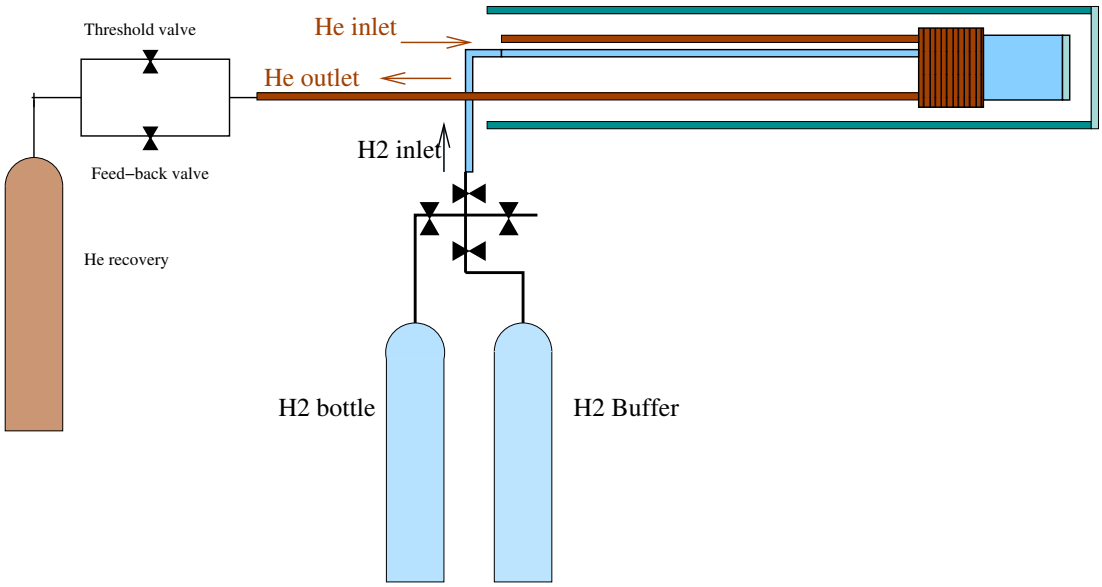

Figure 3.20: Scheme of the LH_2 target

Back-to-back γ-rays are selected with a detector mounted on a movable, remotely controlled stage (Fig. 3.21.a) pointing towards the center of the LH_2 target. By requiring an opening angle larger than 170°, photons can be selected with an energy spread $\sigma_{E_\gamma}/E_\gamma < 1\%$.

Up to 2009, the detector consisted of nine NaI(Tl) scyntillator crystals, with two removable layers of lead and plastic scintillator, for a total thickness of ≈ 0.3 X_0, used for timing measurements. Each crystal has dimensions $62.5 \times 62.5 \times 305$ mm^3 and is read by a 10×10 mm^2 APD. For the 2010 run onwards, the NaI detector was replaced with a new one composed of 4×4 BGO crystals, providing better energy and position resolution.

The CEX reaction can not only provide energy calibration at 55 MeV, close to the signal energy scale, but can do so in a position-dependent fashion by pointing

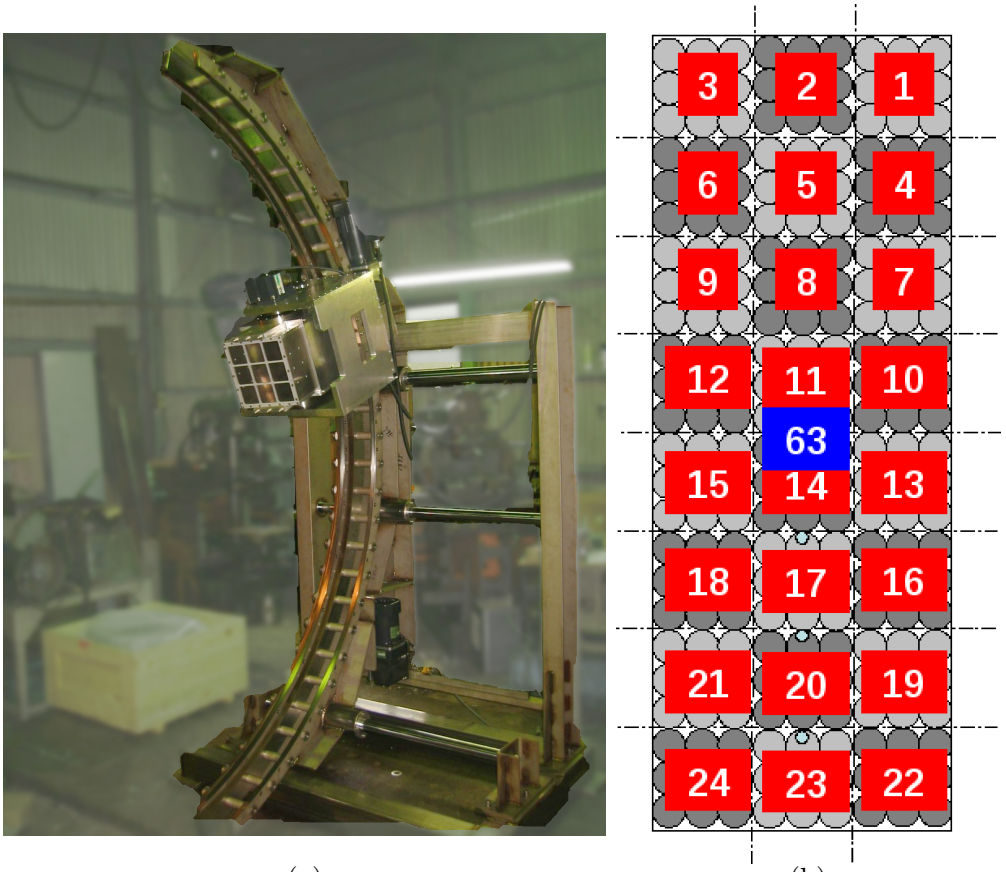

(a) (b)

Figure 3.21: (a) Moveable support for the CEX auxiliary detector. (b) Numbering of calorimeter software collimators (*patches*) used during CEX calibration.

the secondary detector at different regions of the calorimeter in order to study the LXe detector response uniformity. The calorimeter inner face is divided into 3×8 *patches* for this purpose, each composed by 3×3 PMTs, towards which the secondary detector is pointed. Events belonging to the appropriate patch are selected at the trigger level and the resulting mapping is used to provide a correction for non-uniformities in the calorimeter response along the (u,v) plane. The patch layout is summarized in Fig. 3.21.b.

This calibration can not be performed in presence of the COBRA magnetic field, requires a time consuming set up for the LH_2 target and deteriorates PMT gain at ~ 4 times the rate of regular physics run. For this reason it is only performed a few times per year during dedicated periods.

3.4.4 Reconstruction and Performance

The photon conversion point in LXe is reconstructed in three dimensions by fitting the observed light distribution on the PMTs to the expected distribution calculated from solid angles. The γ-ray direction is then obtained by combining this information with the reconstructed position of the positron vertex on the target. The position resolution can be evaluated using the CEX reaction in conjunction with lead collimators placed at known positions outside the cryostat on the target side. The average resolution is $\sigma_{u,v} \sim 5$ mm and $\sigma_w \sim 6$ mm.

The photon energy is reconstructed using the sum of the collected light weighted by photocathode coverage, and will be discussed in more detail in Chapter 7. The linearity of the relation between E_γ and detected scintillation photons is shown in Fig. 3.22. This method provides very good results for all events except for very shallow ones ($w < 2$ cm) which are very sensitive to the conversion point position relative to each PMT.

The resolution at the signal energy scale is extracted from CEX data after correcting for the different background conditions and unfolding the photon energy spread. Fig. 3.23 shows a fit of the 55 MeV peak from CEX data acquired at *patch 8* ($|u| <$ 9.3 cm, $18.6 < v < 37.2$ cm) for deep events ($w > 2$ cm). The response function is asymmetric due to interaction of γ-rays with the material in front of the active volume and shower leakage from the front face, resulting in a low energy tail; hence the quoted

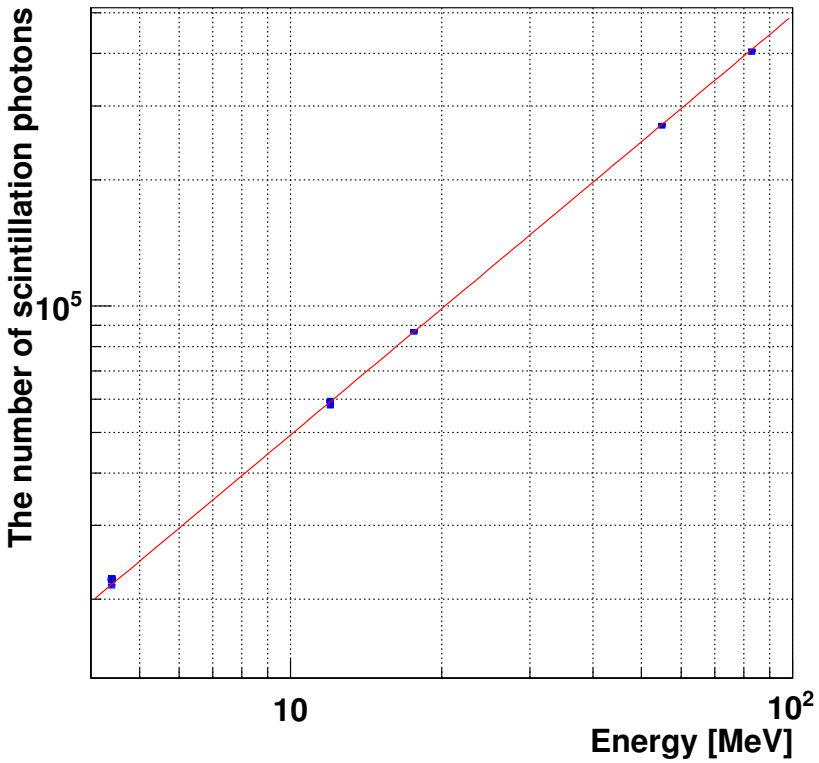

Figure 3.22: Number of detected scintillation photons as a function of calibration signal energy: 4.4, 11.6 and 17.6 MeV γ-rays are obtained from the CW calibration, while 55 and 83 MeV γ-rays are from the CEX calibration.

resolution is valid for the high-energy side. The average energy resolution over the full calorimeter surface is $\sigma_{E_\gamma} = 1.7\%$ ($w > 2$ cm) and 2.4% ($w < 2$ cm).

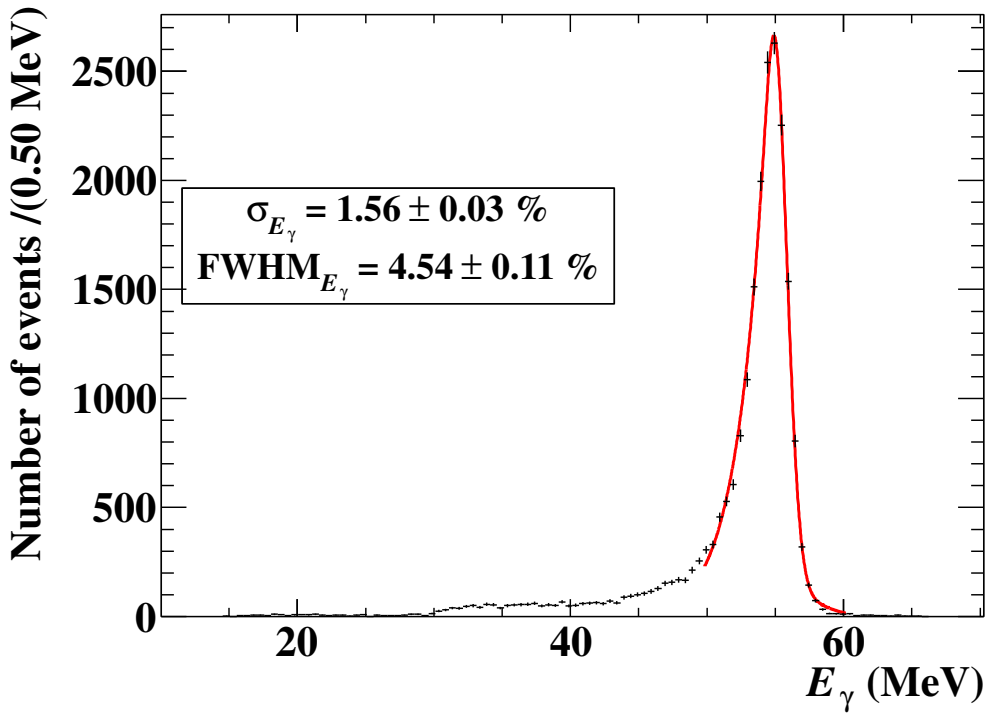

Figure 3.23: Energy response of the LXe detector to 55 MeV photons from CEX calibration. Only events at depth $w > 2$ cm and belonging to *patch 8* are used.

LXe timing resolution arises from the combination of different contributions: photoelectron statistics, electronics, uncertainties in time of flight determination and position reconstruction and a small correction from the muon decay vertex position resolution. The total timing resolution is $\sigma_t = 67$ ps.

3.5 Trigger and Acquisition

A search for rare events in a high background environment requires an efficient and quick event selection, which in turn requires high resolutions and fast front-end electronics and trigger.

3.5.1 Trigger System

Trigger latency requirements are limited by the digitizing electronics, as an excessively slow trigger might reach the digitizing electronics when portions of the waveform have already been overwritten. For this reason the trigger signal must reach the front-end boards within 450 ns from the event time. The trigger must also provide sufficient background rejection while maintaining a signal efficiency close to unity.

This is achieved at the hardware-wise by using a system of VME boards arranged in a pyramid structure. The signals are digitized by means of 100 MHz flash-ADCs and reconstruction of relevant observables is handled by Field-Programmable Gate Arrays (FPGA) incorporated in the trigger boards.

The first layer of VME boards (commonly called "Type 1") collect individual detector signals at a 100 MHz rate, while a second layer ("Type 2") combines information from Type 1 boards into estimates of the observables of interest. A scheme of the trigger hierarchy is shown in Fig. 3.24.

This solution is chosen not only for the ability to achieve the required speed and efficiencies, but also for ease of programming multiple trigger criteria for different calibrations and event types. The availability of cyclic RAM buffers allows the use of the trigger as a secondary digitizer, independent from the DAQ scheme.

The observable reconstructed at trigger level are the photon energy E_γ, the $e-\gamma$ relative direction and their relative timing. The latency requirements prevent use of the DC information, as drift times in the chamber can be as high as 200 ns. Hence it is not possible to reconstruct the positron momentum, although requiring a TC hit implies a request for $p_{e^+} > 45$ MeV/c.

The photon energy is obtained from the sum of PMT charges weighted with the QEs, gains and PMT coverages. A threshold of $E_\gamma > 45$ MeV is requested, guaranteeing an efficiency $\gtrsim 99.5\%$ for signal events while reducing the background rate by two orders of magnitude.

The photon direction is given by the (θ, ϕ) coordinate of the PMT with the largest signal, with the assumption that the γ-ray originates from the target center. The positron direction is derived from the (z, ϕ) coordinates of the TC hit under the same assumptions.

The relative $e-\gamma$ timing is assessed by allowing a 10 ns window for time coincidences. The timing offsets are corrected by using simultaneous γ-rays from CW Boron reactions (see Sect. 3.4.3).

The full trigger efficiency is $\epsilon \simeq 97\%$ for signal events and the trigger rate is on the order of ~ 10 Hz.

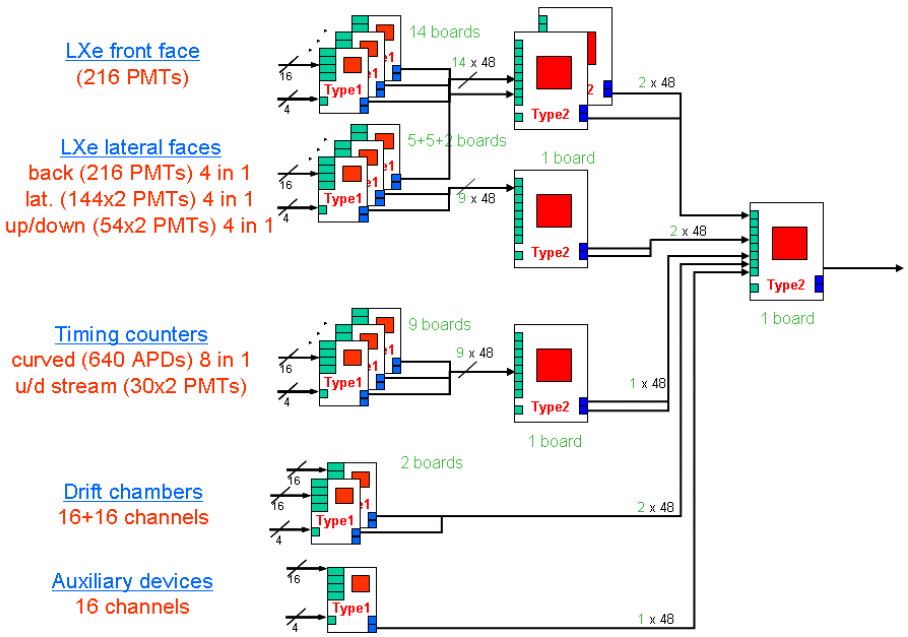

Figure 3.24: Schematic of the trigger system, composed of Type 1 (left) and Type 2 (right) boards, arranged in a pyramid scheme.

3.5.2 Front-end Electronics and DAQ

The data acquisition system (DAQ) for the MEG experiment requires a high precision and high rate of operation. For this reason each detector channel is digitized at high sampling frequency using a capacitor sampling chip designed at PSI, called the Domino Ring Sampler (DRS). An array of 1024 analog cells controlled by a circulating domino wave constantly samples the input signals at a frequency of 1.6 GHz (LXe and TC) and 0.8 GHz (DC) until the wave is stopped by a trigger signal. This sampling speed

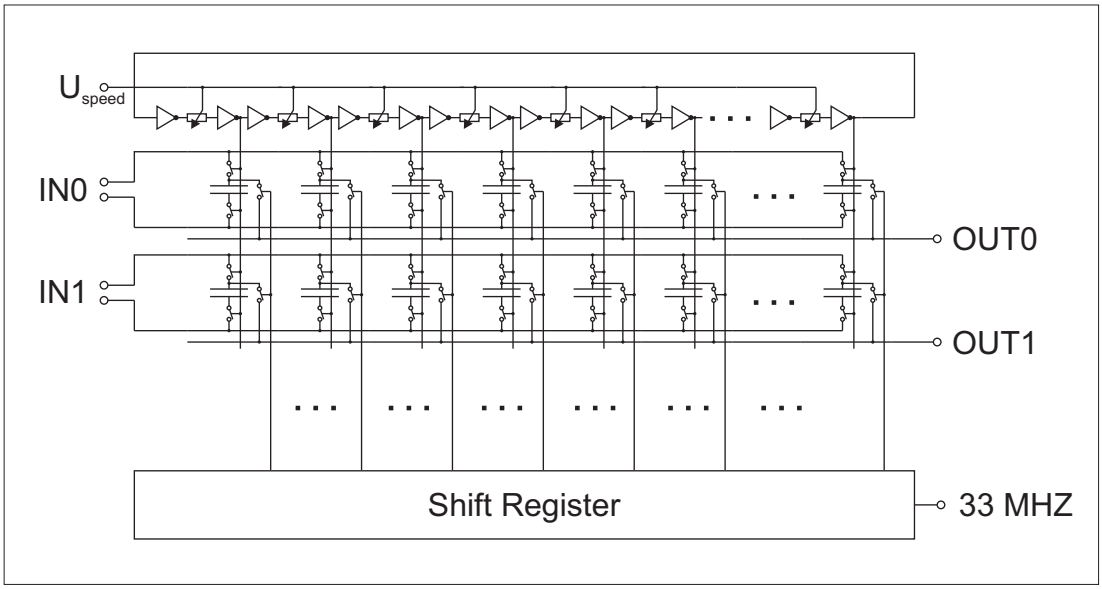

Figure 3.25: Simplified schematic of the DRS inverter chain.

is controlled with high precision by an external clock. The cell content is then read out through a shift register at 33 MHz. A schematic is shown in Fig. 3.25.

Each chip contains eight data channels, plus one additional timing channel sampling the external clock as to correct for possible jitter, achieving a timing precision of $\sim$ 50 ps. The chip is housed on a custom VME board and read out by a commercial 12 bit ADC and controlled by FPGAs, allowing for easy modification of the DAQ algorithms.

The crates containing the VME boards are read out by a cluster of nine dedicated PCs for online waveform processing. A tenth backend PC stores the collected data which is then copied to the PSI computing center for offline analysis.

4

2009-2011 Analysis

Events are characterized by five distinct observables $\tilde{\mathrm{x}} = \mathrm{E}_\gamma, \mathrm{E_e}, \mathrm{t}_{\mathrm{e}\gamma}, \theta_{\mathrm{e}\gamma}$ and $\phi_{\mathrm{e}\gamma}$. The analysis is done through a blind approach, where the region corresponding to $48 < \mathrm{E}_\gamma < 58\mathrm{MeV}$, $|\mathrm{t}_{\mathrm{e}\gamma}| < 1$ ns is hidden until the probability density functions (PDFs) used in the analysis are finalized. The blind region is chosen to fully contain signal events but still retain some background.

The best estimates for the number of signal, radiative and accidental events are computed simultaneously in the analysis region $48 < \mathrm{E}_\gamma < 58\mathrm{MeV}$, $50 < \mathrm{E_e} < 56\mathrm{MeV}$, $|\mathrm{t}_{\mathrm{e}\gamma}| < 1$ ns, $|\theta_{\mathrm{e}\gamma}| < 50$ mrad and $|\phi_{\mathrm{e}\gamma}| < 50$ mrad by maximizing the likelihood function

$$\begin{aligned}\mathcal{L}(N_{sig}, N_{RMD}, N_{acc}) &= \frac{e^{-N}}{N_{obs}!} e^{\left[-(N_{RMD}-\langle N_{RMD}\rangle)^2/2\sigma^2_{RMD}\right]} \\ &\times\ e^{\left[-(N_{acc}-\langle N_{acc}\rangle)^2/2\sigma^2_{acc}\right]} \\ &\times \prod_{i=1}^{N_{obs}} \left[N_{sig}S(\vec{x_i}) + N_{RMD}R(\vec{x_i}) + N_{acc}B(\vec{x_i})\right]\end{aligned}$$

where $\vec{x_i}$ are the observables for the i-th event, N_{sig}, N_{RMD} and N_{acc} are the number of signal, RMD and accidental events to estimate via the maximization and S, R and B the corresponding PDFs. $N = N_{sig} + N_{RMD} + N_{acc}$ while N_{obs} is the number of observed events in the analysis region.

Event values between brackets are estimates for the expected values in the blind region extrapolated from the so-called "sidebands", which are regions outside the blinding box. $\langle N_{RMD}\rangle$ is extracted from the off-energy region $48 < \mathrm{E}_\gamma$ and $\langle N_{acc}\rangle$ from the off-time regions $|\mathrm{t}_{\mathrm{e}\gamma}| > 1$ ns, each with their own uncertainty σ_{RMD} and σ_{acc}.

The PDFs for signal, radiative and accidental events are all extracted from data in the sidebands. Different resolutions and correlations between variables are accounted for on a per-event basis.

As a cross-check, the analysis is repeated independently either without event-by-event information, using stereo angle PDFs instead of two separate (θ, ϕ) angular PDFs, or with a Bayesian approach. Each method gives results consistent with the method described above.

The 90% C.L. upper limit is determined by a frequentistic approach with profile likelihood ratio ordering (2, 26, 27). Multiple sets of toy Monte Carlo are generated at different values of N_{sig}, treating N_{RMD} and N_{acc} as fixed nuisance parameters. The likelihood ratio

$$\lambda_p(N_{sig}) \;=\; \frac{\mathcal{L}(N_{sig}, \hat{\hat{N}}_{RMD}(N_{sig}), \hat{\hat{N}}_{acc}(N_{sig}))}{\mathcal{L}(\hat{N}_{sig}, \hat{N}_{RMD}, \hat{N}_{acc})} \tag{4.1}$$

is computed for each pseudo-experiment, where the hat and double hat denote the best estimates for likelihood maximization for floating and fixed N_{sig} respectively. If, after ordering the toy MC by their likelihood ratio, less than 90% of toy MC have a better likelihood than the real experiment, that value of N_{sig} belongs to the 90% C.L. region of the upper limit.

Normalization

The number of signal events is translated into an upper limit by using a normalization factor which is calculated in two independent ways: counting the number of Michel positrons selected with a prescaled dedicated trigger and by using the number of RMD events observed in the sidebands.

Sensitivity Evaluation

The sensitivity ($\mathcal{S}_{90}$) of the MEG experiment is estimated by running the likelihood analysis described above on an ensemble of toy experiments, generated under a null signal hypotesis with the values for $\langle N_{RMD} \rangle$ and $\langle N_{acc} \rangle$ estimated from the sidebands. The median of the 90% C.L. branching ratio upper limits is taken as the experiment sensitivity.

Results for 2009-2011 Data Set

The analysis was performed on three years of data (2009-2011), consisting in the first half the total MEG I data set. The profile likelihood ratios as a function of the branching ratio are shown in Fig. 4.1, while Fig. 4.2 shows the confidence intervals. The results are summarized in Tab. 4.1 for the 2009-2010 data set, the year 2011 alone and the total 2009-2011 data set.

Year	$\mathcal{B}_{\text{fit}} \times 10^{12}$	$\mathcal{B}_{90} \times 10^{12}$	$\mathcal{S}_{90} \times 10^{12}$
2009–2010	0.09	1.3	1.3
2011	−0.35	0.67	1.1
2009–2011	−0.06	0.57	0.77

Table 4.1: Best fit values for the likelihood function ($\mathcal{B}_{\text{fit}}$), branching ratios ($\mathcal{B}_{90}$) and sensitivities ($\mathcal{S}_{90}$). (28)

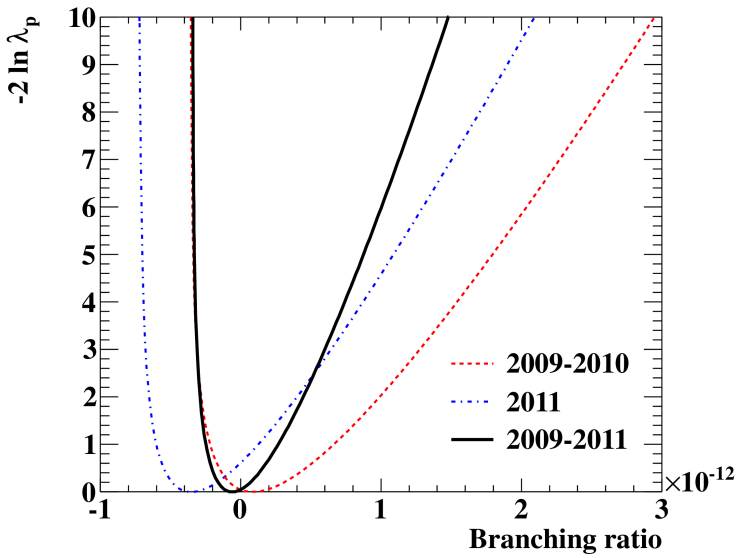

Figure 4.1: Profile likelihood ratios as a function of $\mathcal{B}(\mu \to e\gamma)$. As a reminder, these curves are not directly used to derive the upper limits, which are obtained in a full frequentist approach. (28)

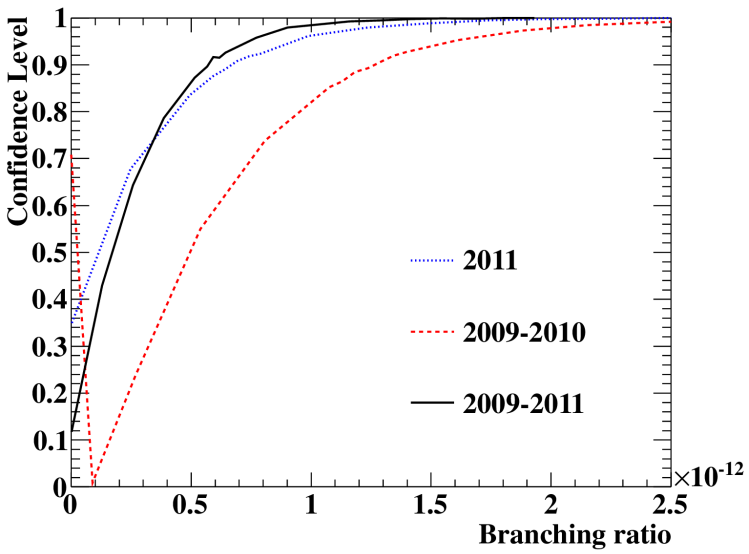

Figure 4.2: Confidence level scan for different values of $\mathcal{B}(\mu \to e\gamma)$ for the 2009-2010 combined data, the 2011 data, and the total combined 2011 data. (28)

In conclusion, the upper limit provided by the 2009-2011 MEG I data set is $\mathcal{B} < 5.7 \times 10^{-13}$ at 90% confidence level. This is the most stringent upper limit to date on the $\mu \to e\gamma$ branching ratio, with an improvement of about a factor of 20 with respect to the previous result by the MEGA collaboration. A full analysis on the complete 2009-2013 MEG I dataset is underway.

Part III

The MEG II Upgrade

5

The MEG Upgrade Plan

5.1 Motivations

The MEG I upper limit of 5.7×10^{-13} at 90% C.L. is the current best result for the measurement of the $\mu \to e\gamma$ decay branching ratio ($\mathcal{B}$). The inclusion of data from the years 2012 and 2013 will double the available statistics, for an expected single event sensitivity of $4 \div 5 \times 10^{-13}$.

The statistical significance of further data acquired in the same conditions is limited, since as previously discussed in Chapter 2, the background is dominated by accidental coincidences and thus the sensitivity does not scale linearly with the collected data. A further increase in sensitivity would require an improvement in the detector resolutions.

Nevertheless, while SUSY theories with cLFV modes have broad possible intervals for the value of the $\mathcal{B}(\mu \to e\gamma)$ (see Chapter 1), most of them predict a large value for $\mathcal{B} \gtrsim 10^{-13}$. In particular SUSY-GUT theories favor the $\mu \to e\gamma$ channel when compared to other sources of cLFV. It would be thus very interesting to push the sensitivity one order of magnitude further.

Next generation cLFV experiments are in the works such as Mu2e at Fermilab (21) (expected to start in 2020) and COMET at JPARC (29) (Phase-I expected 2016) to measure branching ratio of the $\mu \to e$ conversion, or the Mu3e experiment at PSI (30) searching for the $\mu 3e$ decay, as well as future high intensities B factories (31) for $\tau \to \mu\gamma$ search. The proposed plans for MEG II (32) aim to be competitive with these experiments by increasing sensitivity by a further order of magnitude in a short term and at a low cost.

5.1.1 Margins of Improvement

The comparison between foreseen and experimental resolutions in MEG I is summarized in Tab 5.1.

The photon detector and timing counter almost met the design requirement, but the resolutions of the positron spectrometer are substantially worse than the design values, which in turn impacts the e-γ timing measurements, as the measurement of $t_{e\gamma}$ uses the length of the positron track from target to TC, as measured by the DC tracker.

The tracker efficiency is badly affected by the positioning of front-end electronics and mechanical supports which intercept a large fraction of positrons in their path to the timing counter. Additionally, the thin segmented cathode foils used to determine the hit position along the Z-coordinate suffer from having low amplitude signals (only a few mV) and being thus vulnerable to noise. Their use in high radiation environments also leads to the formation of deposits which give rise to discharges. Overall this makes the tracker unfit for operating at the higher rates beam rates that could be a possibility for the upgrade.

As far as the LXe detector is concerned, it suffers from degraded energy reconstruction close to the inner face, which are subject to strong non-uniformities in response due to the PMT granularity.

Resolution	Foreseen	Obtained
σ_{E_γ} (%)	1.2	1.7
σ_{t_γ} (psec)	43	67
γ position (mm)	4(u,v),6(w)	5(u,v),6(w)
γ efficiency (%)	> 40	60
$\sigma_{E_{e^+}}$ (KeV)	200	380
e^+ angle (mrad)	$5(\phi_e)$,$5(\theta_e)$	$11(\phi_e)$,$9(\theta_e)$
σt_{e^+} (psec)	50	107
e^+ efficiency (%)	90	40
$\sigma t_{e\gamma}$ (ps)	65	120

Table 5.1: Foreseen and measured resolutions for the MEG detector.

5.2 Upgrade Overview

We plan a significant improvement of sensitivity, to the level of $\sim 5 \times 10^{-14}$, in a short span of time ($\approx 5 \div 6$ years for R&D and running), by increasing detector resolutions and efficiencies and allowing for an increased muon rate. In order to achieve this in a reasonable time and budget frame, existing assets will be recycled into the upgraded experiment whenever possible. A rough overview of the upgrade concept is sketched in Fig. 5.1.

5.2.1 Beamline and Magnet

The optimal signal/background ratio for MEG I is achieved at a stopping rate of $3 \times 10^7 \mu$/sec, which is ≈ 3 lower than the maximum achievable rate with the πE5 beam.

In the MEG II experiment we plan on using the full available beam intensity to achieve a stopping rate of $7 \times 10^7 \mu$/sec on a thinner, 140 μm target placed at an angle of 15° with respect to the beam axis. This configuration has been chosen as the optimal one via MC simulations. An alternate option, involving a thicker scintillating active target, is being explored to tag the muon decay vertex. (33)

The magnet system, in particular the superconducting COBRA magnet, will remain unchanged due to cost and construction time concerns. The positron tracking devices were designed with this constraint in mind.

5.2.2 Drift Chamber

The positron tracker was completely redesigned for improved performance and high rate of operation. It is a 10-layer cylindrical stereo wire drift chamber, of half length 970 mm, set with the axis aligned to the muon beam direction; a layout used by the KLOE (34) experiment. Each layer is set to alternating stereo angles to better reconstruct the z hit coordinate, with angles varying from 8° for the outer layers to 7° for the innermost ones. Individual cells, comprising eight field wires surrounding the anodic sense wire, have a size of approximately 7×7 mm^2, with variations caused by the stereo twist.

The tracking volume extends from a radius of 27.5 cm (outermost layer, measured at the chamber extremities) to ~ 17 cm, so that low energy positrons ($E_e < 45$ MeV)

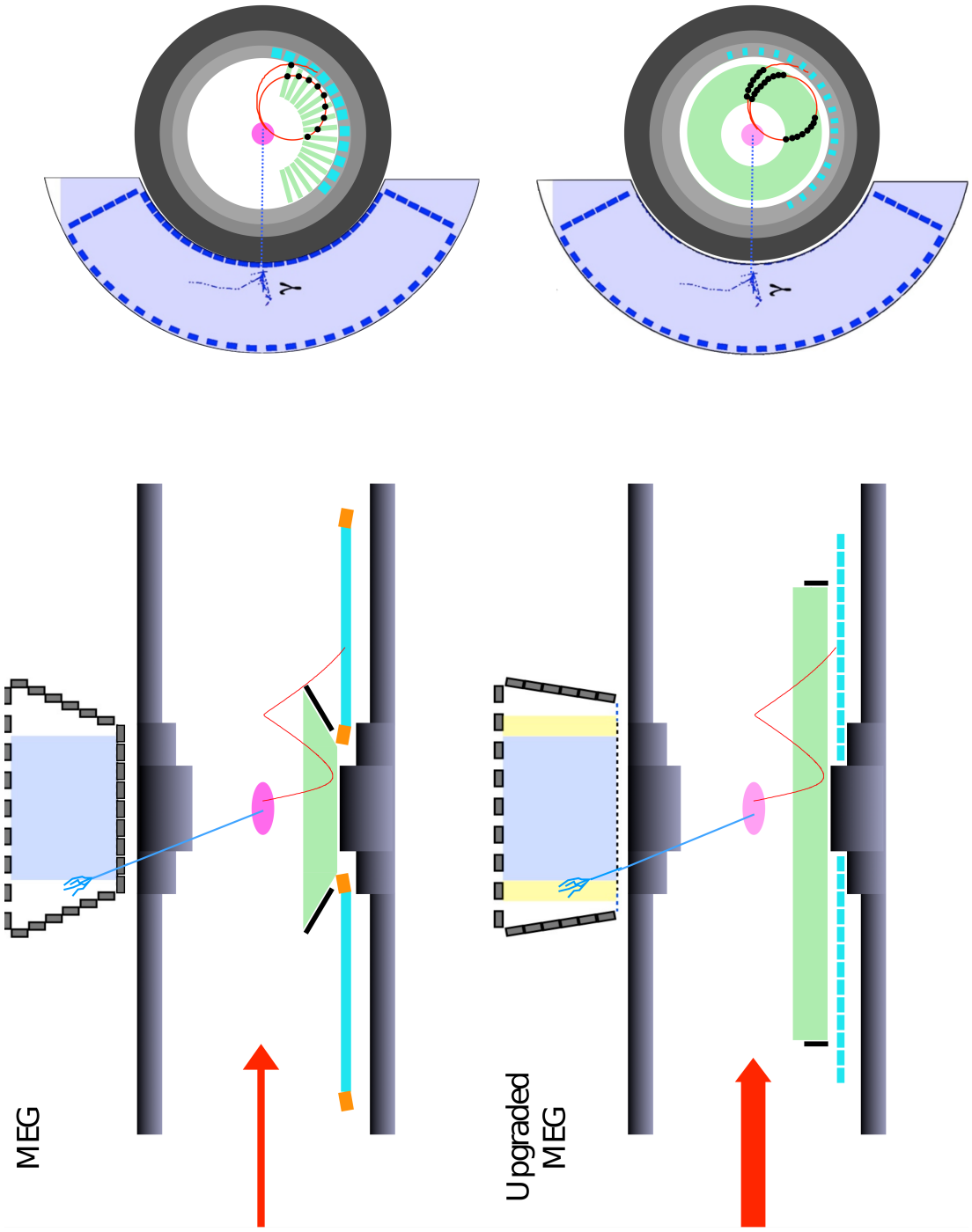

Figure 5.1: Overview of the MEG upgrade plans, comparing the MEG I detector to the one planned for MEG II.

are swept out by the magnetic field without crossing the sensitive volume. A sketch of the geometry can be seen in Fig. 5.2.

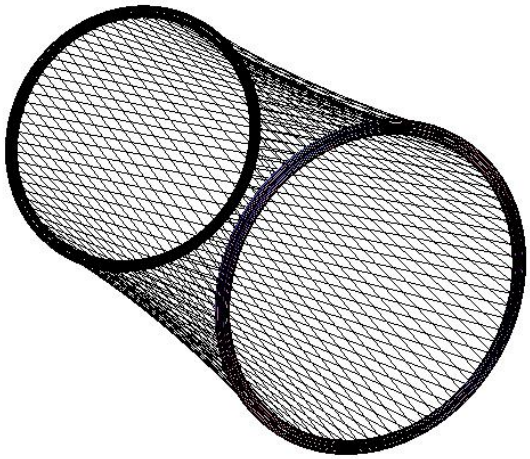

Figure 5.2: Sketch of the new MEG drift chamber geometry.

The choice of wires and materials for the chamber is dominated by the need to minimize multiple scattering. The anodes are 20 μm diameter tungsten wires, while the cathode wires are 50 μm aluminum. A thin 20 μm Kapton protective foil is used to separate the chamber volume from the central beam/target volume, which is filled with helium. The chamber itself is filled with a 85:15 He/iC_4H_{10} mixture, chosen once again for its low mass.

The chamber length allows for the chamber supports and readout electronics, which heavily contributed to multiple scattering in MEG I, to be placed outside the particle path. The total thickness crossed by a signal track in this configuration is $X_0 = 1.6 \times 10^{-3}$ for a single loop, as opposed to $X_0 = 2.0 \times 10^{-3}$ for the MEG I spectrometer.

The large chamber occupancy makes fast hit reconstruction a tricky proposal. The implementation of a double anode readout system, providing a coarse longitudinal resolution and a redundancy margin, can greatly symplify the reconstruction algorithm. The resolution achievable through double readout alone will be discussed in Section 6.3.

Expected Performance

The response for the drift chamber was studied by means of a full Monte Carlo simulation of the detector. A track produces ~ 60 cell hits on average, greatly improving track resolution. A value of 120 μm for single hit cell resolution was assumed in the simulation, resulting in an angular resolution of $\sigma_{\phi_e} \simeq \sigma_{\theta_e} \sim 5$ mrad and a momentum resolution $\sigma_p \sim 120$ KeV. The resolution of the reconstructed vertex position on target is $\sigma_y \sim 0.8$ mm and $\sigma_z \sim 1.2$ mm. Thanks to the positioning of readout electronics and mechanical supports out of the way of the positron path, the DC-TC matching efficiency is improved to be $> 80\%$.

5.2.3 Timing Counter

The timing counter for MEG I achieved the desired performances during beam tests, but ultimately performed less than satisfactorily in the experiment itself. The cause is to be found in the behavior of TC PMTs in the COBRA magnetic field. Magnetic fields affect PMTs by increasing the transit time spread and reducing gain. In addition, the TC design suffers from having a large track projection along z, further increasing the signal time spread.

The new pixelated timing counter for MEG II aims to fix these shortcomings by combining precise, magnetic-insensitive detectors with a high level of segmentation. It is composed of two semi-cylindrical modules, segmented as shown in Fig. 5.3. Each pixel is composed of a fast plastic scintillator read on each side by six 3×3 mm^2 silicon photomultipliers (SiPM) mounted on the plastic support of the module.

Thanks to their small size, each individual pixel can have good timing resolution as the contribution of scintillation light propagation time is small. The individual pixel time measurements can be combined by correcting for the particle transit time, achieving a time resolution $\sigma_t \lesssim 30$ ps. The information provided by multiple hits can be used during track reconstruction.

5.2.4 Xenon Calorimeter

The LXe calorimeter is a key component in the background suppression for the $\mu \to e\gamma$ search. The original detector performed admirably during the MEG I data taking, reaching the desired timing and position resolution performances. The most obvious

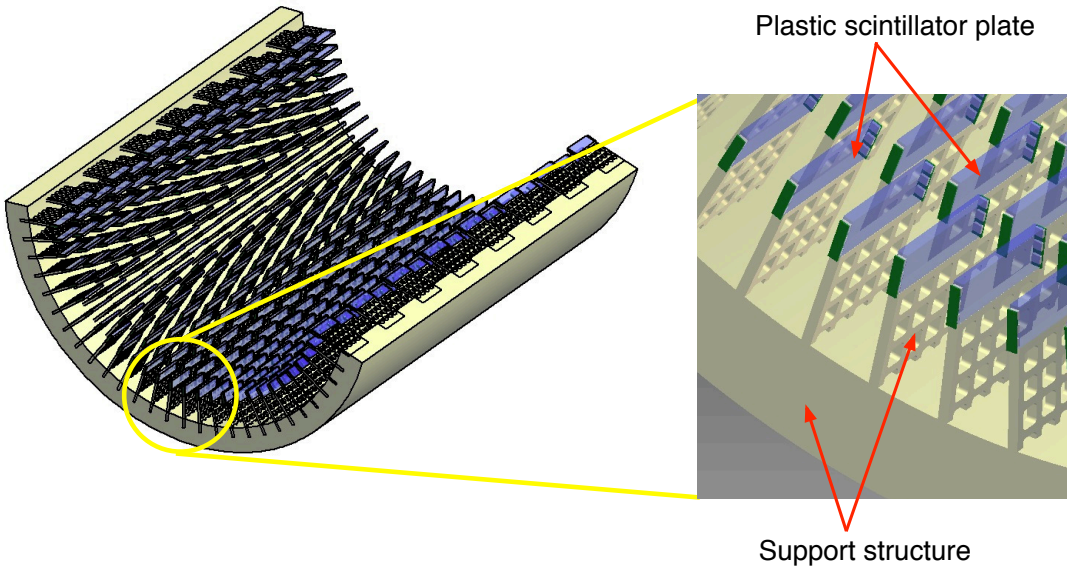

Figure 5.3: Schematic of the pixelated timing counter, showing the individual pixels.

margin of improvement lies in the energy reconstruction, which displays a worse resolution than foreseen with a strong position dependency.

The calorimeter inner face is covered by 216 PMTs positioned at 6.2 cm from each other. The sensitive surface of the photocathode, however, is round shaped with only a 4.6 cm diameter, leaving considerable dead space between each PMT where light is not collected. The result is a calorimeter response strongly dependent on position for shallow events, as shown in Fig. 5.4. This effect is partially corrected during offline analysis, but nevertheless negatively impacts the overall resolution.

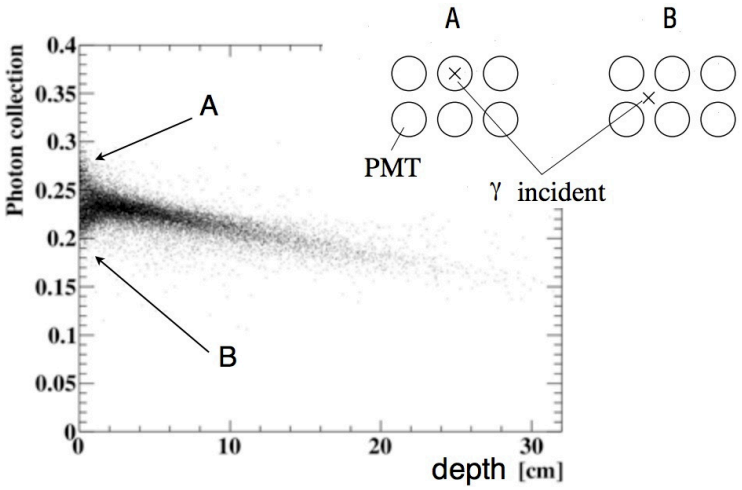

Figure 5.4: Efficiency of scintillation light collection as a function of depth of first interaction, as estimated from MC simulation.

The solution adopted for the upgraded detector is to replace the inner face PMTs with smaller, square shaped photosensors, allowing for simultaneously improved imaging power (better position reconstruction and pileup rejection) and more uniform light collection (superior energy resolution, with no position dependency). Fig. 5.5 shows a simulated example of the imaging power of the new layout.

The candidate for this replacement is a 12×12 mm^2 MPPC (Multi-Pixel Photon Counter), a type of SiPM produced by Hamamatsu Photonics. The choice of a thin sensor allows a further reduction of the material traversed by γ-rays crossing the inner face of the detector, thus improving the photon detection efficiency.

The same PMTs of MEG I will be used for the other faces of the calorimeter. However, as a result of MC studies, the layout of the upstream and downstram faces is

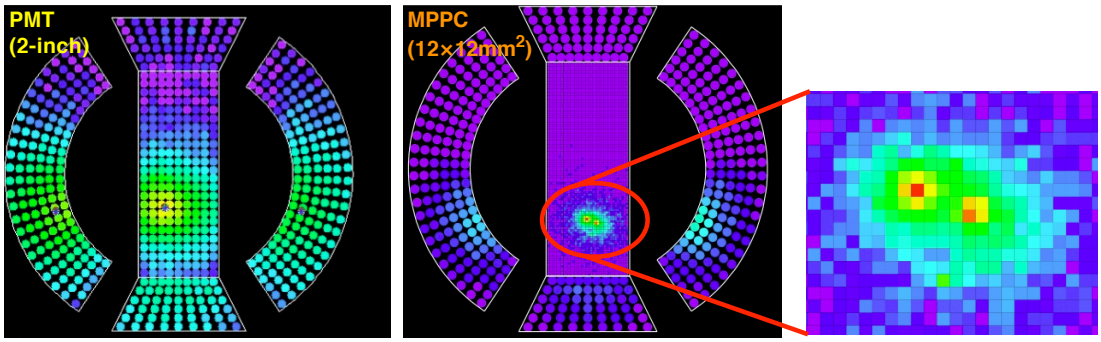

Figure 5.5: Example of light distribution seen in the MEG I calorimeter (left) and in the foreseen configuration for MEG II, using smaller, 12×12 mm^2 photosensors on the entrance face (right). Using a more granular detector, two local energy deposits are clearly separated, greatly reducing pileup.

to be modified as shown in Fig. 5.6, to better contain showers at the calorimeter edges. The entrance face will be extended along z, while the lateral face PMTs will be aligned on the same plane.

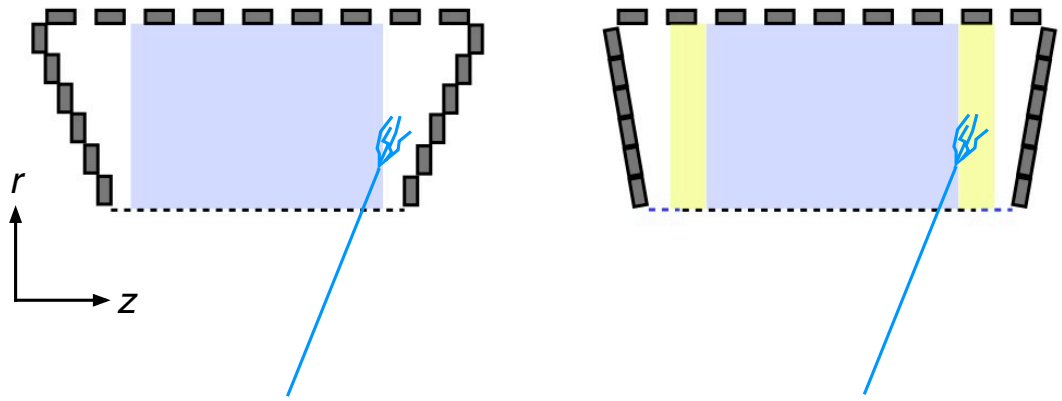

Figure 5.6: MEG I (left) and MEG II (right) PMT layouts viewed on the $r - z$ plane.

MPPC Development

VUV-sensitive MPPCs have been developed in close collaboration with Hamamatsu. The silicon detectors are protected by a thin quartz layer and the overall refraction index has been optimized for use in LXe at a wavelength of 178 nm. These new SiPMs are able to achieve a photodetection efficiency of $\sim 15\%$, similar to the average PMT

quantum efficiency of 16%. Each 12×12 mm^2 photodetector is composed of monolithic arrays of four 6×6 mm^2 MPPCs. The four segments are read in series, while the power supply is provided in parallel, producing a sharp waveform decay constant of ~ 30 ns, appropriate to our needs.

Performance

A full simulation based on Geant4 was developed to compare the resolutions of the present calorimeter to the planned upgraded configuration. The increased granularity of the inner face is expected to strongly improve the position resolution for shallow events, as shown in Fig. 5.7.

As far as the photon energy is concerned, resolutions are predicted to strongly improve, especially in the shallow ($w < 2$ cm) region, due to the better photon collection efficiency. Resolutions also improve in the deep region ($w > 2$ cm) thanks to the lower energy leakage from the new lateral face configuration. However, in MEG I, the measured energy resolution of the detector (1.7% for $w > 2$ cm) is worse than the MC prediction (1.2% for $w > 2$ cm). The reason could be either related to the behavior of PMTs or to the optical properties of the calorimeter.

This discrepancy is accounted for in the MEG II simulation by introducing an additional systematic smearing of the resolution. Fig. 5.8 shows the predicted energy responses in both the shallow and deep regions under three assumpions: (1) the ideal case where the fluctuation completely vanishes; (2) a conservative case where part of the fluctuation remains, corresponding to a 0.7% systematic smearing; and (3) the worst case scenario where the full fluctuation remains, which is equivalent to a 1.3% smearing.

In the conservative assumption, the energy resolution is expected to improve from $\sigma_{E_\gamma}(\%) = 2.4(shallow)/1.7(deep)$ to $\sigma_{E_\gamma}(\%) = 1.1(shallow)/1.0(deep)$. However, were the calorimeter to inherit the full fluctuation, the final resolution could end being worse, up to $\sigma_{E_\gamma} \sim 1.4\%$.

In Chapter 7 we will focus on understanding the origin of the differences and trying to develop a better reconstruction technique.

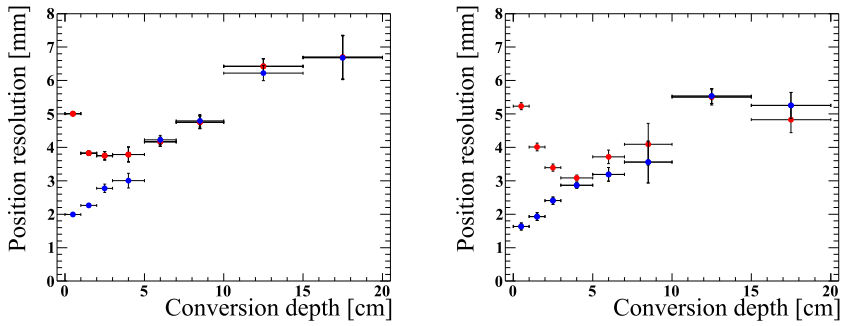

(a) (b)

Figure 5.7: Position resolutions along u (a) and v (b) as a function of conversion depth. The MEG I resolutions are shown in red, while the upgraded resolutions are shown in blue.

5.2.5 Trigger and DAQ

Two main improvements are required from the aquisition system in order to handle the requirements of MEG II: an increase in channels and an increase in bandwidth to implement cluster timing algorithms. The additional channels are required because of the higher number of individual outputs in the upgraded detectors and could be managed at a moderate cost. However, the MEG I frontend cannot handle the upgraded bandwidth requirements.

A new design for a DAQ board (WaveDREAM) has been studied, combining DRS digitization and low level trigger in a compact system, a scheme of which can be seen in Fig. 5.9. The new frontend has been designed to allow for fast digitization at 2 GHz using the DRS chip, a bandwidth suitable for a cluster timing algorithm.

Each DRS channel is also sampled at 100 MHz by ADCs to provide the same functionality as Type 1 trigger boards. The outputs are passed to dedicated trigger concentrator boards, which are used to interface to the higher level boards in a three level pyramid structure.

This compact, space saving design is to be housed in a dedicated custom crate, for reduced costs compared to the MEG I commercial VME boards.

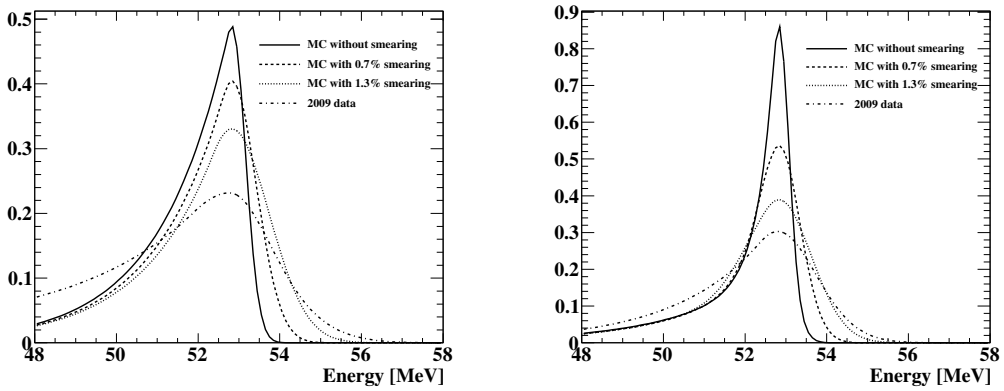

($w < 2$ cm) ($w > 2$ cm)

Figure 5.8: Simulated energy responses of the LXe detector under different assumptions for additional fluctuations, compared to MEG I data.

5.3 Final Sensitivity and Time Schedule

The achievable sensitivity for MEG II was evaluated using a *toy MC* ensemble, generated assuming zero signal events. The average number of accidental and radiative events was extrapolated from the MEG I values, corrected for the new detector performances (Tab. 5.2). The number of background events in each simulation was then left to fluctuate according to Poissonian statistics.

All simulations are fit with the likelihood analysis procedure used in MEG analysis (Chapter 4), extracting an upper limit for $\mathcal{B}(\mu \to e\gamma)$ at 90% CL. The median of the upper limit across all toy MC is taken as the sensitivity.

Fig. 5.10 shows the resulting sensitivity as a function of DAQ time. Assuming a muon rate on target of 7×10^7 μ/sec and ~ 200 DAQ days per year, a sensitivity of 5×10^{-14} is reached after ~ 80 weeks, or ≈ 3 years of data taking.

Construction of the new detectors is underway, to be completed in the middle of 2015. An engineering run is forseen at the end of 2015, followed by three full years of data taking in 2016-2018. The time schedule of the MEG upgrade is summarized in Chart 1.

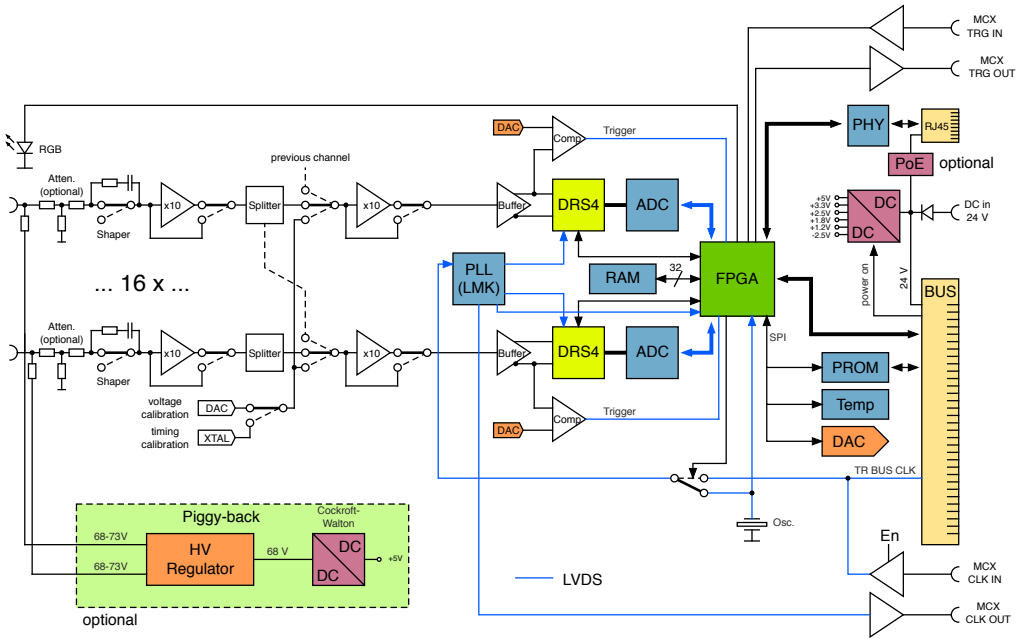

Figure 5.9: Simplified schematic of the WaveDREAM board.

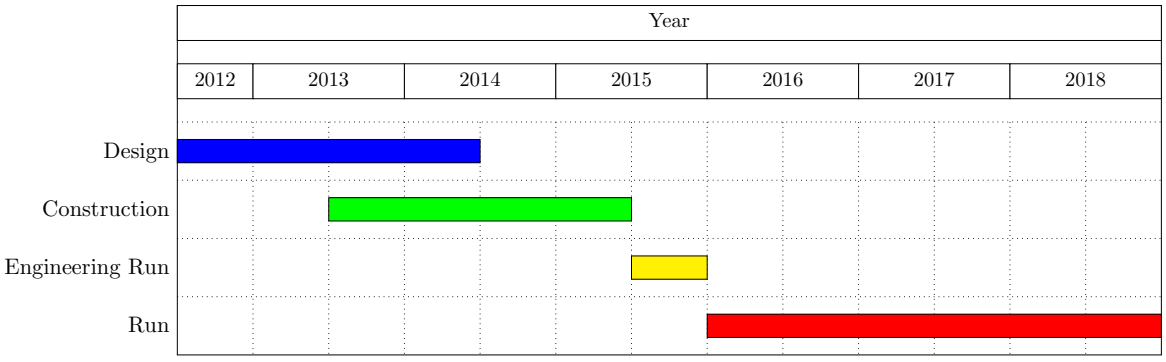

Chart 1: MEG Upgrade Time Schedule

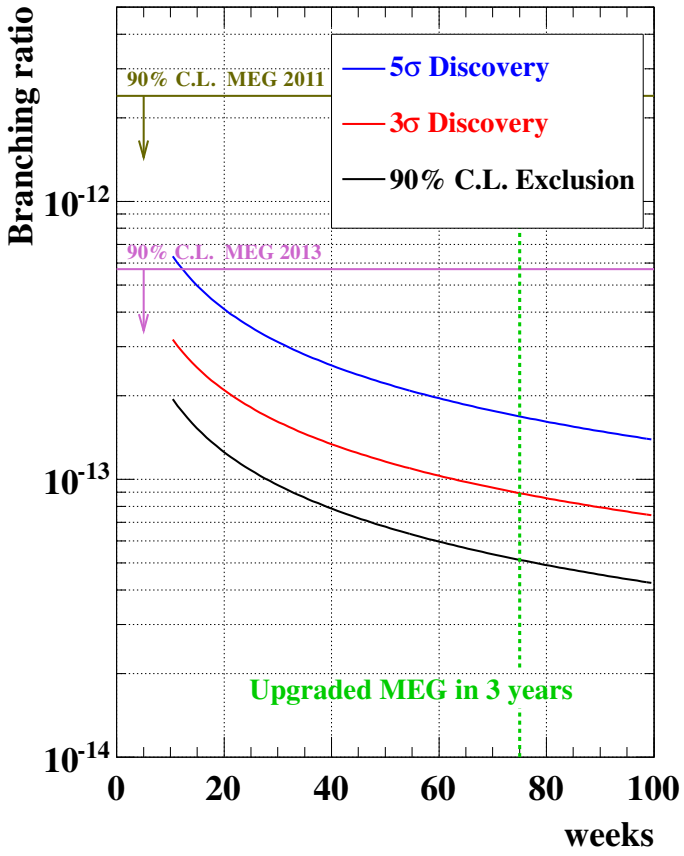

Figure 5.10: Projected sensitivity for MEG II as a function of DAQ time.

Resolutions	Present MEG	Upgrade
e^+ energy (keV)	306 (core)	130
e^+ θ (mrad)	9.4	5.3
e^+ ϕ (mrad)	8.7	3.7
e^+ vertex (mm) Z/Y(core)	2.4 / 1.2	1.6 / 0.7
γ energy (%) (w <2 cm)/(w >2 cm)	2.4 / 1.7	1.1 / 1.0
γ position (mm) $u/v/w$	5 / 5 / 6	2.6 / 2.2 / 5
γ-e^+ timing (ps)	122	84
Efficiencies (%)		
trigger	$\approx$ 99	$\approx$ 99
γ	63	69
e^+	40	88

Table 5.2: Comparison of resolutions and efficiencies for MEG I and MEG II.

6

Drift Chamber R&D

This chapter will describe the testing of drift chamber prototypes that successfully proved the feasibility and performance of the MEG II upgraded positron tracker, with an emphasis on the ones the author directly participated in.

6.1 Aging Tests

In the MEG II drift chamber the innermost wires of the chamber are subject to the highest event rate, ≈ 1 MHz for a stopping rate of $7 \times 10^7 \mu$/s. The side of each cell is 7 mm, so that the maximum drift time is ≈ 150 ns, corresponding to a $\approx 15\%$ occupancy for the innermost wire.

In the operating conditions above discussed, the total charge collected by the innermost cells during the acquisition time of the upgraded MEG experiment is evaluated to be quite high: $\simeq 0.4$ C/cm for a gain of $\approx 1 \times 10^5$. This large amount of collected charge makes a DC aging study essential.

To this purpose a DC prototype of 20 cm length was prepared using gold-plated tungsten wires, implementing a single 7×7 mm^2 cell surrounded by field shaping wires that mimic the presence of all other cells.

The prototype (shown in Fig. 6.1) was placed in a 3500 cc stainless-steel chamber equipped with thin (150 μm) mylar windows in order to let the ionizing radiation through. The whole setup is placed inside a Pb/Al box for radiation safety. A gas system (see Fig. 6.2) was assembled to provide the required gas mixture. The preliminary tests were performed before optimization of the gas composition, using a 90:10

He:iC_4H_{10} mixture flushed at 50 cc/min (equivalent to a full chamber volume per hour). Later tests were performed with the final 85:15 mixture, confirming the results here described.

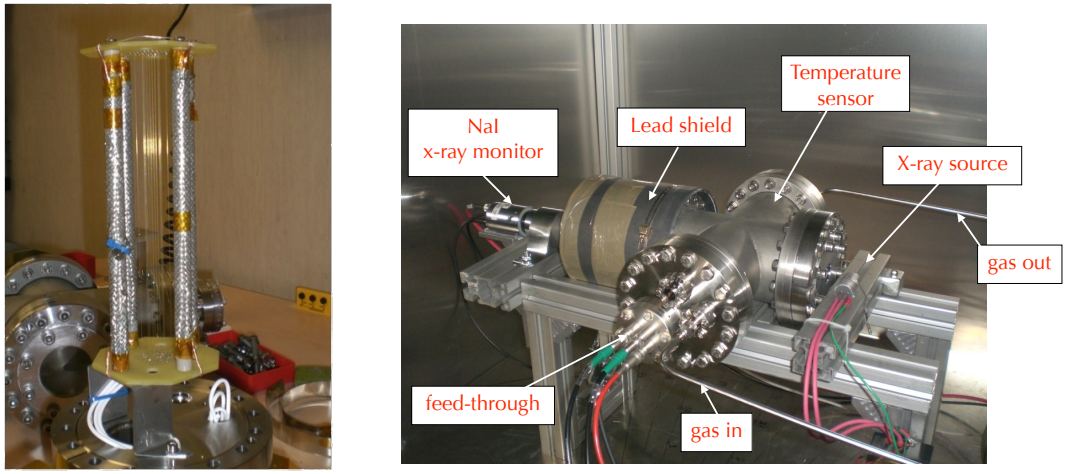

(a) (b)

Figure 6.1: Picture of the aging prototype (a) and of the measurement setup (b).

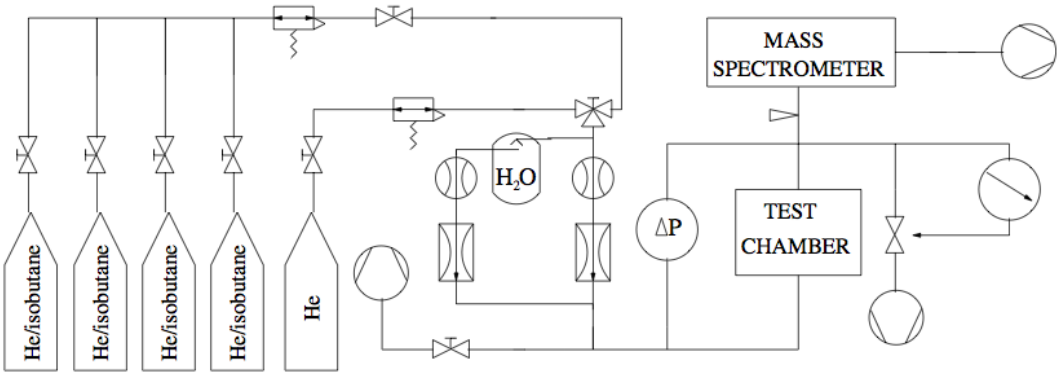

Figure 6.2: Gas circuit layout.

An X-ray gun, able to provide $> 10^{11}$ X-rays/sec/sterad, was placed in front of the mylar window in order to provide the aging effect, while a NaI detector was positioned with a lead collimator in front of the opposite window, to monitor the source's stability.

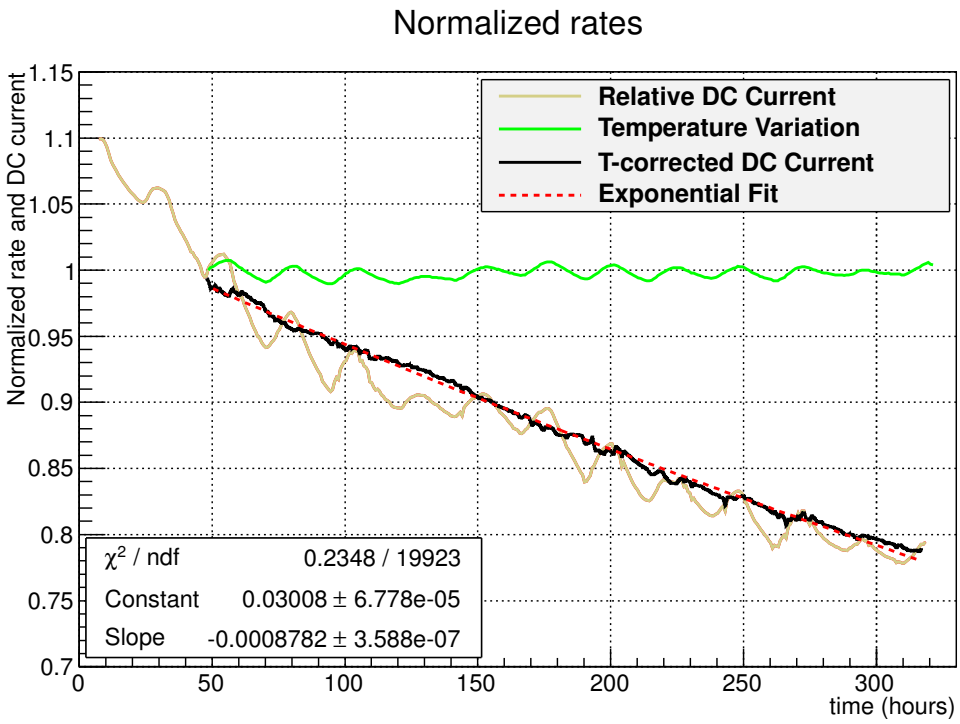

Figure 6.3: Results of the aging tests for the DC prototype, displaying the current decrease as a function of time after correcting

A ^{241}Am source placed inside the chamber was used for calibration.

The current is measured in a shifted potential configuration, where negative HV is applied to the field wires while the signal wire is grounded and read through a picoammeter.

The test was conducted at a DC current of 120 nA/cm, 20 times the maximum current foreseen in normal experimental conditions. Over the span of 10 days, a charge equivalent to $\approx$ 200 days (one running year) of normal operation is collected. The applied HV was -1250 V, corresponding to a gain of $\approx 10^5$.

Daily temperature variations affect the gas density in the chamber and make the wire currents oscillate over a 24 hour period. After correcting for this contribution, the current decrease (shown in Fig. 6.3) depends entirely on aging and can be fit to an exponential curve, giving $\tau \simeq 950$ days, *i.e.* a gain decrease of $\approx 0.11\%$ per day for the innermost wires, sufficiently low to be corrected by slightly rising the supply voltage

once per year. Further effects of aging from additional materials and components used in the chamber were also thoroughly investigated.

6.2 Single Hit Resolution

The single hit resolution of the detector was studied on a smaller sized (20 cm) three cell prototype using a cosmic ray telescope built in Pisa as a test facility.

The telescope, shown in Fig. 6.4, uses an assembly of four double-side silicon layers of SVT, the former vertex detector of the BaBar experiment (35), housed in aluminum boxes above and below the test detector (two layers in each box). The telescope array provides a hit resolution of 20 μm (transverse) and 40 μm (longitudinal), ideal for testing prototypes.

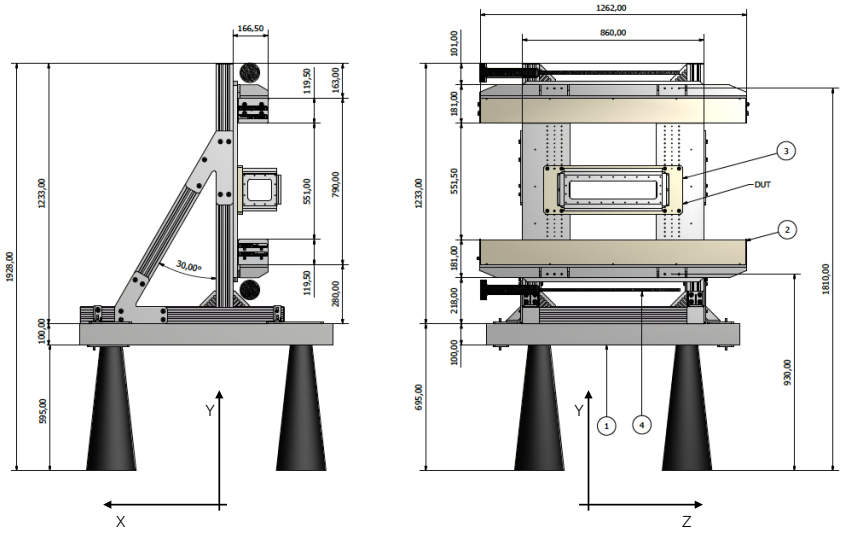

Figure 6.4: Technical design of the cosmic ray telescope for prototype testing.

Using this setup with the addition of a fast scintillator bar for timing purposes, the single hit resolution was measured by comparing the cell impact parameter, obtained from the drift time of the first ionization cluster, to the "true" impact parameter obtained with the telescope (see Fig. 6.5). The resolution was found to be $\sigma_{1hit} \lesssim$ 120 μm for all cells.

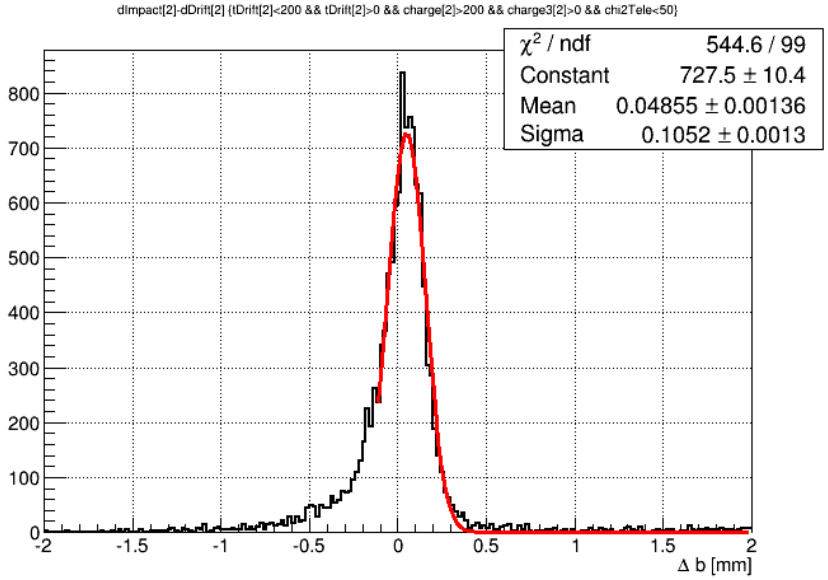

Figure 6.5: Single hit resolution of the prototype measured with the cosmic ray telescope.

It is to be noted that while the use of a low Z gas mixture in the drift chamber is essential for minimizing the effects of multiple scattering, the average number of ionization clusters produced by charged particles in such a mixture is quite low. This in turn increases the bias in the measurement of the distance of closest approach of a particle to the wire.

Single hit resolution could be further improved by using the information from all ionization clusters. Since the temporal separation between signals from different ionization clusters is of the order of a few nanoseconds, very fast electronics are needed, with a bandwidth on the GHz scale. Studies to verify the feasibility of such a technique are underway.

6.3 The Long Prototype

The construction of a 180 cm long drift chamber such as the one proposed for MEG II is a complex undertaking whose feasibility needs to be confirmed in practice.

To begin with, tensing micrometric wires of such lenght is a non-trivial process from a mechanical standpoint. Additionally, because of the stereo angle built into the wire structure, the electric field and hence the signal gain is position-dependent, increasing the complexity of the measurements. Furthermore, it is important to measure the speed of signal transmission on the wires, as it is directly impacts the achievable position resolution along the wire length.

In order to study all of the above, we devised the first full-length, single cell prototype of the MEG II chamber. This prototype is 1795 mm long and consists of a single cell measuring 7×7 mm^2 at each end, twisted by 60° along its axis to emulate the final detector's stereo angle.

The wires used in construction were chosen based on availability at the time and are respectively 80 μm diameter silver-coated aluminum for the cathodes and 20 μm diameter gold-coated tungsten [1] for the anode (sense) wire.

The cell is constructed by manually stringing and soldering the chosen wires through the holes of two printed circuit boards mounted on specially-designed aluminum supports which were bolted to an aluminum profile bar. The wiring was performed on a vertical position with the wires tensed using lead weights of 23 g and 30 g for anode and cathode, respectively. Four additional 80 μm field wires surround the cell and are set to a separate high voltage to mimic the presence of the other cells.

To avoid misalignments of the wire plates and subsequent distorsions of the cell shape, the positions of the aluminum supports was checked repeatedly during construction using a coordinate measuring machine. The total misaligment is measured to be under 40 μm.

Because of the twisted nature of the cell the distance of cathode wires to the anode depends on the longitudinal position, altering the cell width as follows:

$$\mathrm{d}(z) = \mathrm{d}_{\mathrm{cell}} \cos\alpha \sqrt{1 + \frac{z^2}{l^2} \tan^2\alpha} \tag{6.1}$$

[1] Measured resistivity is $171.1\Omega/m$.

where z is measured from the center of the prototype, $d_{cell} = 7$ mm is the cell width at either end of the prototype ($z = \pm l = \pm 897.5$ mm) and $2\alpha = 60°$ is the chamber twist angle. The cell section is thus 25% smaller at the chamber center.

6.3.1 Prototype Housing

To house the prototype we constructed a chamber using a 2 m long, 18 cm diameter plexiglas tube which was fitted with flanges of the same material at both ends to seal it hermetically. Plexiglas is light, cheap, easy to cut and work; the single pieces can be fused together during construction with the application of a solvent such as Dichloromethane (CH_2Cl_2), making for an airtight chamber.

In order to guarantee a stable operation, the field at the chamber walls must be well-defined. For this reason, a Faraday cage was build by sewing a cylinder-shaped aluminum net and inserting it in the tube. The net is set to a common ground with the rest of the supporting structure.

The flanges were closed with custom-built caps equipped with feedthroughs for high-voltage, low-voltage, and signal cables. The overall volume of the chamber is approximately 48 l.

6.3.2 Readout

In order to minimize noise pickup prior to amplification, the frontend preamplifier boards are soldered directly inside the chamber to both ends of the anode wire.

The preamplifying system is the test prototype for the final frontend electronics and is composed of a custom two stage cascading setup of AD8099 and THS4509 operational amplifiers. The models provided during construction provided a gain factor of $g_{FE}. \approx 7$; however, impedence studies undertaken in conjunction with the protoype construction improved the overall impedence matching and altered the frontend gain, enhancing it to $g_{FE} = 23$.

Each preamplifier board has differential output, which is then read through the four channels of a DRS4 evaluation board (36). The readout is thus hybrid, with each channel terminated at 50 Ω and the signal differentiation done successively at software level.

The power for the preamplifier is supplied by two low voltage modules in series with a common ground, with an output of ±3 V. A filter box (Fig. 6.7) placed close to the

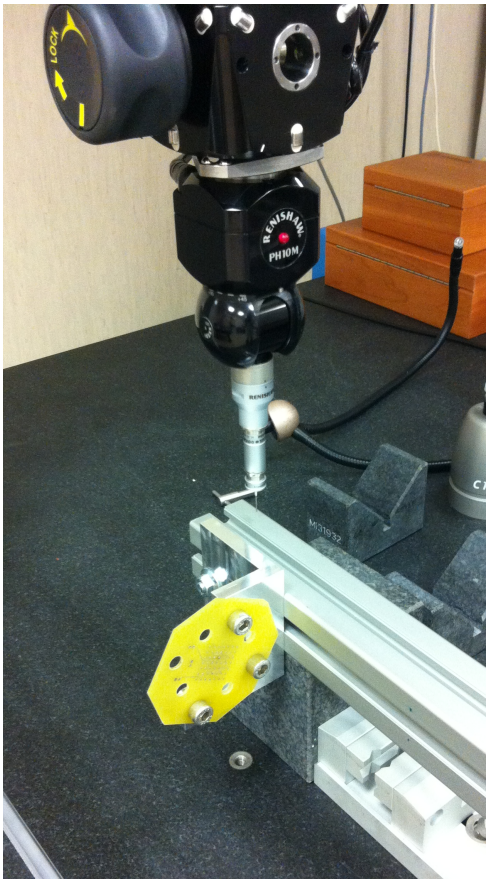

(c) *Aluminum support under the measuring machine.*

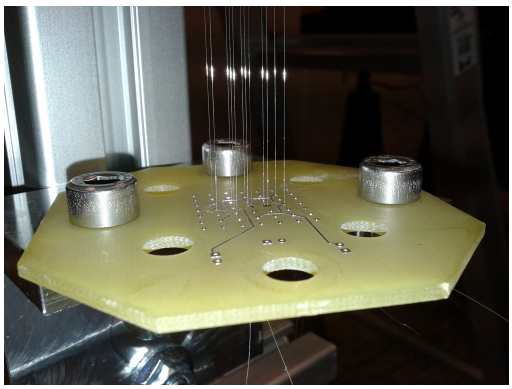

(a) *Detail of the printed circuit board with soldered wires.*

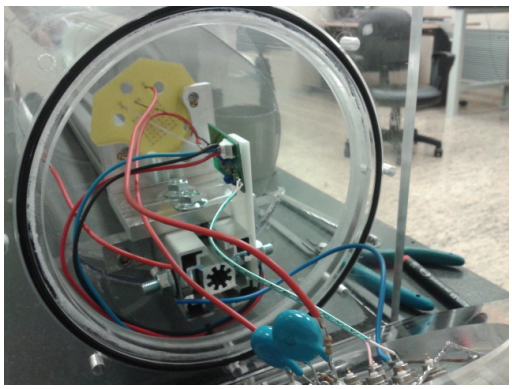

(b) *Detail of the endcap with HV connections.*

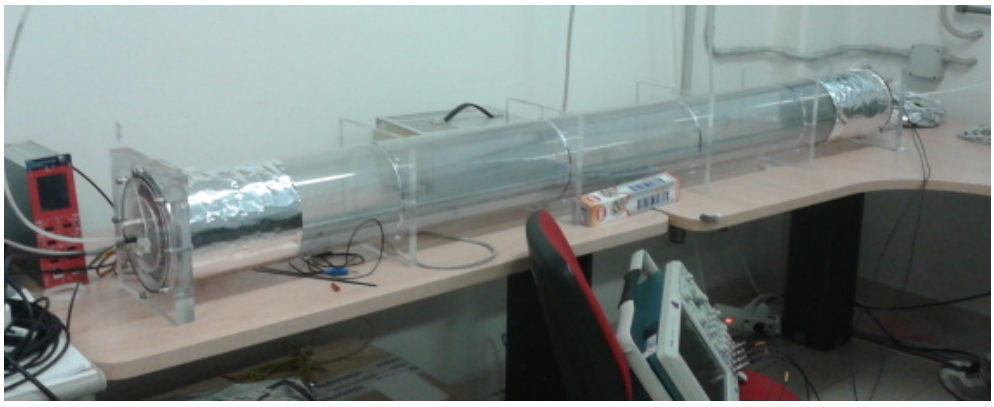

(d) *The long prototype.*

Figure 6.6: Assembly of the long protype.

electronics reduces pickup noise on the power line by a factor of ≈ 5 in the 1 kHz to 1 MHz range.

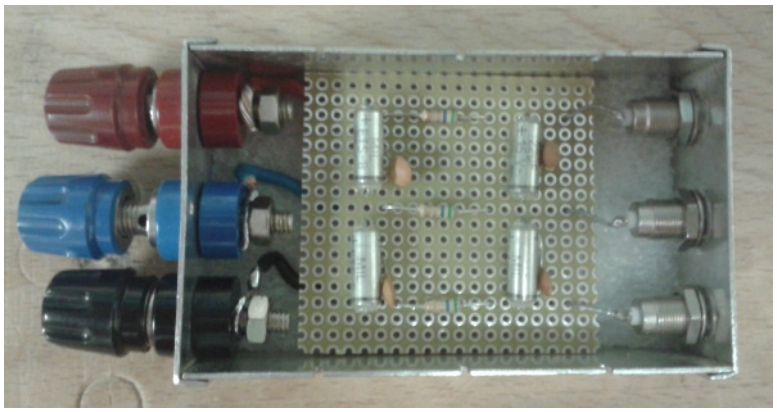

Figure 6.7: Low voltage line filter box.

6.3.3 Preliminary Setup and Trigger

The chamber was evacuated at $\approx 10^{-3}$ bar and then flushed with an 85:15 He/iC_4H_{10} mixture at a flow rate of 20 cc/min. The wire HV was set to 1530 V (anode) and 382 V (field) respectively.

The signal was provided by a ^{106}Ru source mounted on a C-shaped plexiglas support, with a plastic scintillator equipped with a 2×2 cm^2 PMT at the other end providing the trigger. The source was equipped with a 3 mm lead collimator to restrict the β trajectories to a narrow beam crossing the prototype cell. A 500 μm copper foil in front of the scintillator to stopped low energy β from the source, narrowing the signal energy band to the 2-3 MeV region.

6.3.4 Acquisition and Results

The source support was placed at different positions on the prototype housing for data acquisition, using a reference frame drawn on the plexiglas cylinder with the cell's narrowest point, i.e. the midpoint of the chamber, centered at $z' = 103$ cm. The uncertainty on the positioning is ± 1 cm.

Signal differentiation between the double readouts, along with baseline subtraction, was performed during preliminary analysis. A sample resulting waveform is shown in Fig. 6.8.

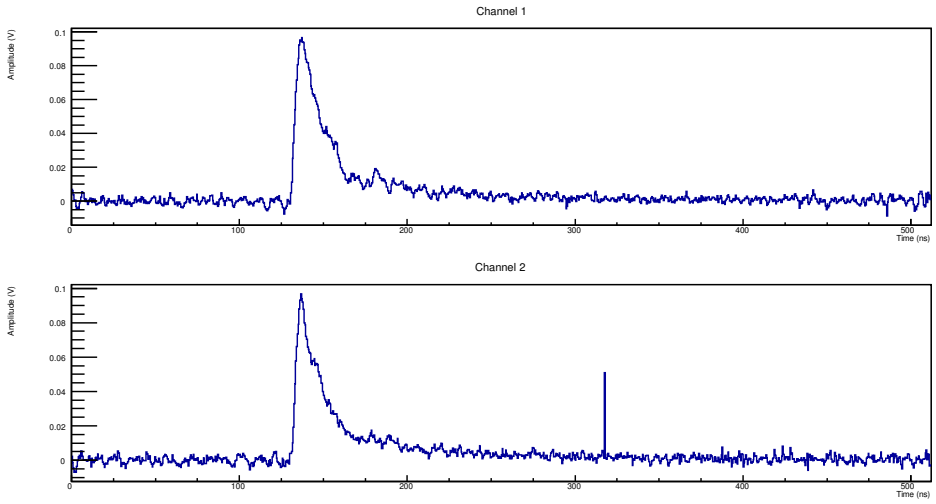

Figure 6.8: Sample waveform from β signal traversing the prototype chamber .

Timing

The time $T_{1,2}$ of each signal can obtained by fitting each waveform to its rising edge, while the signal charge $Q_{1,2}$ is obtained by integrating the waveform in a 100 ns window starting from it.

The time difference of the two signals depends linearly from the signal propagation speed along the wire:

$$\Delta T = \frac{v}{2} \cdot \Delta z \tag{6.2}$$

with $\Delta T = T_1 - T_2$ and Δz is the distance from the chamber center.

This propagation speed can be measured by fitting the position-dependent time difference distributions, as in Fig. 6.9. The resulting measured signal speed along the wire is $v_{sig} = 29.0 \pm 1.7$ cm/ns.

In addition, this shows the feasibility of using the time difference between signals to determine the event position along the wire with a precision of the order of ≈ 10 cm, allowing for simplified track reconstruction in the final detector.

Charge Asymmetry

An independent estimate of longitudinal position can be achieved by studying the collected charge at each end of the anode wire. The average value of the charge asymmetry, $\frac{Q_1 - Q_2}{Q_1 + Q_2}$, is plotted in Fig. 6.10 as a function of position, showing once again an

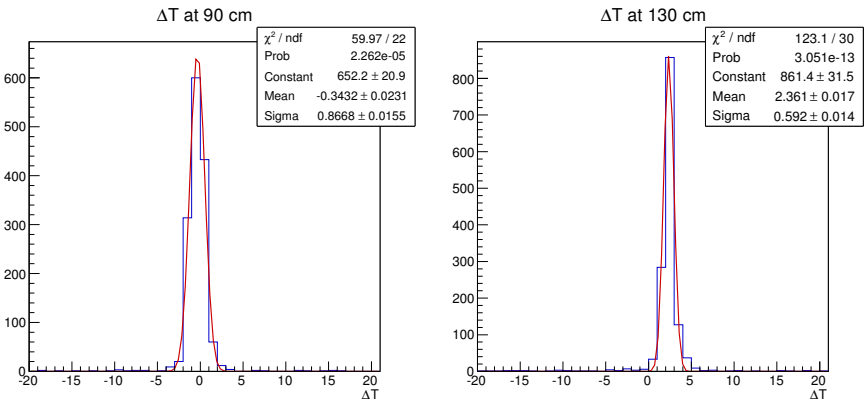

(a) *A sample of time difference gaussian distribution fits.*

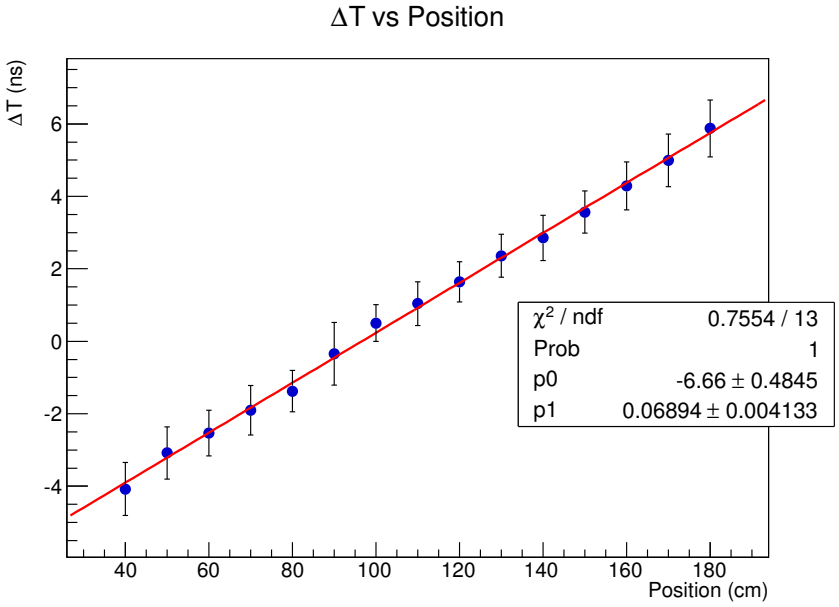

(b) *Time difference as a function of position.*

Figure 6.9: Signal speed and position measurement through time difference.

achievable precision of ≈ 10 cm on longitudinal position for a single hit through charge measurements alone.

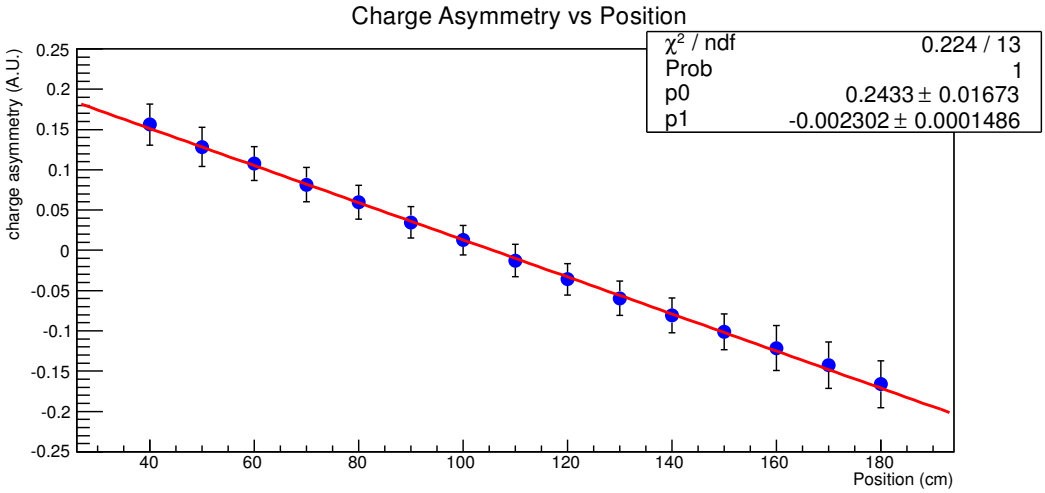

Figure 6.10: Charge asymmetry as a function of position.

The combined contribution of charge and time difference can thus provide a promising starting point for a reconstruction algorithm. A more precise measurement of the achievable single hit resolution along z will be performed on the full detector with the final wires and cell configuration by exploiting the stereo geometry of the chamber.

Gain Variation

The total collected charge on the sense wire depends linearly on the chamber gain g and the average length of the ionizing particle's path through the drift cell:

$$Q(z) \sim \langle d(z) \rangle \; g(z) \tag{6.3}$$

We can then evaluate the gain for the single twisted cell configuration by first fitting the total charge $Q = Q_1 + Q_2$ with an empyrical function (Fig. 6.11) and then correcting the mean value by a factor based on cell size which can be extracted from Eq. 6.1:

$$S = \sqrt{1 + \frac{z^2}{l^2} \tan^2 \alpha} \tag{6.4}$$

where z is, as previously mentioned, in the cell reference frame. This correction accounts for the smaller number of primary electrons resulting from the reduced cell size in the chamber center.

The chamber gain, estimated as the corrected charge normalized to the central value, is shown in Fig. 6.12 as a function of position. The change in cell size having been taken into account, this variation in gain is entirely dependent on the changes in electrical field and consists in a $\sim 40\%$ drop at the chamber ends, to be compared to a value of $\sim 20\%$ predicted by Garfield simulations.

This suggests either some systematic effect which needs to be better understood, such as a shrinking of the cell size introduced by the electric force between wires enhancing the gain at the chamber center; or some additional contribution not accounted for in the simulation, such as the charge screening effect of the first ionization cluster. Future studies will investigate this matter.

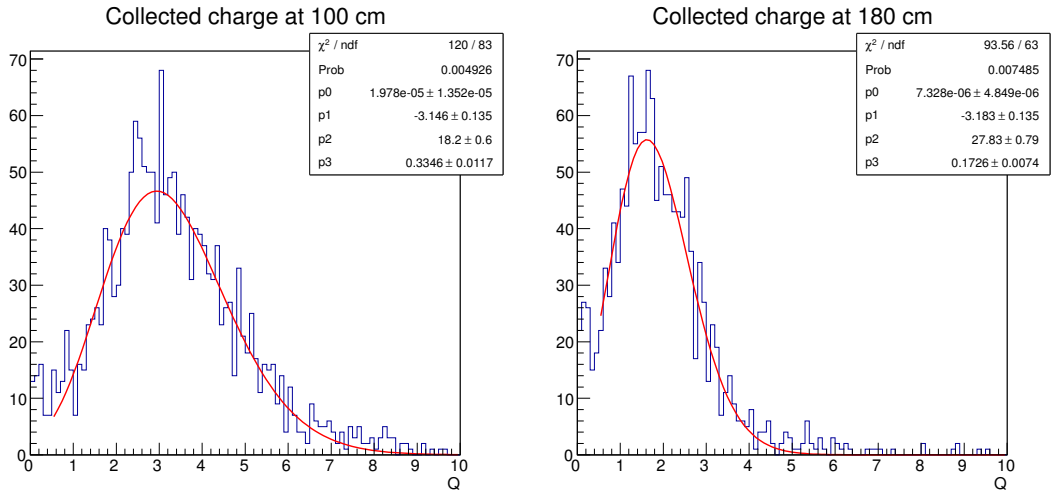

Figure 6.11: Example of total charge distribution with fit.

6.3.5 Wire Tension Measurements

An important quality check for drift chamber construction is a precise determination of wire tension. A common method (37) is based on inducing oscillations in the chamber wires, thus changing the mutual capacitance between the anode and neighboring cathodes.

A wire of fixed linear density μ with tension T supports standing waves of frequency

$$f_n = \frac{n}{2L}\sqrt{T/\mu} \tag{6.5}$$

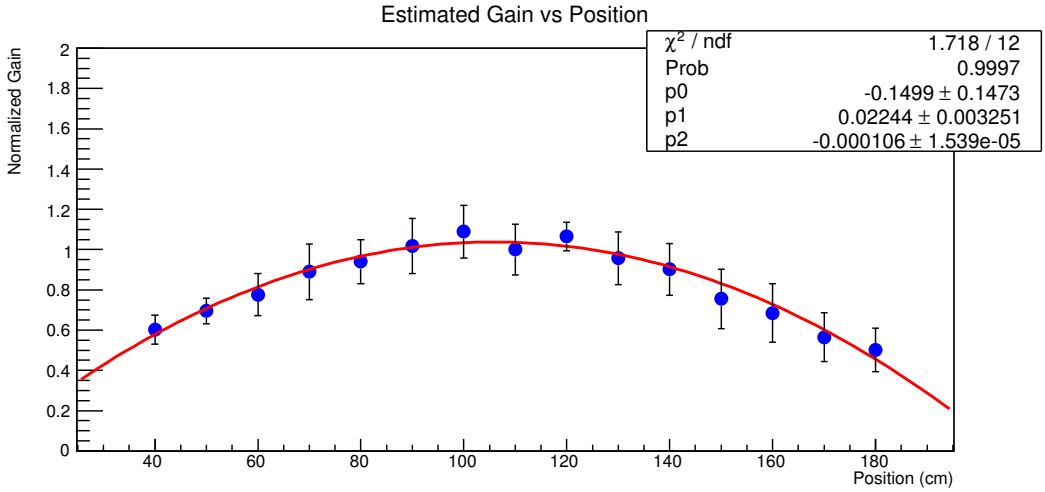

Figure 6.12: Gain variation along the z coordinate.

where n is an integer corresponding to the wave harmonic.

The construction of the long prototype offered an unique opportunity to test this method on a full length chamber. The expected resonance frequencies for our chosen wires are $f_{anode} = 53.7$ Hz and $f_{cathode} = 37.7$ Hz. Frequency measurements in this range are strongly affected by ambient noise and especially by 50 Hz electrical noise, making a naked wire measurement impossible. The measurement was thus performed after the insertion of the prototype into the shielded housing.

A Logitech Z523 speaker placed above the plexiglass chamber was used to resonate the wires at different frequencies and the resulting anode current was checked using an oscilloscope.

As an example, we report the Fourier transform of a signal resulting from a 54 Hz excitation of the anode wire. A peak corresponding to the anode resonance is clearly visible at ≈ 53.7 Hz, along with the 50 Hz peak from electrical noise and the 37.7 Hz peak from cathode oscillation pick-up. A number of additional peaks are also present, caused by various mechanical resonances with the drift chamber housing. These are dependent on the speaker position with respect to the plexiglass tube and make precise measurements difficult.

Nevertheless this test provides a useful proof of concept, to be later expanded with a dedicated prototype.

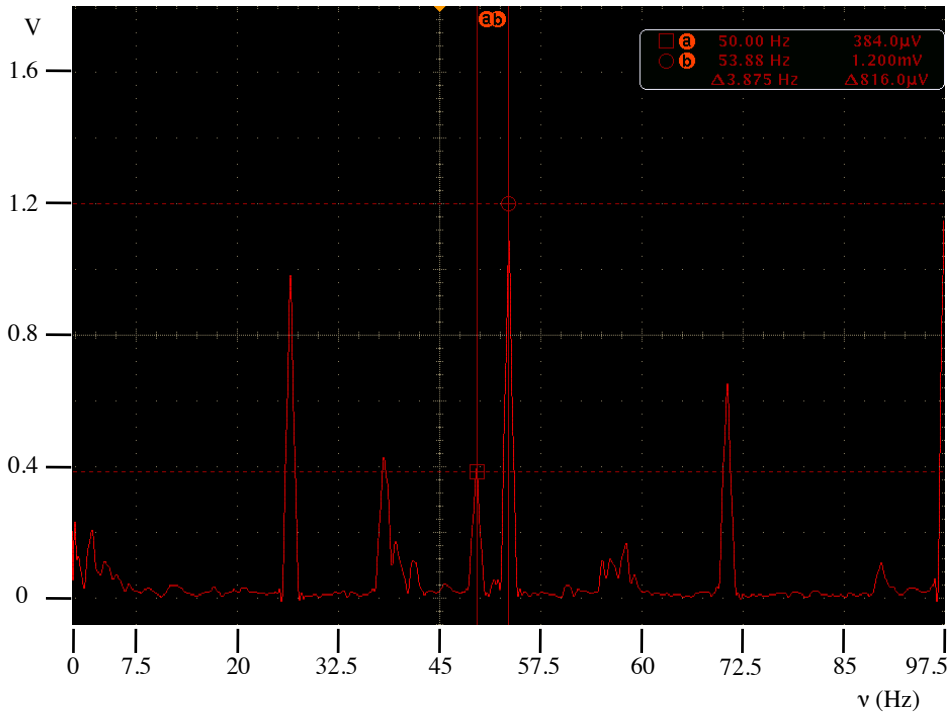

Figure 6.13: Frequency spectrum of anode current after 54 Hz excitation.

7

LXe Calorimeter Studies

In this chapter we will investigate the calorimeter's behavior in order to try and reconcile the observed differences in energy resolution between simulations and measurements. Were these differences partially unrelated to the inner face PMT geometry, they could be inherited by MEG II and negatively impact the ultimate sensitivity of the upgraded experiment. An algorithm based on a linear fitting technique will be used in an attempt to obtain a position-independent method of energy reconstruction.

7.1 Overview of Photon Energy Reconstruction

7.1.1 Standard Reconstruction Method

Gamma energy reconstruction in the LXe calorimeter is based on the weighted sum of the observed scintillation light $N_{pho,i}$ in each PMT, evaluated by correcting the collected charge q_i for the gain G_i and quantum efficiency QE_i. The weights ω_i are inversely proportional to the photo-cathode coverage of the i-th PMT region, and the quantity

$$Nsum2 = \sum_{i}^{N_{PMT}} \omega_i N_{pho,i} = \sum_{i}^{N_{PMT}} \frac{\omega_i q_i}{G_i QE_i} \tag{7.1}$$

approximates the total amount of scintillation light. This quantity shows, however, dependence on the gamma conversion point caused by geometrical effects, such as different shower escape, different leakage of scintillation photons, and different effects of reflection, scattering and absorption. An empirical position-dependent correction function $f(u, v, w)$ is extracted by mapping the calorimeter's response using CEX calibration

data for each *patch* (see Sec. 3.4.3.5) and applied to the sum, yeilding the corrected value

$$Nsum2_{corr} = f(u, v, w) \times Nsum2 \tag{7.2}$$

where $\{u, v, w\}$ are the calorimeter coordinates. The correction constant can vary throught time; temporal fluctuations of the function are monitored and accounted for through the use of Cockroft-Walton calibration events from proton capture in Lithium (17.6 MeV photons). The resolution σ_R at the signal energy $E_\gamma = 52.8$ MeV is obtained from a Gaussian fit of the same data to the high energy side of the spectrum and depends on the γ-ray conversion depth w: $\sigma_R = 1.7\%$ ($w > 2$ cm) and 2.4% ($w < 2$ cm).

7.1.2 Linear Fitting Algorithm

An alternate method was used during initial MEG I R&D, in a large 100 l prototype (25) of the final LXe calorimeter.

This method is based on Principal Component Analysis (PCA) (38, 39), a subset of multivariate analysis which allows fast extraction of relevant information (the so-called principal components) from complex data.

Let us represent each event as a point $\vec{N}_{pho}$ in N-dimensional measurement space, where N = 846 is the number of PMTs. The objective of PCA is to find a linear transformation $\vec{Y} = \mathbf{P}\vec{N_{pho}} + \vec{C}$ that induces a change of basis from the original basis (scintillation light, as seen by each PMT) to a different one that best expresses relevant information: total scintillation energy and shower spatial coordinates.

This transformation is normally extracted from collected data based on which axis exhibits the largest variance; this is under the assumption that large variance corresponds to interesting structure in data, while axis with low variance represent redundancy in the measurements (i.e. strong correlations).

In our case we instead use a MC simulation ($\approx 10^4$ events) to generate data with known values of energy and position and use them to teach the algorithm the proper transformation. We call this process *training*. The energy component of any data sample can then be written as

$$E_{PCA} = c_0 + \sum_{i}^{N_{PMT}} c_i q_i \tag{7.3}$$

and the coefficients c_i are obtained by minimizing the value

$$\chi^2 = \sum_{MC\ events} (E_{true} - E_{PCA})^2 \tag{7.4}$$

where E_{true} is the "true" energy value from Monte Carlo knowledge. The minimization process can be solved analytically, giving

$$c_0 = \langle E_{true} \rangle - \langle \sum_{i}^{N_{PMT}} c_i q_i \rangle \tag{7.5}$$

$$c_i = \frac{\mathcal{M}^{-1}}{N-1} [\sum_{MC\ events} E_{true} q_i] - \frac{1}{N} \sum_{MC\ events} E_{true} \sum_{MC\ events} q_i \tag{7.6}$$

where $\mathcal{M}$ is the covariance matrix

$$\mathcal{M}_{ij} = \langle (q_i - \langle q_i \rangle)(q_j - \langle q_j \rangle) \rangle \tag{7.7}$$

This algorithm is fast, simple and gave very good results during the prototype studies, with no need for ad-hoc correction functions. Its maximum effectiveness for the MEG I calorimeter can be estimated by applying the algorithm to a separately generated MC and results in $\sigma_R = 1.2\%$ for events at any depth

Whether this is achievable in practice strongly depends on the faithfulness of Monte Carlo simulation that is used for training. In the presence of discrepancies between simulation and data, as in the current case for the MEG LXe calorimeter, the results are of inferior quality.

Nevertheless, when compared to the standard method discussed in the previous section, this result suggests the existence of some limiting factor to the photon reconstruction which is not accounted for.

7.2 Looking for Possible MC/Data Discrepancies

We will search for discrepancies between simulations and real data which might limit the resolution of the LXe detector. The numerous calibration methods (described in Section 3.4.3) will be used for the comparison.

7.2.1 QE Angular Dependence

A first disagreement between data and Monte Carlo is found in the treatment of scintillation light at different angles of incidence of scintillation light on individual PMT surfaces. This can be seen by comparing signals coming from known positions in space, such as those from α-sources used for QE evaluation. The plot in Fig. 7.1a shows the observed data/MC signal ratio for each of the calorimeter PMTs and each of the 25 calibration α-sources as a function of source-PMT angle.

In the past, implementation of polarized reflections in the calorimeter simulation (40) managed to improve the ratio uniformity and thus the energy resolution. It stands to reason that further improvement could be achieved by taking into account hitherto disregarded contributions.

The Monte Carlo simulation tracks scintillation lights only up to the PMT quartz window, counting photons that do not get reflected or absorbed as hits. There is, however, a further potential step that is not currently accounted for: photons could potentially cross the quartz volume but get reflected on the photocathode surface.

The best test for this effect is obtained by comparing the relative ratio of collected scintillation light between real and simulated α events. As this effect naturally depends from light incidence angle, it must be compared indipendently for each PMT-source pair.

Multiple simultions for different values of photocathode reflectivity were tested. The best results were obtained for 60% reflection and can be seen in Fig. 7.1b compared to non-reflecting photcathodes, as a function of the incident angle. As we can see, the angular dependence is partially mitigated with the new reflections with a 15% reduction in RMS.

The new simulation was used to evaluate a new set of quantum efficiencies for the calorimeter which were then applied to data from 17.6 MeV γ-rays from Cockroft-Walton Lithium calibrations (CWLi). The results are shown in Tab. 7.1.

The minimal improvement in the width of the reconstructed light peak suggests that while this is an improvement in the accuracy of the simulation, its effect on actual resolution is of secondary importance. We must thus look elsewhere for effects introducing large improvements.

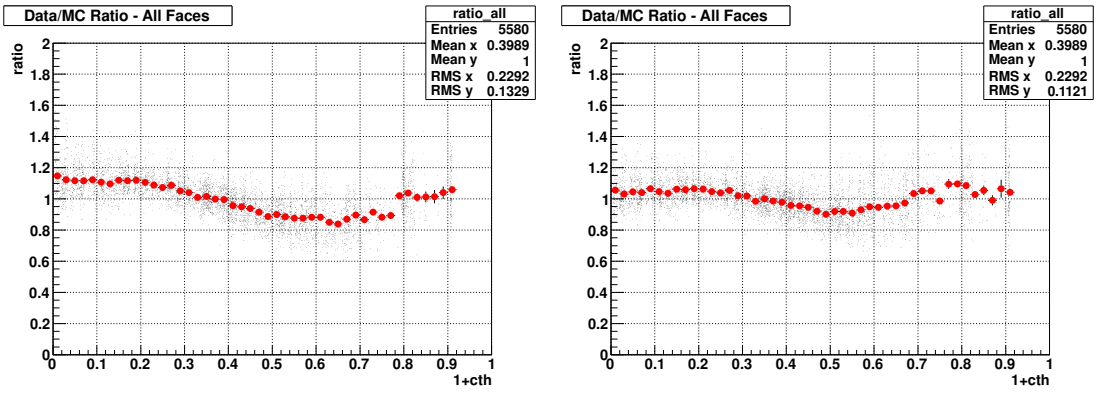

(a) No reflection

(b) 60% reflection

Figure 7.1: Data/MC ratio for α-source signals as a function of γ angle of incidence on PMTs without and with photcathode reflection.

Depth	$Nsum2$, no refl.	$Nsum2$, 60% refl.
$w < 2$ cm	4.8%	4.7%
$w > 2$ cm	3.8%	3.7%

Table 7.1: Change in light peak width after the introduction of photocathode reflections.

7.2.2 Search for Detector Asymmetries

Alternatively, the discrepancies discussed above could be due to calorimeter non-uniformities, arising from local or global distorsions of the detector volume of various origin. To check this experimentally, we first need to define a quantitative estimator that suits our purposes. Once a model for the asymmetries were found, it could be implemented into the simulations to reconcile the differences.

Let us consider a shower vertex reconstructed at a certain point (u, v) in the calorimeter's system of coordinates. Assuming a uniform, symmetrical geometry, the total collected scintillation light in a given surface (for example, the calorimeter's top face) should be equal to the collected light on the opposite surface (i.e. the bottom face) for events originating from the symmetrical position, $(u, -v)$.

Thus we can define an *asymmetry estimator*

$$A(u,v) = \frac{\mu^{top}(u,v) - \mu^{bottom}(u,-v)}{\mu^{top}(u,v) + \mu^{bottom}(u,-v)} \tag{7.8}$$

where μ is the mean value of the observed light distribution in a given face as a function of the gamma event position (see Fig. 7.2-7.3).

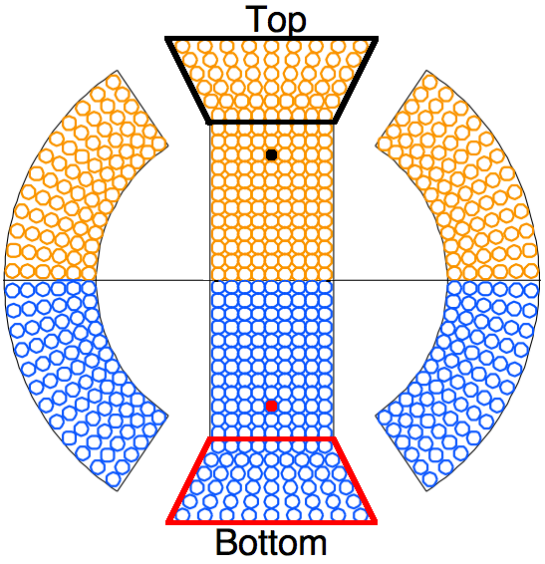

Figure 7.2: Symmetrical event positions used for asymmetry evaluation (black and red dots) and corresponding studied faces.

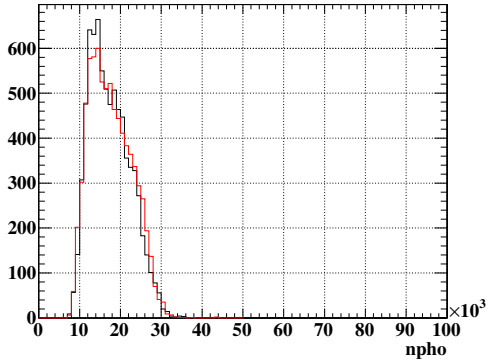

Figure 7.3: Sample top face (black) and bottom face (red) signals for symmetrical events.

We map this estimator over a fine 27×36 mesh over the top half of the calorimeter, such that each bin covers 1/3x1/3 of a PMT. The studied faces have dead PMTs: the estimator is computed by excluding the corresponding PMTs on the opposite face, thus forcing symmetry in the values for collected light. In addition, other PMTs which display very low and/or unstable gain are also excluded. The affected PMTs are shown in Fig. 7.4.

For the purpose of this analysis we examine $\sim 10^6$ γ events used for energy scale calibration: 55 MeV photons from π^0 decay and 17.6 MeV photons from Li capture.

As can be seen from Fig. 7.5 the average top/bottom asymmetry of the calorimeter for Li capture events is on the scale of a few percent. Additionally, the asymmetry distribution tends to widen as one approaches the center of the calorimeter. This is expected as fewer photons manage to reach the top and bottom faces.

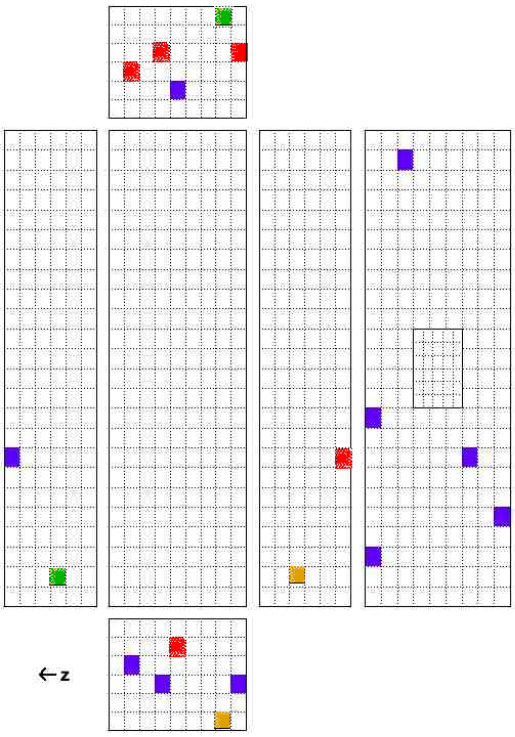

Figure 7.4: PMT map of the LXe calorimeter.
Purple: Dead PMT.
Red: Symmetrical to above.
Orange: Low gain PMT.
Green: Symmetrical to above.

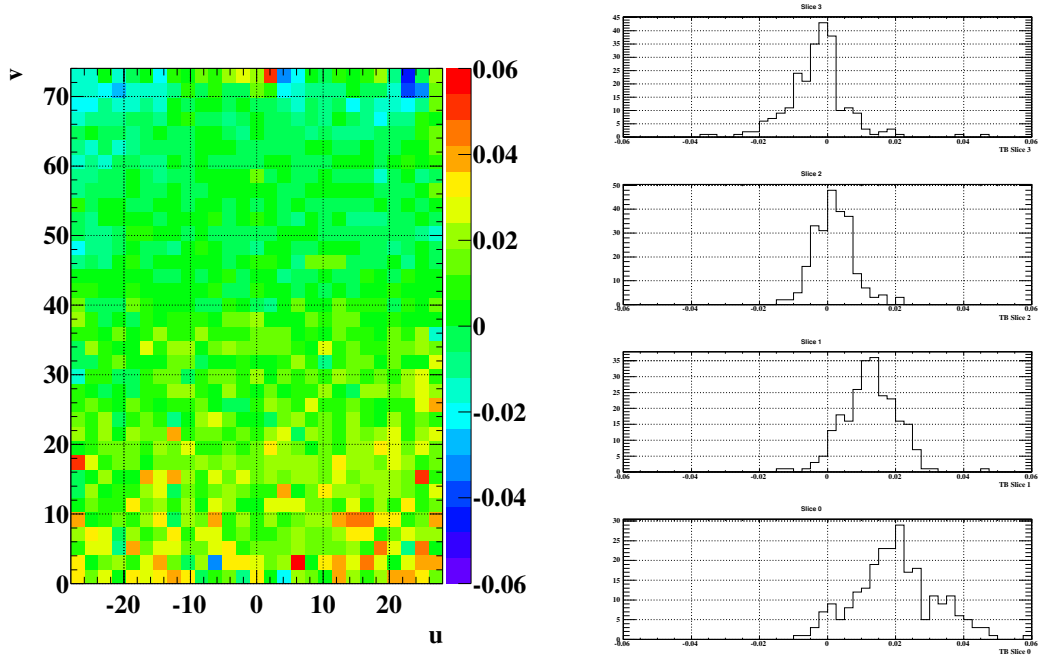

Figure 7.5: (Left) Top/bottom asymmetry map for 17.6 MeV Li capture events. (Right) Asymmetry distributions and their evolution along the vertical axis.

On the other hand, the asymmetry seems to favor the top face (i.e. the estimator becomes positive) as we move towards the center; this behaviour is also present for π^0 data (see Fig. 7.6). Furthermore, π^0 events display an overall negative shift of -2% and exhibit non-uniform distributions far from the detector center, with asymmetries as high as -6%. These effects are replicated in 83 MeV events originating from the same decay.

This energy- and position-dependent behavior has to be understood to obtain a complete model for calorimeter non-uniformities.

We checked if the detector's asymmetrical response might be caused by mechanical deformations of the cryostat structure during the cooling process by exploring various Monte Carlo simulations of the calorimeter in altered configurations. We were unable to reproduce the measured asymmetries even with large distorsion of the geometry, thus excluding this possibility.

As an example, Fig. 7.6 shows the impact of a simulated 2° tilt in the bottom calorimeter face, roughly equivalent to a 1 cm deformation. No structure is apparent.

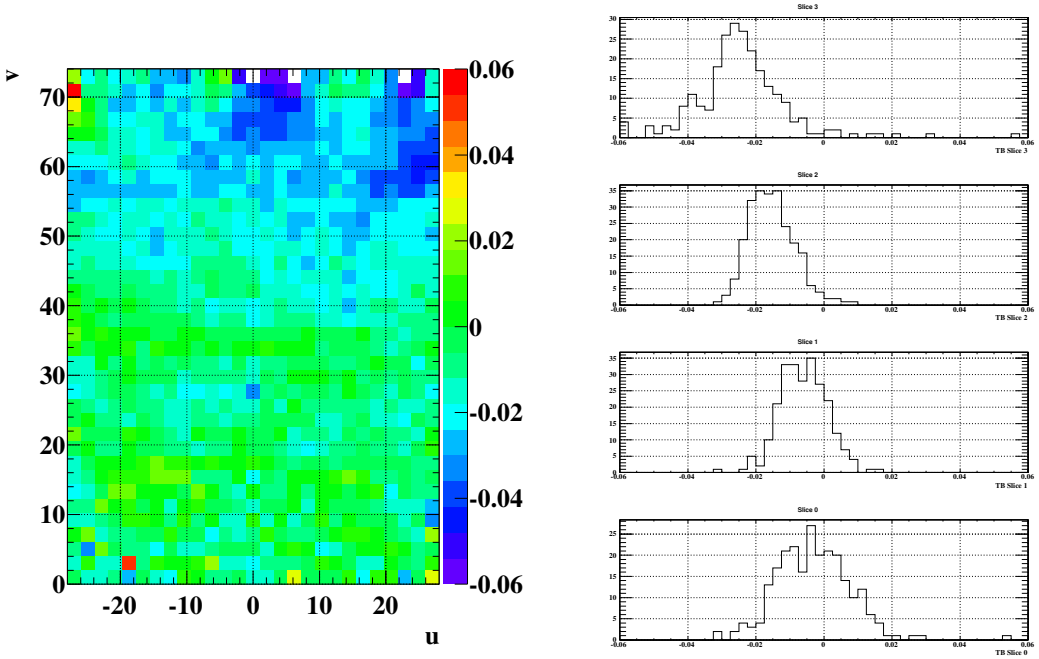

Figure 7.6: (Left) Top/bottom asymmetry map for 55 MeV π^0 decay events. (Right) Asymmetry distributions and their evolution along the vertical axis.

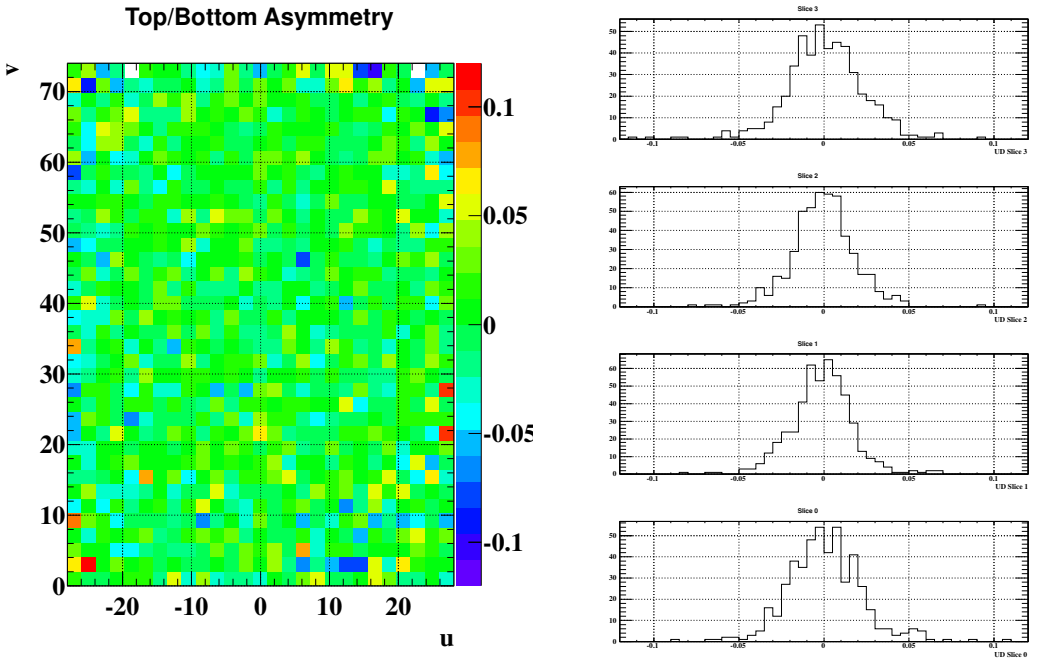

Figure 7.7: (Left) Top/bottom asymmetry map for 17.6 MeV γ from MC with bottom face tilt. (Right) Asymmetry distributions and their evolution along the vertical axis.

7.2.3 Calorimeter Response in MC and Data

We can examine these irregularities in more depth by studying the behavior of collected light *nsum2* as a function of the vertical calorimeter axis. Given a specific monochromatic energy probe, a perfect calorimeter would supposedly give the same response independently of the position where the photon signal used for probing produces a shower.

As alread discussed, this is not true in the data. Consider for example Fig. 7.8, which displays the normalized values for the mean of the light peak corresponding to the 17.6 MeV calibration signal in 2009 data and in simulations. The drops at the end of the graph are expected and correspond to containment losses, while the irregular shape is born from real irregularities in the light response.

It is however important to note that not even the MC simulation provides a flat response. While the inner and outer faces of the calorimeter ideally contribute to light collection independently on position, the top and bottom faces give greater contributions for events closer to them. The resulting characteristic saddle-like shape is clearly visible in the picture.

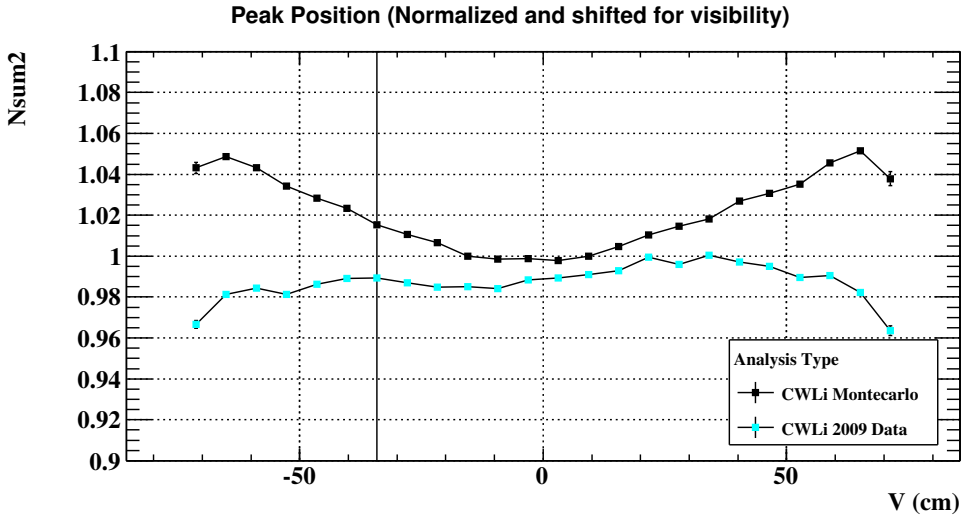

Figure 7.8: Peak of collected light for 17.6 MeV γ in Monte Carlo and officially reprocessed 2009 data.

Nevertheless the two behaviors are significantly different: the Monte Carlo response is symmetric, while data presents, in addition to the asymmetries already shown in the

last section, a completely different shape.

7.2.4 Quantum Efficiencies in Liquid and Gas

Mechanical deformations being excluded, a candidate for this effect is an erroneous evaluation of PMT quantum efficiencies.

Quantum efficiencies in MEG are extracted by comparing the collected light expected from Monte Carlo simulations to data from α sources. As discussed in Section 3.4.3.2, this data is usually acquired in liquid phase to serve as a monitor of detector stability. However the acquisition of α events in liquid introduces additional complexity in the reconstruction which needs to take into consideration the LXe optical properties.

To exclude these factors, we produced a set of QEs using data collected in gas phase at the beginning of the year. A re-analysis 2009 CWLi calibration data these quantum efficiencies was performed. The resulting energy response (Fig. 7.9) shows a much better agreement with the MC expectation, suggesting that QEs obtained in gas are a more accurate estimate of the real values. A cross check on 55 MeV CEX data shows the same results (Fig. 7.10) which have also been verified to be consistent across years.

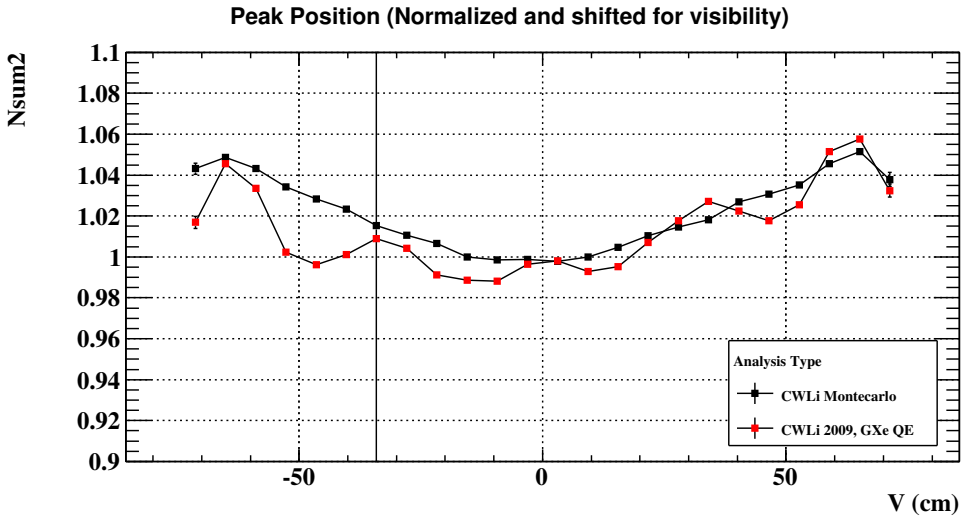

Figure 7.9: Peak of collected light for 17.6 MeV γ in Monte Carlo and 2009 data reanalyzed with QEs extracted in gas.

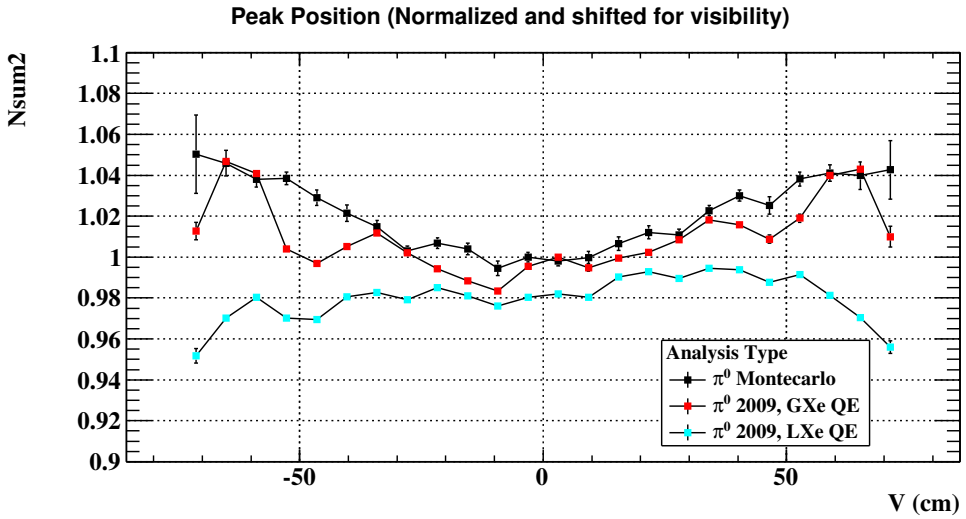

Figure 7.10: Peaks of collected light for 55 MeV γ from pion charge exchange reaction.

The improved faithfulness of gas-evaluated quantum efficiencies is further proven by comparing the ratio of collected light for each PMT-source pair, as done in Section 7.2.1. The comparison for PMTs belonging to each face is shown in Fig. 7.11 and 7.12 and a reduction of angular dependency in the outer, top and bottom faces of the calorimeter is clearly visible.

When using GXe QEs, however, two new issues arise which must be considered.

First, the simulation for upstream and downstream faces significantly underestimates the collected light at very high angles. The exact behavior of reflections at very high incidence angles is heavily affected by local irregularities and is tricky to model. Fortunately, the amount of source-PMT pairs where the α events are seen at high angles is quite low, on the order of a few percent for $(1 + \cos\theta) < 0.7$. An angular cut can eliminate those pairs from the QE evaluation.

The second and more pressing issue, as evident from Fig. 7.9 and 7.10, is the appearance of four regions where the data peak curve deviates from the MC expectation. These irregularities correspond spacially to regions in-between the source wires and are caused by a systematic overestimation of QEs for inner face PMTs. This is caused by the fact that those PMTs can only see events originating from the two closest wires because of the geometric constraints of the curved calorimeter. All the sources involved are at similar distances and angles to the PMT and as a result the the points of the

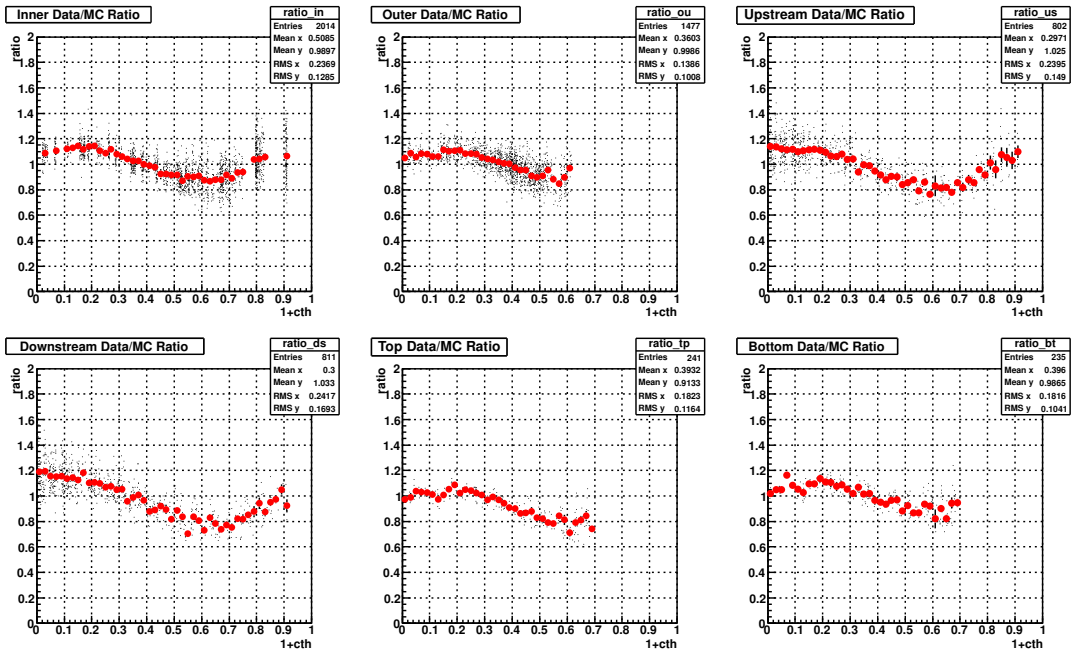

Figure 7.11: Data/MC signal ratio for α-sources in LXe as a function of γ angle of incidence on PMTs.

fit are clumped together, which together with the reduced amount of points leads to a less accurate fit, as can be seen for example in Fig. 7.14.

We can map the irregularities across the calorimeter (u, v) coordinates by normalizing the fitted peak mean value for events in each region to the Monte Carlo expectation, showing a clearer picture of the issue in Fig. 7.15.

The position of sources is constrained 2-dimensionally by the source wire, but their staggered positioning is subject to uncertainties along the u axis and can be adjusted in the Monte Carlo within these same uncertainties in order to minimize the irregularity.

The smoothest result is obtained for a shift of $(-0.08, -2.0, 0.54, 3.1, -0.05)$ combined with a phenomenological upwards shift of the bottom wire by $\theta = 0.5°$, the result of which is shown in Fig. 7.16. The distribution of the Data/MC ratios before and after the shift is shown in Fig. 7.17). After the shift the distribution is narrower, with a $\approx 21\%$ reduction in RMS.

The irregularities cannot be completely eliminated, as they arise from the particular arrangement of the calibration sources in the detector.

Ultimately, this suggests that if *alpha*-source calibration for the MEG II were to be

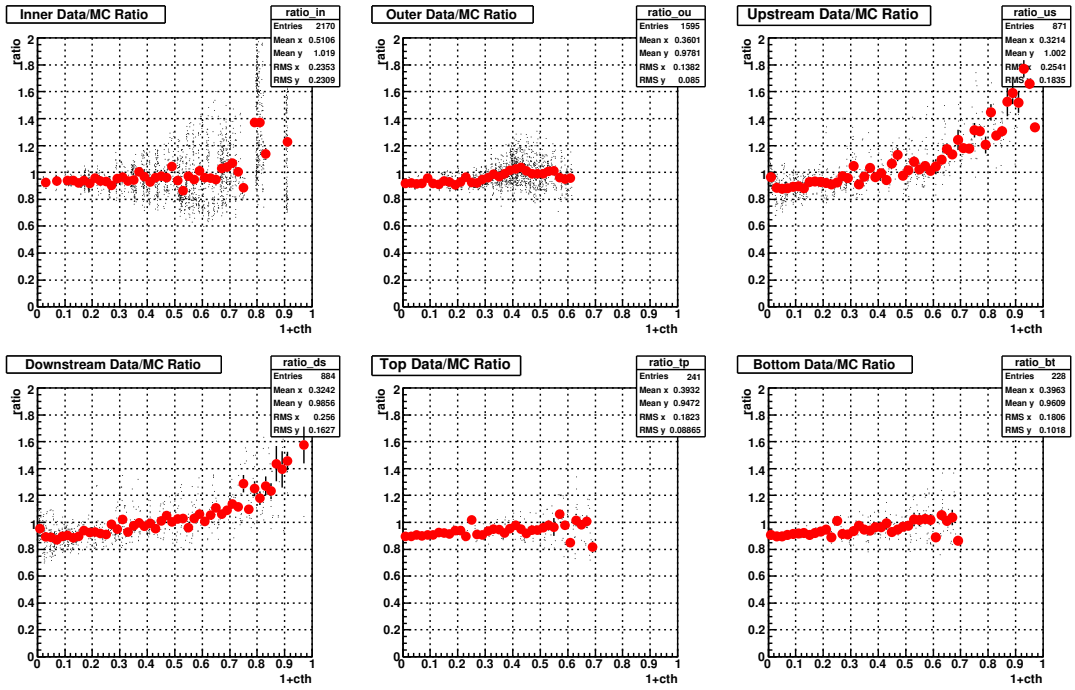

Figure 7.12: Data/MC signal ratio for α-sources in gas phase Xenon as a function of γ angle of incidence on PMTs.

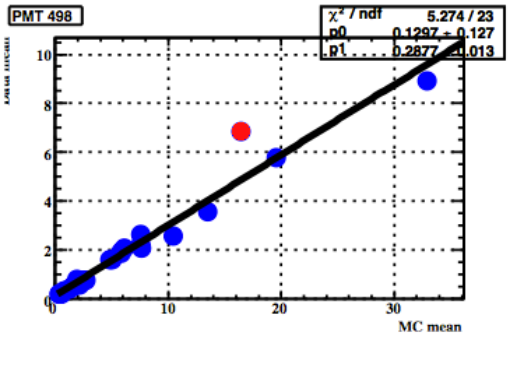

Figure 7.13: QE fit for a PMT on the upstream face with a source with high incidence angle (red point). Excluding the source improves the quality of the fit.

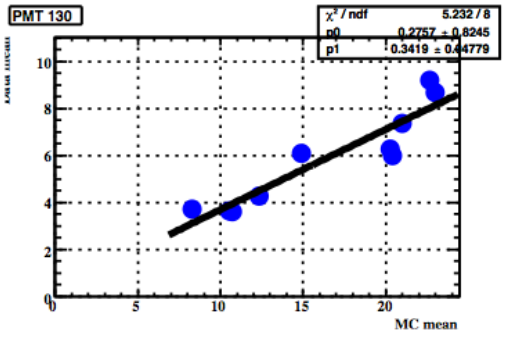

Figure 7.14: QE fit for an inner face PMT equidistant from two source wires.

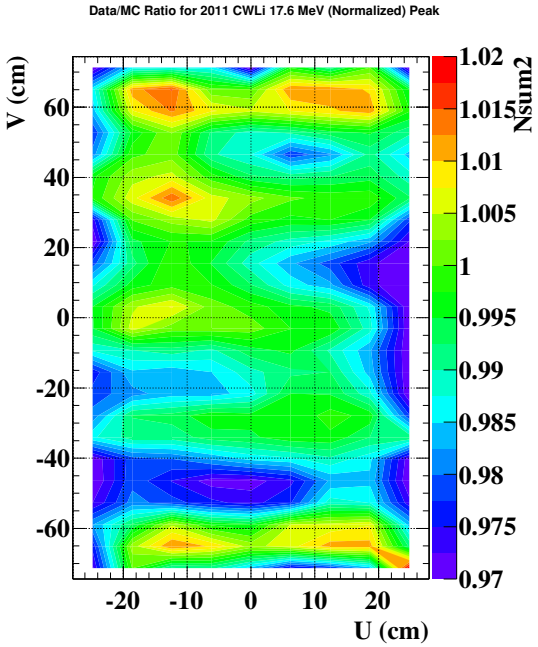

Figure 7.15: Data/MC 17.6 MeV peak ratio map for GXe QEs.

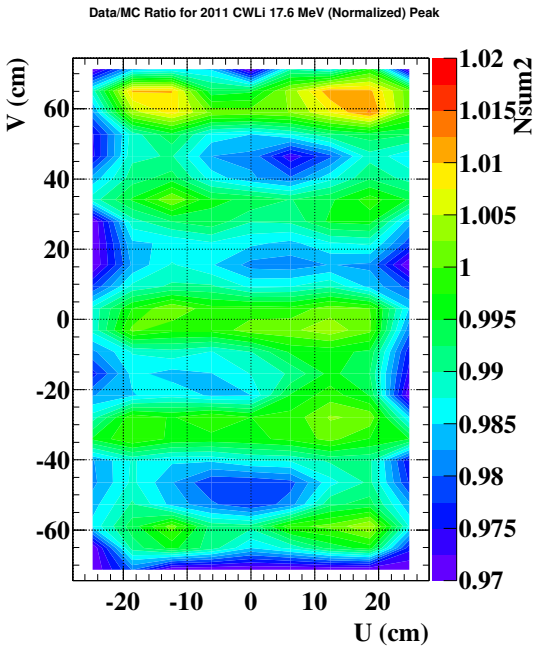

Figure 7.16: Data/MC 17.6 MeV peak ratio map for GXe QEs with shifted wires.

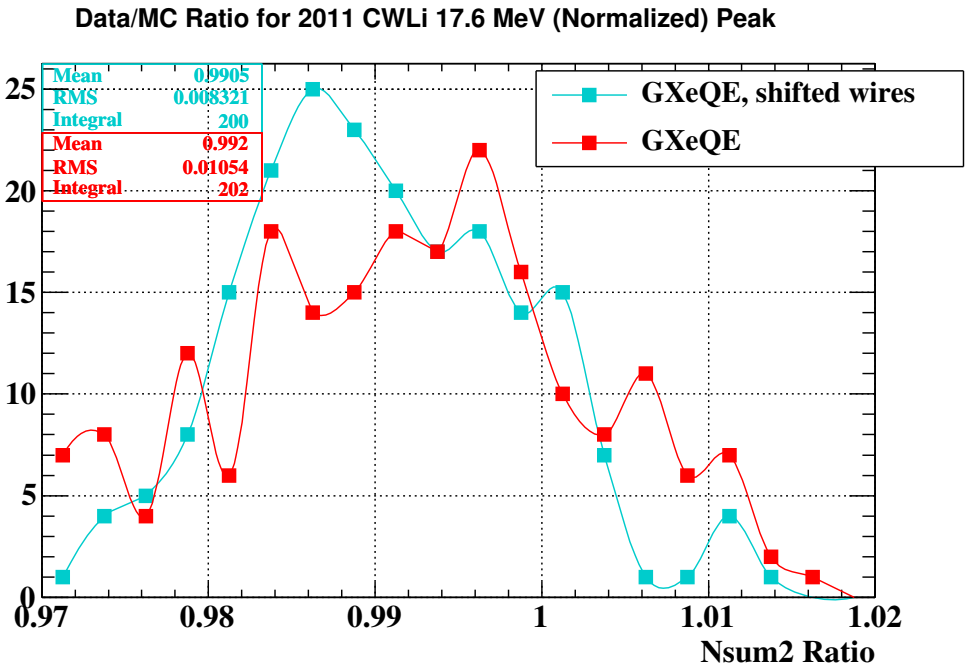

Figure 7.17: Data/MC signal peak ratio before (red) and after (blue) wire shifts in QE evaluation.

performed in GXe, it would benefit from having additional sources to reduce granularity and provide additional calibration points.

7.2.5 Monte Carlo Fine Tuning

As a quality test of the QEs obtained in gas phase, we use π^0 runs from 2009 data and compare the collected light per calorimeter face to the expected simulated values. To this purpose, we use data from *patch 8* runs (see Section 3.4.3.5).

Simulation of scintillation light in the MEG Monte Carlo depends on several parameters. Light transportation in particular is affected by Rayleigh scattering, absorption of scintillation light and the various optical properties of the calorimeter materials.

The refraction indexes of LXe and PMT quartz windows are based on fixed formulas obtained from experimental measurement, which will be discussed later.

The plastic material used for the inner face wall (PEEK) has no accurate known measurements for ultraviolet, low temperature refraction indexes. A fixed value of $n_{PEEK} = 1.844$, independent of wavelenght have been used in the past, but repeated

testing shows negligible contributions to the results for values as high as $n_{PEEK} = 2.1$

The Aluminum reflectivity R_{Al} is treated in the Monte Carlo as a free parameter, as attempts to model reflections on the LXe-Al interface clashed with known experimental measurements (40). As the Aluminum surface is not perfectly smooth, a percentage R_{rand} of the reflected light is instead randomly scattered.

The total attenuation length of of LXe was measured experimentally in the 100 l MEG prototype (25) to be

$$\frac{1}{\lambda_{att}} = \frac{1}{\lambda_{Ray}} + \frac{1}{\lambda_{abs}} = 40 \pm 2.5\text{cm}^{-1} \tag{7.9}$$

All the mentioned parameters were tuned to maximize the agreement of the Monte Carlo with the reanalyzed data. The best values found for this comparison were:

1. Rayleigh scattering length $_{Ray} = 45$cm.
2. Absorption length $_{abs} = 400$cm.
3. PEEK refraction index $n_{PEEK} = 1.8$.
4. Aluminum reflectivity $R_{Al} = 63\%$ with a 30% random component.

The obtained best values for Rayleigh scattering and absorption lenghts are in particular in excellent agreement with the experimental measurements. The plot in Fig. 7.18 shows the agreement achieved between data and simulations for each face of the calorimeter. The cuts used are:

1. *patch 8* selection: $|u| < 9.3$ and $18.6 < v < 37.2$
2. 90% of energy from events in the NaI coincidence detector deposited in the central crystal.
3. Pileup rejection on real events. Monte Carlo simulated without pileup event.

Every face displays excellent agreement except for the inner and outer ones, where the Monte Carlo respectively overestimates and underestimates the signal from experimental data, in a manner similar to a shift in energy scale. For this reason, a phenomenological inward shift $\delta R_{wi} - 1$ cm of α-source wires was introduced in the α simulation, leading to the new comparison in Fig. 7.19.

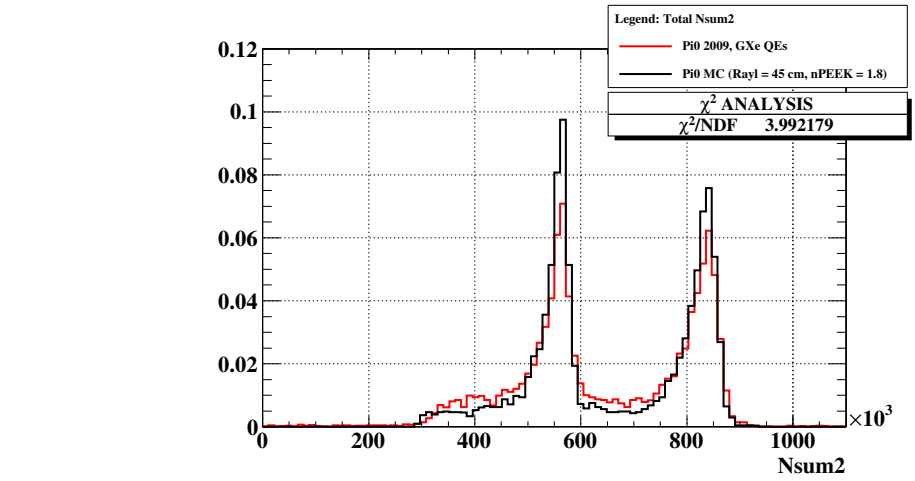

(a)

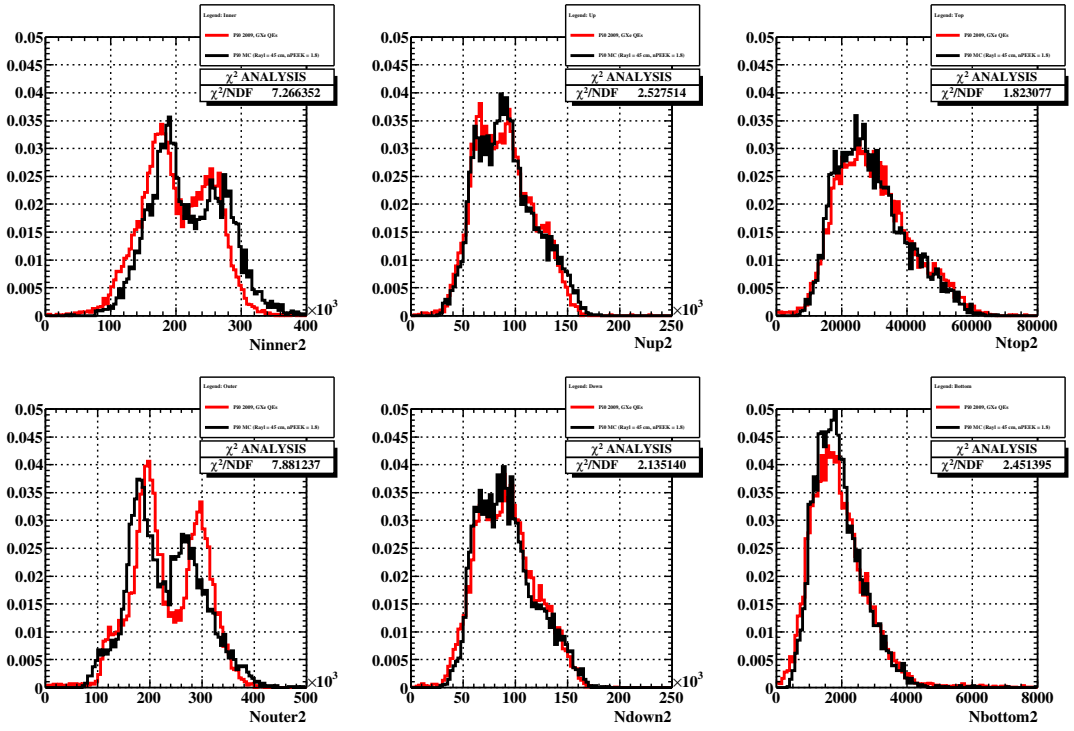

(b)

Figure 7.18: Light spectrum of π^0 data with GXe QEs (red) and Monte Carlo (black) events for the full calorimeter (a) and each individual face (b).

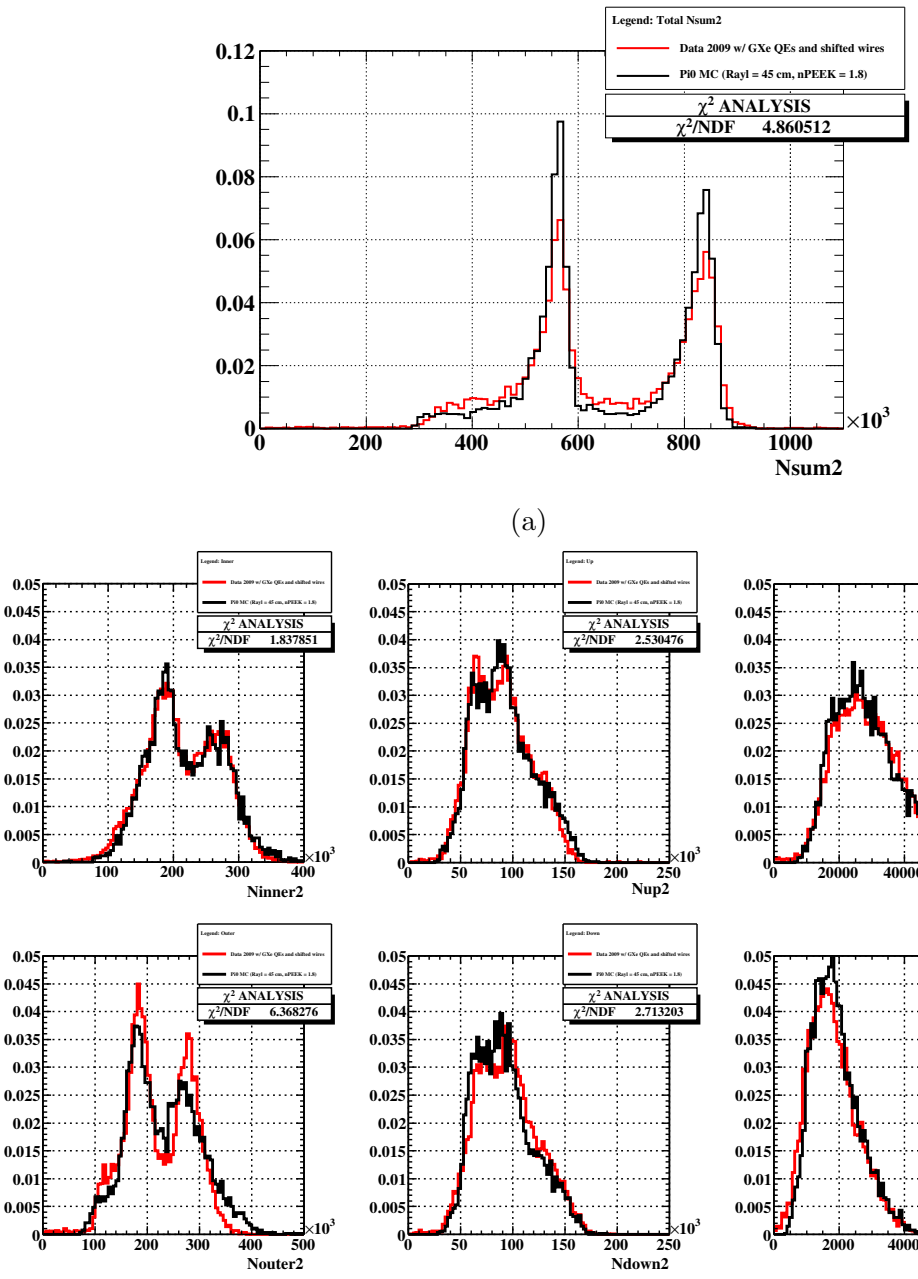

(a)

(b)

Figure 7.19: Light spectrum of π^0 data with GXe QEs (red) and Monte Carlo (black) events for the full calorimeter (a) and each individual face (b) after applying radial -1 cm wire shift in α simulations.

The agreement obtained is satisfactory on every face except for the outer one, where the differences between the distributions cannot be resolved with a simple shift in the energy scale.

The plot of the anomalous outer face versus the rest (Fig. 7.20) shows enhanced light collection on the outer face for Monte Carlo events.

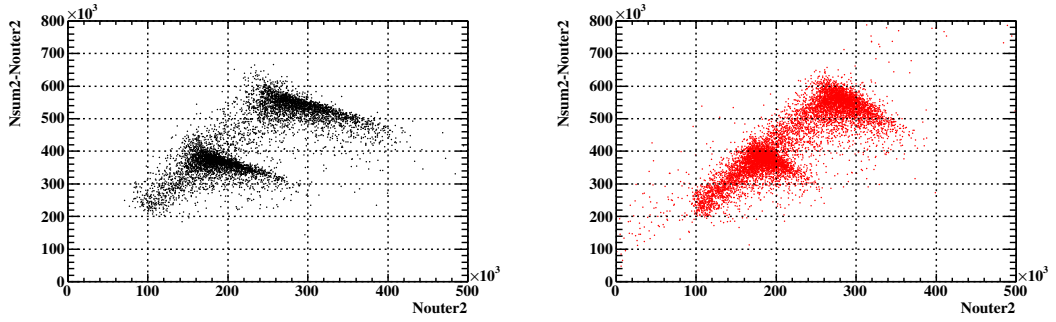

(a) (b)

Figure 7.20: Correlation plots for light collection in the outer face (*nouter2*) vs the remaining faces (*nsum2-nouter2*) showing different shapes for Monte Carlo (a) and π^0 data (b).

A more detailed study can be performed by extending the comparisons of collected light for each face to a bidimensional profiled scatter plot in order to examine behaviors of simulated and real data at different event depths (w) which can be seen in Fig. 7.21. A deviation is apparent in the outer face for high w, with an enhancement in collected light for deep shower events.

To exclude the possibility of trigger bias which could cut out deeper events producing a high level of light in the outer face, the π^0 single patch trigger conditions were implemented as an additional selection to Monte Carlo events, requiring the PMT with the highest signal in the inner face to belong to the patch the data is acquired in. This excluded 15% of simulated events during analysis, but was shown to be redundant with the geometrical patch selection and have negligible impact on the final comparison.

On the other hand it can be shown that the enhancement is primarily seen in light collected at high angles. By looking to the light collected by outer face PMTs uniquely belonging to the ($|u| < 9.3$, $18.6 < v < 37.2$), corresponding to *patch 8*, the agreement between data and Monte Carlo is restored (Fig. 7.22). The signal in these PMTs is

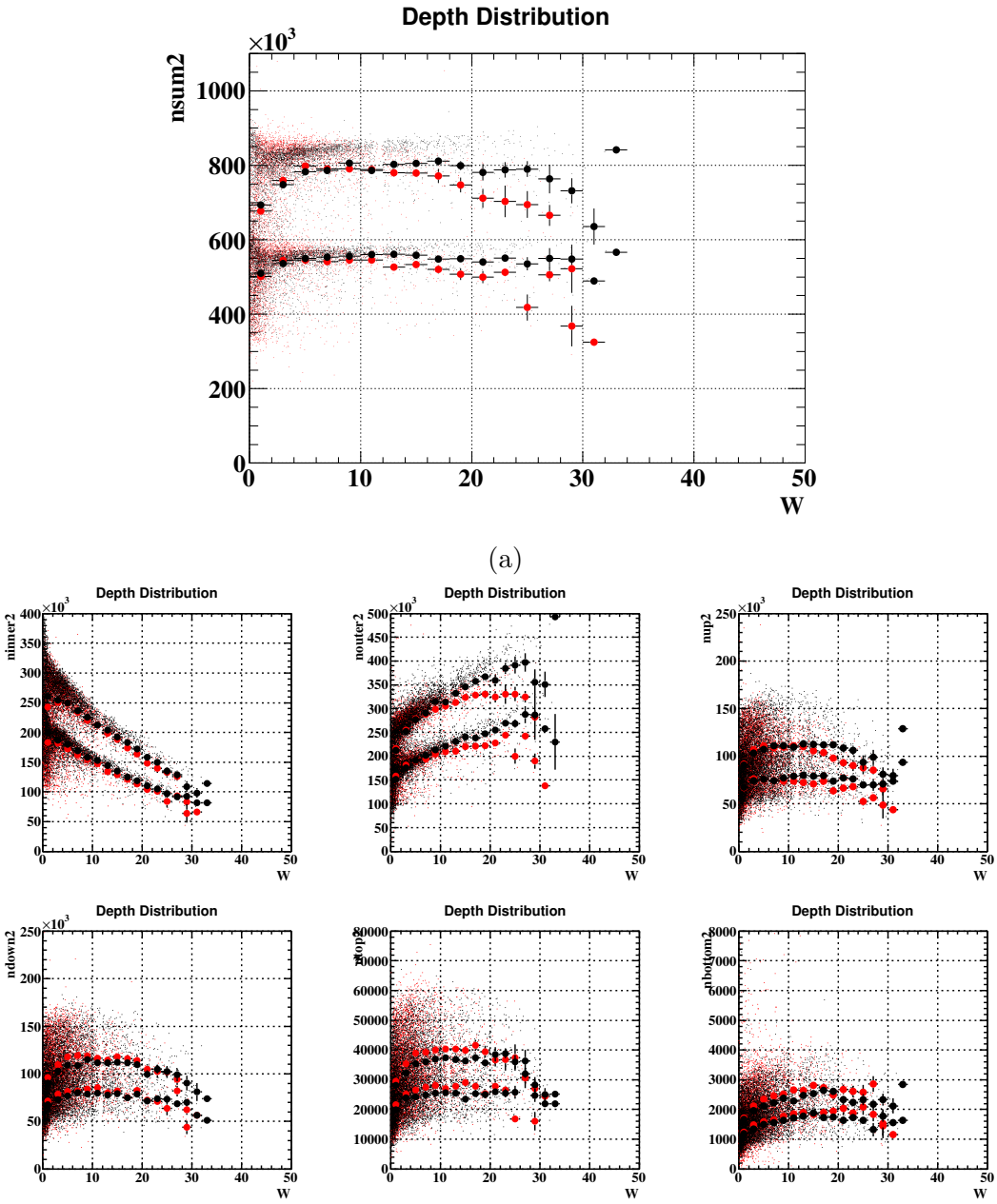

(a)

(b)

Figure 7.21: Profiled scatter plot of π^0 data with GXe QEs (red) and Monte Carlo (black) events for (a) the full calorimeter and (b) each individual face, as a function of event depth.

dominated by direct light. Meanwhile adiacent PMTs, which see events at a greater angle, are already subject to the anomaly (Fig. 7.23).

It is thus reasonable to attribute this difference to an incomplete understanding of reflection parameters on the PMT surface, which are strongly dependent on the refraction indexes used.

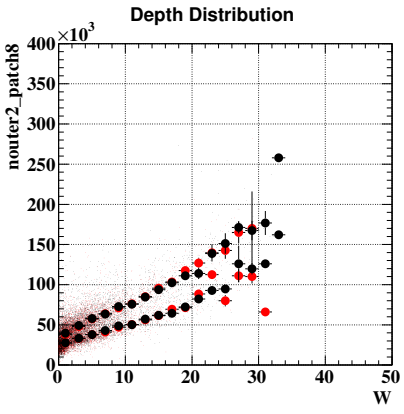

Figure 7.22: Scatter plot of π^0 data (red) and Monte Carlo (black) for the outer face PMTs in *patch8*.

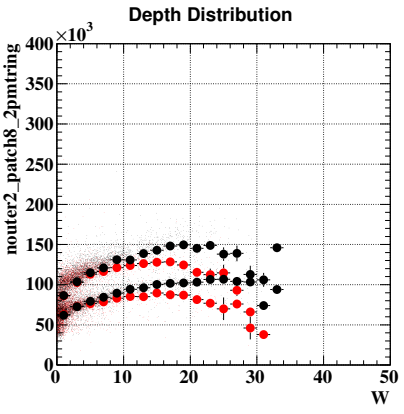

Figure 7.23: Scatter plot of π^0 data (red) and Monte Carlo (black) for the PMTs surrounding the outer face *patch8* PMTs.

7.2.6 Refraction Indexes

It is important to note at this point that refraction indexes of calorimeter materials are not constant, but instead $n = n(\lambda)$. The values implemented in the Monte Carlo are empirical formulas obtained from interpolation of experimental measurements of liquid xenon (Eq. 7.10) and quartz (Eq. 7.11) refraction indexes:

$$n_{LXe} = \frac{2.82 \cdot 10^{-6}}{4.52 \cdot 10^{-5} - \frac{1}{\lambda^2}} + \frac{5.21 \cdot 10^{-4}}{4 \cdot 10^{-4} - \frac{1}{\lambda^2}} \tag{7.10}$$

$$n_{quartz} = 1.464 + e^{0.1869 - 0.01354\lambda} \tag{7.11}$$

where wavelenght λ is in nm. Xenon scintillation light distribution is approximately gaussian, with a peak wavelenght of $\lambda = 178$ nm and $\sigma_\lambda = 6$ nm.

The values for the parameters currently used to model $n_{LXe}(\lambda)$ in Eq. 7.10 were obtained through measurements performed at KEK (41). A contemporary measurement by Hitachi et al. (42) provides a somewhat different model:

$$\omega = 1.2055{\cdot}10^{-8}\,\frac{2}{3}{\cdot}\frac{\rho_{liq}}{\rho_{gas}}\left(\frac{0.26783}{4.374177\cdot 10^{-5}-\frac{1}{\lambda^2}}+\frac{0.29481}{5.747915\cdot 10^{-5}-\frac{1}{\lambda^2}}+\frac{5.03333}{1.1274\cdot 10^{-4}-\frac{1}{\lambda^2}}\right) \tag{7.12}$$

$$n_{LXe}=\sqrt{\frac{1+2\omega}{1-\omega}} \tag{7.13}$$

where $\rho_{liq} = 2.908$ and $\rho_{gas} = 5.8984\cdot 10^{-3}$ are the liquid and gas phase xenon densities, respectively. All the models mentioned are displayed in Fig. 7.24.

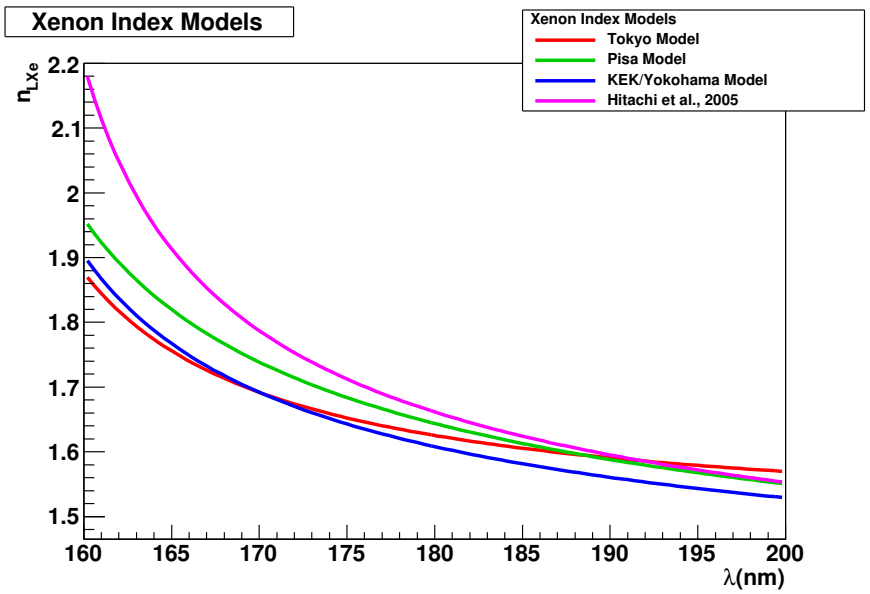

Figure 7.24: Different models for LXe refraction index in a $3\sigma_\lambda$ region around the 178 nm scintillation peak. (41, 42)

As far as n_{quartz} is concerned, while measurements of quartz optical properties have been performed in the past (43, 44, 45), they typically do not extend into our wavelength region of interest. Two separate parametrizations of were adopted in Tokyo and Pisa, the former of which corresponds to Eq. 7.11. They are shown in Fig. 7.25 together with empyrical fits of the experimental measurements, extended into the 160-200 nm region.

The Pisa model, corresponding to

$$\omega = 0.10464 + \frac{26.474}{(161.78 - (\frac{1240}{\lambda})^2)} \tag{7.14}$$

$$n_{quartz} = \sqrt{\frac{1+2\omega}{1-\omega}} \tag{7.15}$$

is in good agreement with the extension of published values for fused silica (44) and must thus be considered as an alternative over its Tokyo counterpart.

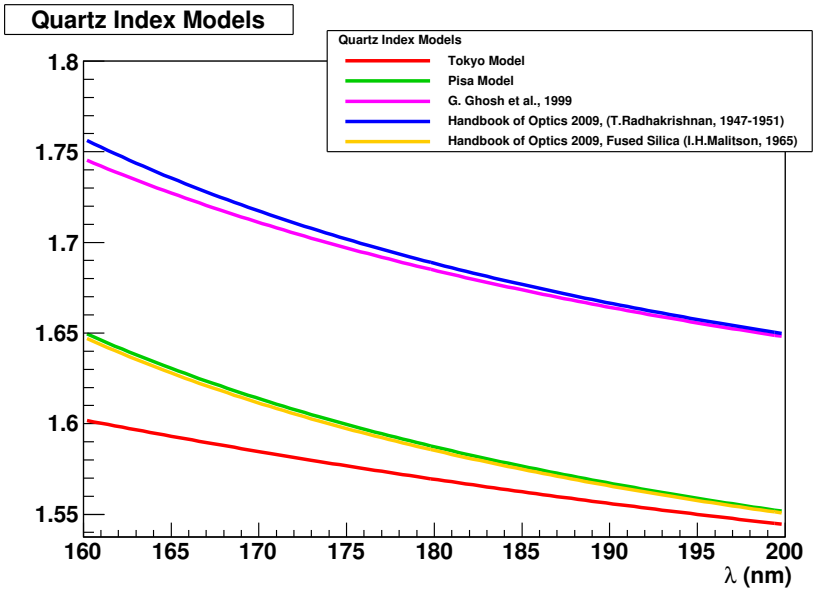

Figure 7.25: Different models for crystalline and fused quartz refraction index in a $3\sigma_\lambda$ region around the 178 nm scintillation peak. (43, 44, 45)

A glimpse at the behavior of scintillation light at different angles, which is strongly influenced by the parameters above, can be obtained by normalizing (event per event) the light signals of each outer face PMT to its solid angle coverage of the event shower. The normalization factor is $\sim \frac{d^2}{\cos(\theta)}$, where d is the distance and θ the angle between the PMT and the shower vertex. Due to the fact that the shower develops deeper than the conversion point, this normalization factor is underestimated at low θ and overestimated at high θ. Nevertheless, it provides a qualitative estimate of the impact of different properties.

The profiled scatter plots in Fig. 7.26, taken for event-outer PMT pairs with $d <$ 60 cm over $\approx 2 \cdot 10^4$ events, show the differences at high angles between data and simulations, as suggested in the previous section.

Different combinations of refractive indexes were extensively tested and compared. The Pisa model for n_{quartz} and the n_{LXe} from Hitachi et al. (42) were selected for their close match to the real detector response. The collected light normalized to solid angle for the new indexes is shown in Fig. 7.27 while the comparison with data for outer face PMTs surrounding the patch region, equivalent to Fig. 7.23, is shown in Fig. 7.28.

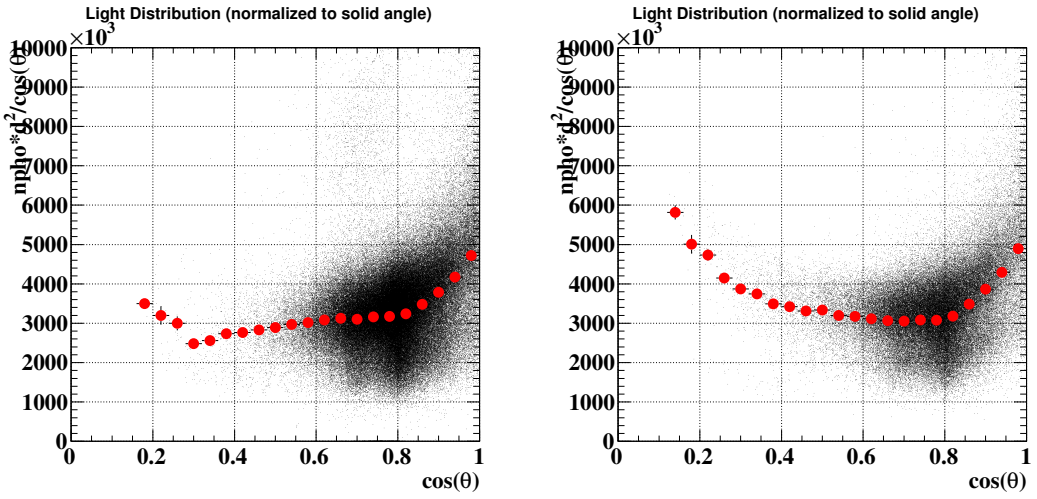

(a) (b)

Figure 7.26: Light collection on outer faces PMTs in data (a) and Monte Carlo (b), normalized to solid angle.

The analysis described in Section 7.2.5 was repeated after the change in optical properties. As the changes in models did not extensively modify the energy scale, the radial shift of α wires in the QE evaluation was confirmed, with the addition of a small correction to the aluminum reflectivity R_{Al} from 63% to 70%. The final result, displayed in Fig. 7.29, is the best agreement reached so far between Monte Carlo and data.

A quantitative comparison of light width peaks (Fig. 7.30) shows that the simulation and data are now in good agreement, within $\sim 10\%$.

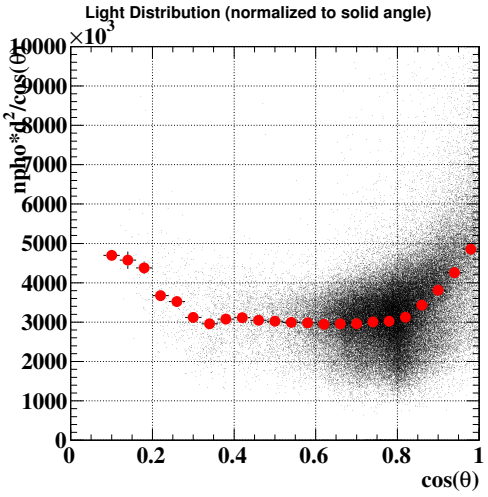

Figure 7.27: Light collection, normalized to solid angle, on outer faces PMTs from Monte Carlo using the new formulas for refractive indexes.

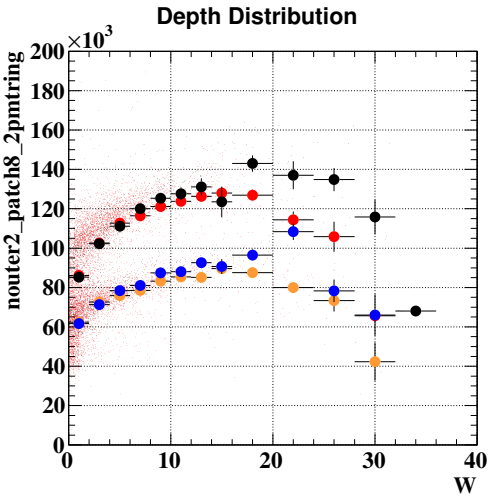

Figure 7.28: Scatter plot of π^0 data (*red*: 83 MeV; *orange*: 55 MeV) and Monte Carlo (*black*: 83 MeV; *blue*: 55 MeV) for the two-wide PMT ring surrounding the *patch8* outer face, using the new refraction index models.

7.3 Linear Fit Analysis

Given the excellent agreement between data and MC achieved in the previous section, we attempted the use of a linear fitting algorithm to reconstruct the energy of π^0 events, to verify the achievable energy resolution with this method which is, in principle, depth-independent.

The training process for the linear fit algorithm was performed on 2.5×10^4 events from a Monte Carlo set generated with the modified parameters described in the previous section. The coefficients were applied to data analyzed with gas-evaluated QEs extracted using a simulation with the same optical properties.

Ordinarily, the Monte Carlo simulation only tracks 16% of scintillation photons to the PMTs in order to save processing power. This provides an energy scale consistent with the one from real data, originating from QEs being normalized to an average value of 16%.

In order to minimize statistical fluctuations for this delicate process, the full 100% of scintillation photons were simulated with the same QEs used for data analysis. PMTs

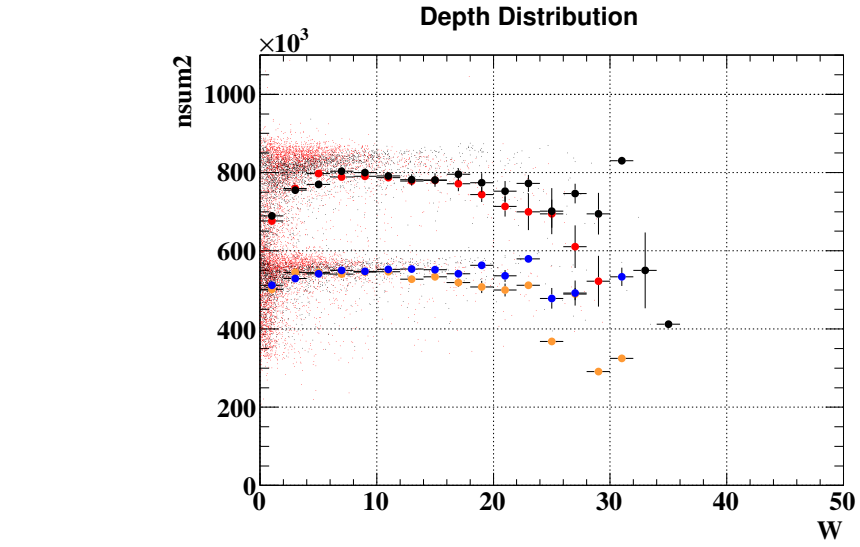

(a)

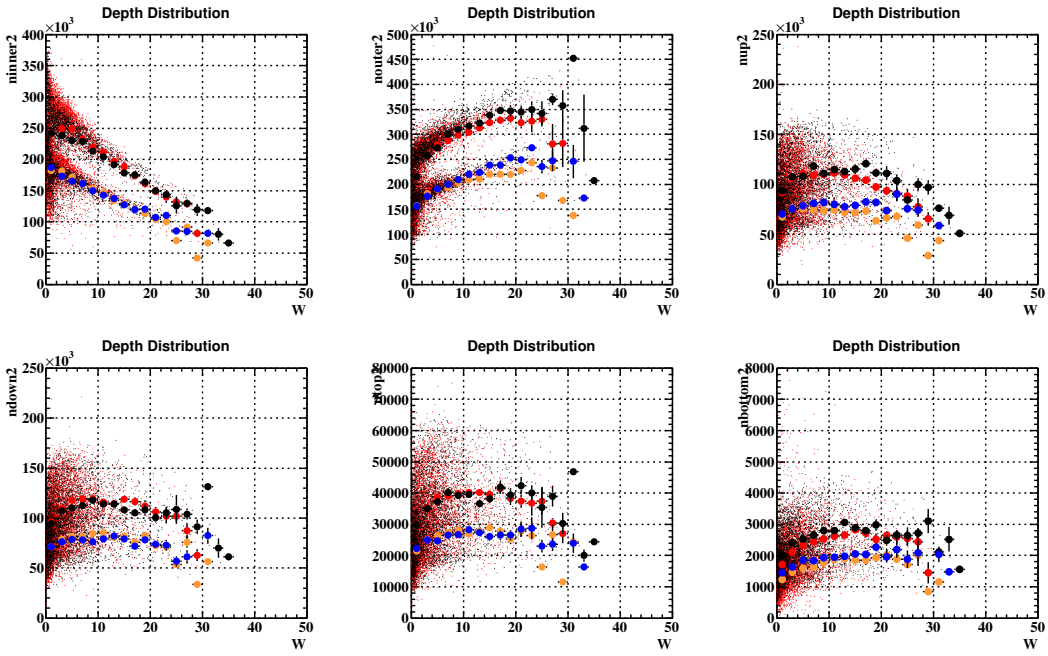

(b)

Figure 7.29: Profiled scatter plot of π^0 data with GXe QEs (*red*: 83 MeV; *orange*: 55 MeV) and Monte Carlo (*black*: 83 MeV; *blue*: 55 MeV) events for (a) the full calorimeter and (b) each individual face, as a function of event depth.

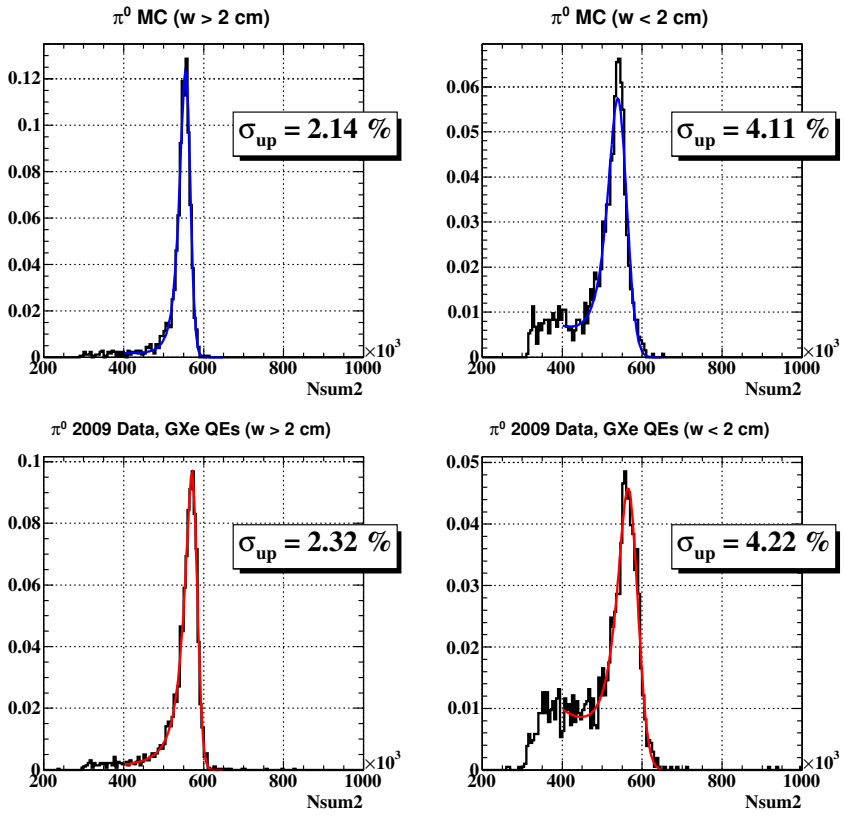

Figure 7.30: Simulated (*blue*) and measured (*red*) 55 MeV light peaks for deep and shallow events, showing the achieved agreement in calorimeter response.

with low (< 30 photons) or no signal were discarded from training on an event per event basis and not used for the energy reconstruction, in order to exclude the contribution of pedestal fluctuations for the real data.

The result of the reconstruction for 55 MeV photons are shown in Fig. 7.31. The cuts applied are the same as in Section 7.2.5 with a less stringent requirement of 60% total energy in the central NaI crystal, which is the cut that was used when measuring the official MEG I resolutions.

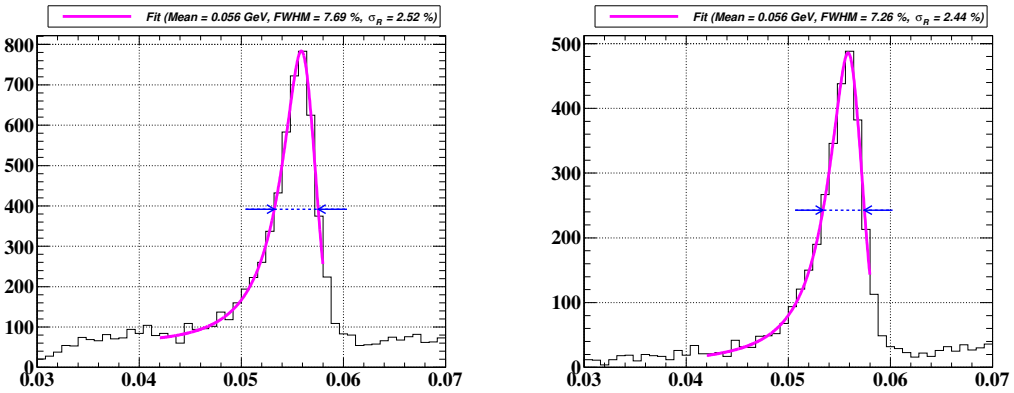

(a) (b)

Figure 7.31: Linear fit reconstruction of 55 MeV photon for all events (a) and events at depth $w > 2$ cm (b).

The reconstructed energy fitted with a tailed gaussian function gives us a resolution of $\sigma_R = 2.52\%$ at all depths, and $\sigma_R = 2.44\%$ for $w > 2$ cm. The obtained resolution has only a slight position dependence compared to the standard method (which gives 2.4% for $w < 2$ cm and 1.7% for $w > 2$ cm), but still a worse overall performance, even after the improvements in the simulation.

The reason for this lies in the core concept of principal component analysis. PCA assumes a linear relationship between acquired data and information contained within it, such that a linear transformation from one to the other is possible. If nonlinear elements were present, the closest linear approximation is taken, eliminating the nonlinear component.

The light collected by the inner face PMTs near the event, which normally would give the greatest contribution to energy evaluation, is also subject to the greatest fluctuation based on the shower position. The training algorithm solves this by heavily

suppressing their coefficients in the energy sum by a factor of ~ 100 and instead using faraway PMTs for reconstruction, where the effects of reflection contribute the most.

The current implementation of the linear fit thus does not seem to be suitable for energy reconstruction in MEG I. However the excellent agreement achieved between data and MC suggests that a better algorithm can be developed. Instead of training on a whole patch, a possible solution would be to individually train on a finer mesh, similar to the one used in Section 7.2.2, with each pixel corresponding to a different set of coefficients, thus sidestepping the issue. In MEG II the inner face pixellation is expected to solve the position dependence, making such a solution unnecessary.

Conclusions

The MEG experiment searching for the rare lepton flavor violating decay $\mu \to e\gamma$ at PSI has completed its first phase in 2013. The analysis of the data from the first half (2009-2011) of this run provides the best upper limit for the $\mu \to e\gamma$ branching ratio: $\mathcal{B} = 5.7 \times 10^{-13}$ at 90% CL. The final analysis on the full data set is underway and a final sensitivity of $4 \div 5 \times 10^{-13}$ is expected. An upgraded second phase (MEG II) is expected to increase the sensitivity by a factor of 10 in a short amount of time, competitive with future cLFV experiments.

A new stereo wire drift chamber is being designed by the Italian side of the collaboration to act as the new positron tracker. The results of the aging tests for the chamber were described, showing it to be suitable for 3 years of high rate operation. The expected performances in terms of single hit resolution were shown. The construction of the first full scale single cell prototype demonstrated the feasibility of a 2 m long stereo drift chamber with variable cell size. Signal timing and charge were measured through the use of a double readout. A longitudinal resolution of ~ 10 cm was shown to be achievable on the basis of this information alone. Gain variation along the cell length was studied and a method to measure the wire tension during the full chamber construction was discussed.

Discrepancies between simulated and measured resolutions were present in the MEG I photon detector and may persist in MEG II, potentially requiring a new reconstruction algorithm. A thorough investigation of the liquid xenon detector was undertaken to understand the limits of the experiment's sensitivity. The use of α sources in gas phase xenon was shown to provide a more accurate evaluation of PMT quantum efficiency as opposed to the MEG I liquid phase calibration scheme, and is proposed for MEG II with the *caveat* of requiring an increased amount of sources. New optical parameters for the calorimeter's components were extracted, showing better agreement

with published data and simultaneously providing a new, more faithful simulation of the calorimeter's response. An alternate algorithm based on a linear fitting technique was applied in an attempt provide an energy reconstruction more closely matching the MC predictions. However its performance in the current implementation is limited by nonlinearities in the MEG I calorimeter's response.

Based on the R&D studies performed we can conclude that the MEG II drift chamber does not display noticeable issues. Its construction is underway and the current outlook is promising. The photon detector will on the other hand require a detailed study after construction, using experimental data to characterize its response and quantify potential systematics. The schedule for MEG II is advancing on time and the experiment is set to probe the limits of cLFV to unprecedented sensitivity, searching for new physics years ahead of the competition.

Bibliography

[1] Y. Kuno and Y. Okada, *Muon decay and physics beyond the standard model*, *Rev.Mod.Phys.* **73** (2001) 151–202, [hep-ph/9909265].

[2] **Particle Data Group**, K. Olive et al., *Review of Particle Physics*, *Chin.Phys.* **C38** (2014) 090001.

[3] **CHOOZ Collaboration**, M. Apollonio et al., *Search for neutrino oscillations on a long baseline at the CHOOZ nuclear power station*, *Eur.Phys.J.* **C27** (2003) 331–374, [hep-ex/0301017].

[4] **KamLAND Collaboration**, K. Eguchi et al., *First results from KamLAND: Evidence for reactor anti-neutrino disappearance*, *Phys.Rev.Lett.* **90** (2003) 021802, [hep-ex/0212021].

[5] **K2K Collaboration**, E. Aliu et al., *Evidence for muon neutrino oscillation in an accelerator-based experiment*, *Phys.Rev.Lett.* **94** (2005) 081802, [hep-ex/0411038].

[6] **Super-Kamiokande Collaboration**, Y. Suzuki, *Solar neutrino results from Super-Kamiokande*, *Nucl.Phys.Proc.Suppl.* **77** (1999) 35–42.

[7] **SNO Collaboration**, Q. Ahmad et al., *Measurement of the rate of* $\nu_e + d \to p + p + e^-$ *interactions produced by* ^8B *solar neutrinos at the Sudbury Neutrino Observatory*, *Phys.Rev.Lett.* **87** (2001) 071301, [nucl-ex/0106015].

[8] **MACRO Collaboration**, G. Giacomelli and A. Margiotta, *Macro results on atmospheric neutrinos*, *Nucl.Phys.Proc.Suppl.* **145** (2005) 116–119, [hep-ex/0504029].

[9] H. Georgi and S. Glashow, *Unity of All Elementary Particle Forces*, *Phys.Rev.Lett.* **32** (1974) 438–441.

[10] H. Fritzsch and P. Minkowski, *Unified Interactions of Leptons and Hadrons*, *Annals Phys.* **93** (1975) 193–266.

[11] H. Georgi and D. V. Nanopoulos, *Ordinary Predictions from Grand Principles: T Quark Mass in O(10)*, *Nucl.Phys.* **B155** (1979) 52.

[12] J. Aysto et al., *Physics with low-energy muons at a neutrino factory complex*, CERN-TH-2001-231 Technical Report, [hep-ph/0109217].

[13] L. Calibbi et al., *Flavour violation in supersymmetric SO(10) unification with a type II seesaw mechanism*, *JHEP* **0912** (2009) 057, [arXiv:0910.0377].

[14] **MEGA Collaboration**, M. Ahmed et al., *Search for the lepton-family-number nonconserving decay $\mu^+ \to e^+\gamma$*, *Phys.Rev.* **D65** (2002) 112002, [hep-ex/0111030].

[15] **RENO collaboration**, J. Ahn et al., *Observation of Reactor Electron Antineutrino Disappearance in the RENO Experiment*, *Phys.Rev.Lett.* **108** (2012) 191802, [arXiv:1204.0626].

[16] **DAYA-BAY Collaboration**, F. An et al., *Observation of electron-antineutrino disappearance at Daya Bay*, *Phys.Rev.Lett.* **108** (2012) 171803, [arXiv:1203.1669].

[17] **T2K Collaboration**, K. Abe et al., *Indication of Electron Neutrino Appearance from an Accelerator-produced Off-axis Muon Neutrino Beam*, *Phys.Rev.Lett.* **107** (2011) 041801, [arXiv:1106.2822].

[18] **DOUBLE-CHOOZ Collaboration**, Y. Abe et al., *Indication for the disappearance of reactor electron antineutrinos in the Double Chooz experiment*, *Phys.Rev.Lett.* **108** (2012) 131801, [arXiv:1112.6353].

[19] S. Antusch et al., *Impact of θ_{13} on lepton flavour violating processes within SUSY seesaw*, *JHEP* **11** (2006) 090, [hep-ph/0607263].

[20] G. Blankenburg et al., *Neutrino Masses and LFV from Minimal Breaking of $U(3)^5$ and $U(2)^5$ flavor Symmetries*, *Eur.Phys.J.* **C72** (2012) 2126, [arXiv:1204.0688].

[21] **Mu2e Collaboration**, R. Carey et al., *Proposal to search for $\mu^- N \to e^- N$ with a single event sensitivity below 10^{-16}*, FERMILAB-PROPOSAL-0973 (2008).

[22] Paul Scherrer Institut, PSI Accelerator Facilities Users Guide. Information available also from the PSI web site www.psi.ch/

[23] J. Allison et al., *The Diamond shaped cathode pads of the OPAL muon barrel drift chambers*, *Nucl.Instrum.Meth.* **A310** (1991) 527–534.

[24] *Hamamatsu Photonics, R9869*. Details available at www.hamamatsu.com/

[25] A. Baldini et al., *Absorption of scintillation light in a 100 l liquid xenon gamma ray detector and expected detector performance*, *Nucl.Instrum.Meth.* **A545** (2005) 753–764, [physics/0407033].

[26] G. J. Feldman and R. D. Cousins, *A Unified approach to the classical statistical analysis of small signals*, *Phys.Rev.* **D57** (1998) 3873–3889, [physics/9711021].

[27] **MEG collaboration**, J. Adam et al., *New limit on the lepton-flavour violating decay $\mu^+ \to e^+\gamma$*, *Phys.Rev.Lett.* **107** (2011) 171801, [arXiv:1107.5547].

[28] **MEG Collaboration**, J. Adam et al., *New constraint on the existence of the $\mu^+ \to e^+\gamma$ decay*, *Phys.Rev.Lett.* **110** (2013) 201801, [arXiv:1303.0754].

[29] **COMET Collaboration**, Y. Cui et al., *Conceptual design report for experimental search for lepton flavor violating $\mu \to e$ conversion at sensitivity of 10^{-16} with a slow-extracted bunched proton beam (COMET)*, KEK-2009-10 Technical Report.

[30] A. Blondel et al., *Research Proposal for an Experiment to Search for the Decay $\mu \to eee$*, [arXiv:1301.6113].

[31] T. Aushev et al., *Physics at Super B Factory*, [arXiv:1002.5012].

[32] A. Baldini et al., *MEG Upgrade Proposal*, [arXiv:1301.7225].

[33] A. Papa et al., *Development of an active target for $\mu \to e\gamma$ search*, *Nucl.Instrum.Meth.* **A718** (2013) 580–581.

[34] M. Adinolfi et al., *The tracking detector of the KLOE experiment*, *Nucl.Instrum.Meth.* **A488** (2002) 51–73.

[35] V. Re et al., *Status and prospects of the BaBar SVT*, *Nucl.Instrum.Meth.* **A560** (2006) 5–8.

[36] S. Ritt, *DRS4 evaluation board manual. PSI edition.* Last revised on March 6, 2014. Information available at `http://www.psi.ch/drs/documentation/`

[37] M. G. Hosack and T. Coan, *Simple acoustical technique for automated measurement of drift tube anode wire tension*, *Nucl.Instrum.Meth.* **A556** (2006) 115–118.

[38] H. Wind, *Principal component analysis*, CERN EP Internal Report **81-12**/Rev.1 August 1982.

[39] J. Shlens, *A tutorial on principal component analysis*, *CoRR* (2014), [`arXiv:1404.1100`].

[40] A. Porcelli, *Studio delle sistematiche del calorimetro elettromagnetico dell'esperimento MEG per l'ottimizzazione della ricerca del decadimento $\mu \to e\gamma$* (Master's Thesis).

[41] Sellmeier equation fitted to measurements in 2005 by S. Nakamura et al., Yokohama/KEK. The Sellmeier coefficients are taken from private communication with S. Nakamura, Yokohama National University, and T. Haruyama, KEK (unpublished).

[42] A. Hitachi et al., *New approach to the calculation of the refractive index of liquid and solid xenon*, *J. Chem. Phys.* **123** (2005) 234508.

[43] G. Ghosh, *Dispersion-equation coefficients for the refractive index and birefringence of calcite and quartz crystals*, *Opt. Commun.* **163** (1999) 95–102.

[44] I. H. Malitson, *Interspecimen comparison of the refractive index of fused silica*, *J. Opt. Soc. Am.* **55** (1965), 1205–1208.

[45] T. Radhakrishnan, *The dispersion, briefringence and optical activity of quartz*, *Proceedings of the Indian Academy of Sciences - Section A* **25**–3 (1947), 260–265.

Acknowledgements

I want to thank all the people who, with their help and support, made this work possible.

First of all my thanks go to the extraordinary researchers of the Pisa MEG group, who watched me grew from an inexperienced undergrad into the person I am now: my supervisor Alessandro Baldini, who tutored me relentlessly on countless topics and never gave up on me, even when the hardships of research nearly made me gave up on myself; Fabrizio Cei, who was always available for discussion and questioning, always having some new insight to provide; Giovanni Signorelli, who through his brilliant mind and sharp wit showed me the beauty of physics; Marco Grassi, Carlo Bemporad and Donato Nicolò, whose experience I could count on whenever I tackled a topic I was unfamiliar with; Simeone Dussoni, who gave me frank opinions, practical advice and, one infamous evening, first-aid treatment; and Luca Galli and Marco Venturini, who being the closest to me in age I could confide my troubles to without worry. My thanks are also extended to the rest of the MEG collaboration members, who are too many to name individually; here I'll just mention Angela, who I share a special friendship with and was still there to support me even after leaving Pisa for Switzerland; Elisabetta who spent many lab hours with me on the Long Prototype, trying to make the damn thing work; and Emanuele who shared with me the experience of being a PhD student in MEG, including braving the snowy dawn by car after an especially freezing shift.

All of this would not have been possible without support and love of my parents, my sisters, and all of my family. A special mention goes to my grandparents, who never stopped being by my side even when far away—and some, sadly, farther still.

I also thank all of my close friends, who patiently accepted the times my work kept me busy or distant; it made our reunions all that much sweeter.

A peculiar thank you goes to my cat who, by complaining whenever I stayed awake past

2 AM, managed to succeed where many humans failed and kept my sleeping schedule to a somewhat reasonable standard.
Finally, my greatest and deepest gratitude goes to my wife Benedetta, who tirelessly and selflessly supported me over the course of this work. There is very little that words can express except that you are my light, my love and my life, and I thank you from the bottom of my heart.